

# Surface Physics/Chemistry

Ib Chorkendorff  
Interdisciplinary Research Center for Catalysis (ICAT)  
and  
Center for Atomic-scale Materials Physics (CAMP)  
at  
Department of Physics, Building 307  
Technical University of Denmark DK-2800 Lyngby  
Denmark



# Contents

Contents . . . . .	ii
<b>1 Introduction</b>	<b>1</b>
1.1 Area of Application . . . . .	2
<b>2 Requirements for Surface Analysis</b>	<b>3</b>
2.1 Ultra High Vacuum . . . . .	3
2.1.1 Example . . . . .	4
2.1.2 Vacuum Equipment . . . . .	5
2.1.3 Vacuum Pumps . . . . .	5
2.1.4 Pressure Measurement . . . . .	6
2.2 Surface Sensitivity . . . . .	9
2.2.1 The Inelastic Mean Free Path . . . . .	9
2.2.2 The Energy Loss Mechanisms in Solids . . . . .	11
2.3 Problems . . . . .	17
<b>3 Energy Analysis</b>	<b>19</b>
3.1 The Concentric Mirror Analyser . . . . .	19
3.2 The Hemi-Spherical Analyser . . . . .	20
3.2.1 Example . . . . .	22
<b>4 The XPS Method</b>	<b>25</b>
4.1 X-ray Sources . . . . .	26
4.2 Spectral Interpretation . . . . .	31
4.2.1 Multiplet splitting in XPS . . . . .	33
4.2.2 The Binding Energy in XPS . . . . .	39
4.2.3 Line Width . . . . .	45
4.2.4 The Transition Probability . . . . .	48
4.3 Quantitative XPS Analysis . . . . .	51

4.3.1	Example . . . . .	52
4.4	Problems . . . . .	56
<b>5</b>	<b>Ultraviolet or Synchrotron Photoelectron Spectroscopy</b>	<b>61</b>
5.1	The Experimental Setup . . . . .	61
5.2	The Electronic Structure . . . . .	62
5.2.1	The Band Structure . . . . .	62
5.2.2	The Electronic Structure of Adsorbates . . . . .	65
<b>6</b>	<b>The Auger Process</b>	<b>71</b>
6.1	The Excitation Source . . . . .	73
6.2	The Fine Structure in AES . . . . .	74
6.2.1	Nomenclature . . . . .	74
6.2.2	Multiplet Splitting in AES . . . . .	76
6.3	AES for Qualitative Analysis . . . . .	80
6.4	AES for Quantitative Analysis . . . . .	88
6.4.1	Example . . . . .	91
6.4.2	Growth Mechanisms . . . . .	93
6.5	Scanning Auger Microscopy SAM . . . . .	94
6.6	Problems . . . . .	100
<b>7</b>	<b>Depth Profiling with XPS and AES</b>	<b>103</b>
7.1	Instrumentation . . . . .	103
7.2	Ion Sputtering . . . . .	105
7.2.1	The Sputter Yield . . . . .	108
7.3	Factors Limiting Depth Resolution and Accuracy of Profiles . . . . .	109
7.3.1	The Effect of Attenuation . . . . .	110
7.3.2	Other Effects . . . . .	112
7.4	Practical Sputter Profiling . . . . .	116
7.4.1	Sputter Profile of Stainless Steel . . . . .	116
7.4.2	Investigations of Electrical Contacts . . . . .	119
7.4.3	Control of Thin Coatings . . . . .	119
7.5	Problems . . . . .	126
<b>8</b>	<b>Vibrational Spectroscopies HREELS and IR</b>	<b>127</b>
8.1	High Resolution Electron Energy Loss Spectroscopy . . . . .	127
8.1.1	Experimental Set-up . . . . .	127
8.1.2	The Energy Loss Spectrum . . . . .	129

8.1.3	Experimental Results . . . . .	133
8.2	Infrared Adsorption Spectroscopy . . . . .	139
<b>9</b>	<b>Low Energy Electron Diffraction LEED</b>	<b>141</b>
9.1	Surface Crystallography . . . . .	141
9.1.1	Crystal Planes . . . . .	142
9.1.2	Adsorbate Sites . . . . .	145
9.1.3	The Two-Dimensional Lattice . . . . .	145
9.2	Low Electron Energy Diffraction . . . . .	146
9.2.1	Experimental Set-up . . . . .	146
9.2.2	Kinematic Theory . . . . .	149
9.2.3	Multiple Scattering . . . . .	158
9.2.4	Notation and Examples . . . . .	159
9.2.5	Domains . . . . .	163
9.3	Dynamical Scattering and IV-Curves . . . . .	165
<b>10</b>	<b>Microscopy</b>	<b>169</b>
10.1	The Scanning Probe Methods . . . . .	170
10.1.1	Theory of STM . . . . .	172
10.1.2	Results from the Yellium Model . . . . .	177
10.2	Spectroscopy . . . . .	180
10.3	Examples of STM Investigations . . . . .	184
10.3.1	Surface Structure . . . . .	184
10.3.2	Two-Dimensional Alloys and Overlayers . . . . .	188
10.3.3	Dynamics and Chemical Reactions . . . . .	192
10.4	Electron Microscopy . . . . .	193
<b>11</b>	<b>Ion Scattering Methods</b>	<b>197</b>
11.1	Low Energy Ion Scattering Spectroscopy . . . . .	197
11.2	High Energy Ion Scattering Spectroscopy . . . . .	201
11.3	Secondary Ion Mass Spectroscopy . . . . .	203
	<b>Bibliography</b>	<b>207</b>

# Chapter 1

## Introduction

Material science applies a broad spectrum of analytical methods for characterisation. For materials where the surface is particularly important, the methods used are the surface sensitive methods. This in itself is a very broad area and includes a large number of complementary methods for investigations of surface composition, structure, reactivity, etc. Here we shall restrict ourselves to the most generally applied methods, such as: The X-ray induced Photoemission Spectroscopy (XPS) also called Electron Spectroscopy for Chemical Analysis (ESCA) and Auger Electron Spectroscopy (AES). These methods can give information on the surface composition and chemistry, and combined with other methods also give information on the lateral and depth composition. Actually any laboratory that is seriously investigating surfaces on the atomic level will have either of these two spectroscopies available. Besides these two rather fundamental methods there are a great number of more special methods which are used in various combinations in order to investigate more complex systems such as the physics of adsorbates and reactions on surfaces. Here we shall go through the most often encountered methods (without making a complete list) which will include Ultraviolet Photoelectron Spectroscopy (UPS), Low Energy Electron Diffraction (LEED), High Resolution Electron Energy Loss Spectroscopy (HREELS), Scanning Tunneling Microscopy etc.

## 1.1 Area of Application

Surface scientific methods are used widely both in fundamental and in industrial research laboratories since many technologies require a good understanding of the behaviour of the surfaces. A number of fields can be mentioned such as

- Catalysis
- Adhesion
- Corrosion
- Tribology

Common to all these phenomena is the importance of surface reactivity. Especially in the area of catalysis, surface science has a strong impact for the understanding of what is going on at the atomic level. Surface science is also widely used in other areas like:

- Metallurgy
- Biophysics
- General material synthesis
- Microelectronics

The latter field is probably where most of the analytical methods like Scanning Auger Microscopy (SAM), Auger Electron Spectroscopy (AES), and X-ray Photo-electron Spectroscopy is being brought into use. In general the field of surface science is very cross-disciplinary and is expected to develop continuously with the demand for better materials.

It is the intention here to give a brief introduction to most prominent methods and their applications in material science. For detailed and complete discussion of the various subjects touched upon here we shall refer the reader to references [1, 2, 3, 4, 5, 6, 7, 8].

# Chapter 2

## Requirements for Surface Analysis

In this chapter we shall deal with the two major demands for being able to perform surface analysis. The first requirement may seem at a glance rather trivial but it makes surface science troublesome and expensive. In order to be able to study a surface on the atomic level it is imperative that the cleanliness of the surface can be controlled to a very high degree. Thus all experiments must be performed under **Ultra High Vacuum**.

### 2.1 Ultra High Vacuum

Since it is not possible to establish absolute vacuum and as the expenses increases rapidly with the quality of the vacuum it is very important to consider what is really required.

From the kinetic gas theory the velocity distribution is given by a Maxwell-Boltzmann distribution. If we only consider the distribution for molecules with velocity components orthogonal to the surface it can be written as:

$$f(v_x)dv_x = \sqrt{\frac{m}{2\pi kT}} e^{-\frac{mv_x^2}{2kT}} dv_x \quad (2.1)$$

where  $k$  is Boltzmann's constant,  $m$  is the mass of the gas molecule, and  $T$  is the temperature of the gas. The flux  $dF(v_x)$  of particles per  $v_x$  is proportional to the velocity and the probability distribution.



$$dF(v_x) = v_x f(v_x) dv_x = v_x \sqrt{\frac{m}{2\pi kT}} e^{-\frac{mv_x^2}{2kT}} dv_x \quad (2.2)$$

Thus the total flux at the surface is easily found by integration over all velocities

$$F = \int_0^\infty f(v_x) v_x dv_x \quad (2.3)$$

$$F = \int_0^\infty \sqrt{\frac{m}{2\pi kT}} e^{-\frac{mv_x^2}{2kT}} v_x dv_x \quad (2.4)$$

$$F = \sqrt{\frac{kT}{2\pi m}} \quad (2.5)$$

If we want to determine the flux of particles hitting per surface area per time unit this flux has to be weighted by the gas density  $\rho$ . Assuming an ideal gas  $\rho$  can be rewritten as  $\frac{P}{kT}$  leading to the final equation

$$F_{tot}(P, T) = \frac{P}{\sqrt{2\pi mkT}} \quad (2.6)$$

Which implication does this have?

### 2.1.1 Example

Assume that we have been able to obtain a base pressure of  $1 \times 10^{-6}$  mbar oxygen in our vacuum chamber. How long time will it take before every atom on our surface has been hit once on average? We are studying a Cu(100) surface which contains  $1.5 \times 10^{15}$  copper atoms per  $\text{cm}^2$ . By substitution of the relevant numbers into equation (2.6) it is found that the flux at this pressure is  $2.7 \times 10^{14}$   $\text{O}_2$  molecules per  $\text{cm}^2$  per second. Thus if all the molecules that hit the surface reacts, it will be covered with oxygen within 5 s. As many surface science experiments take hours, it is necessary to reduce the pressure by 4 orders of magnitude leading to Ultra High Vacuum with a base pressure less than  $1 \times 10^{-10}$  mbar. How can such low pressure be obtained routinely?

### 2.1.2 Vacuum Equipment

All experiments must be performed in a container where the vacuum can be established. There are rather strong demands on the materials used. They should have a sufficient low vapour pressure even at temperatures as high as 150°C. This immediately rules out such materials as brass, tin, lead, silver solders containing cadmium, plastic etc. The commonly used materials are stainless steel, glass and ceramics. Usually the vacuum is established by pumping the chamber with a sufficiently good pump and then heat it to at least 150°C for at least 12 hours. This will increase the outgassing from the inner walls considerably so that an adequate base pressure can be obtained when it has cooled down to room temperature.

### 2.1.3 Vacuum Pumps

The pumps used for this sort of experiments can naturally be divided into two groups: The open types where the gas is removed from the apparatus and the closed types where the gas is captured by implantation, reaction or simply by freezing out in the pump itself.

Usually the apparatus is pumped down from atmospheric pressure by use of open pumping systems as we are dealing with considerable amounts of gas in this situation. A typical combination will consist of a serially connected rough pump ( $P_{base} \leq 1 \times 10^{-3}$ ) and a turbopump (see Figure 2.1) or an oil diffusion pump (see Figure 2.3). Both types of pumps have base pressures around the desired  $1 \times 10^{-10}$  mbar.

In the pressure regime below  $1 \times 10^{-6}$  mbar the pumping is enforced or done solely by the closed types, like the ion pump (see Figure 2.4) which removes the gas molecules by a combination of implantation into titanium plates and reaction with freshly exposed titanium.

Another type of a closed pump is the cryo-pump which simply freezes out the gasses by having a very cold region with a large surface area. Both these pumps are very clean and useful. Which pump is used is very much dictated by what sort of experiments that has to be performed as each has its advantages or drawbacks such as:

- Ion-pumps ..... generates strong magnetic fields
- Turbo-pumps ..... generates vibrations

- Cryo-pumps ..... generates vibrations
- Oil diffusion-pumps ..... requires a constant use of liq. nitrogen.

The vacuum chamber must be pumped continuously in order to compensate for outgassing of the walls and any analytical methods installed in the apparatus. If there is a malfunction on the apparatus so it must be vented, the whole procedure of pumping down and baking out must be repeated and a loss of at least one or generally two working days must be faced to re-establish the vacuum.

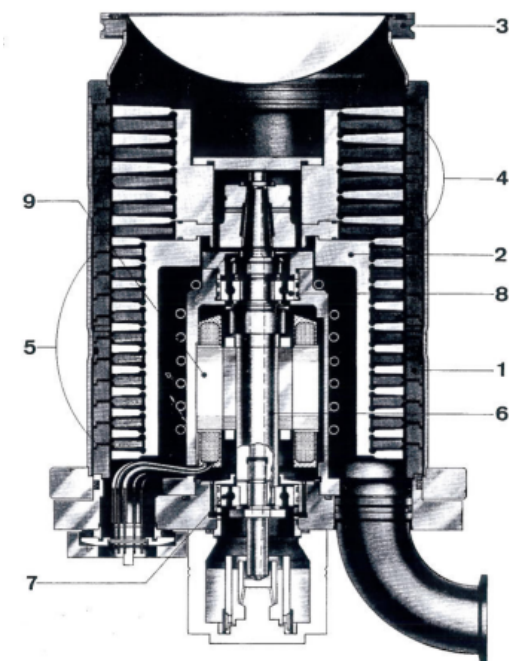


Figure 2.1: Schematic of a turbo pump.

#### 2.1.4 Pressure Measurement

The very low pressure makes the task of measuring the pressures a bit more difficult as all gauges relying on mechanical principles can be ruled out. Usually the pressure is monitored by use of a Bayard-Alpert Ionisation Gauge as shown in Figure 2.5.

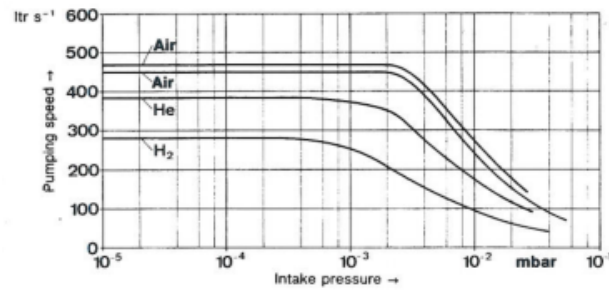


Figure 2.2: Pumping speed as a function of pressure.

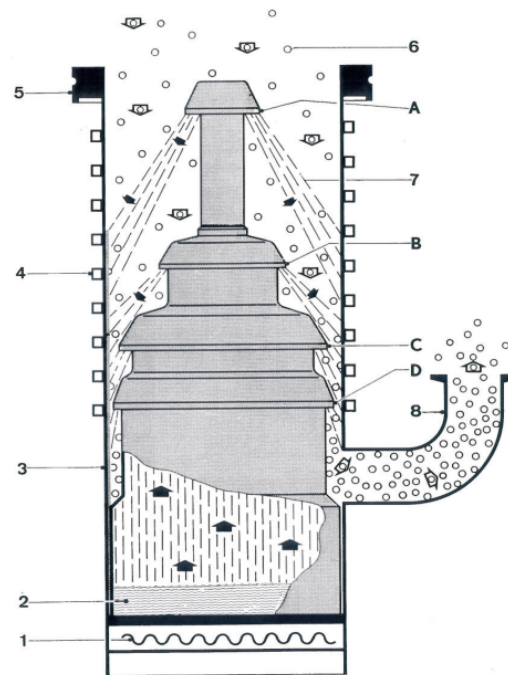


Figure 2.3: Schematics of an oil-diffusion pump.

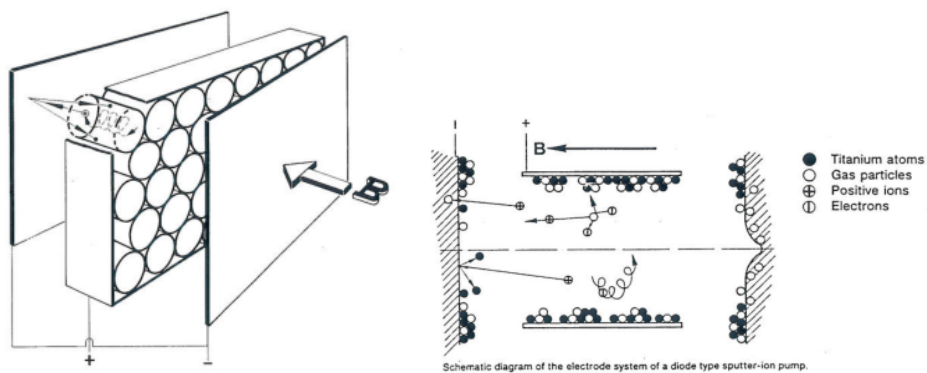


Figure 2.4: Schematics of ion-pumps.

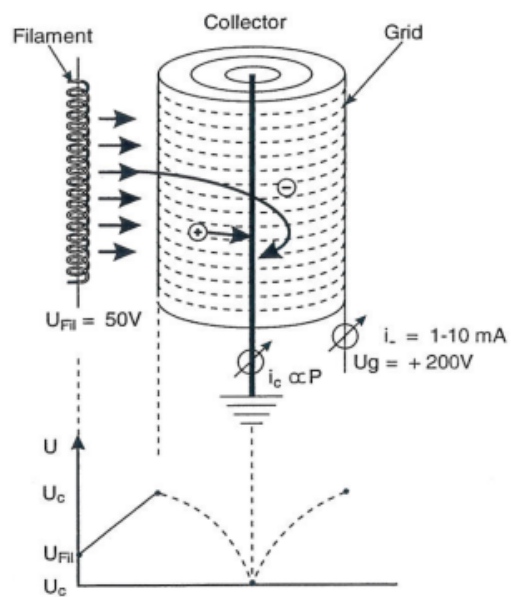


Figure 2.5: Schematics of an ionisation-gauge.

The principle is that electrons are accelerated from a hot filament towards an open structured cage made of a grid. Some electrons will penetrate the cage and be able to ionise gas molecules. In the middle of the cage a thin wire called the collector is mounted which is negatively biased compared to the cage. Positive ions produced by the electron bombardment will be collected by the wire and the current measured will be proportional to the gas density in the cage and thus in the apparatus. Usually such gauges work in the range  $1 \times 10^{-4}$  mbar to  $4 \times 10^{-11}$  mbar. Unfortunately the pressure reading will depend on the gas composition and must therefore be calibrated for the relevant gas.

For more details on Ultra High Vacuum and design of such equipment we shall simply refer to [9].

## 2.2 Surface Sensitivity

The second requirement for doing surface analysis is naturally to have methods that are sensitive to the surface. This in general rules out otherwise useful methods like electron microscopy, X-ray diffraction and Mössbauer spectroscopy. The methods inherently applicable for surface investigations are the electron spectroscopies. These methods are relying on the fact that electrons which are passing through a medium will undergo energy losses and thereby have a limited penetration depth. The electron spectroscopies are all performed by excitation of the solid which then will emit electrons with a characteristic energy distribution  $N(E)$  that allows for identification of the composition of the solid. The excitation source for generation of these electron energy distributions does not need to be surface sensitive and therefore high energy electrons (AES), X-rays (XPS) or even ions can be used. The important point is that the electrons emitted undergo energy losses on their way out of the solid and therefore electrons coming from inside the solid will be exponentially damped. We shall in later chapters treat the detection, measurements, and interpretation of the emitted electrons and now concentrate on the mechanisms ensuring the surface sensitivity.

### 2.2.1 The Inelastic Mean Free Path

A useful term for describing the energy loss process is the inelastic mean free path  $\lambda(E)$ . Which, in this case, is the length an electron will travel in a solid

without experiencing any losses. This length is usually on the order of 5 Å to 100 Å.

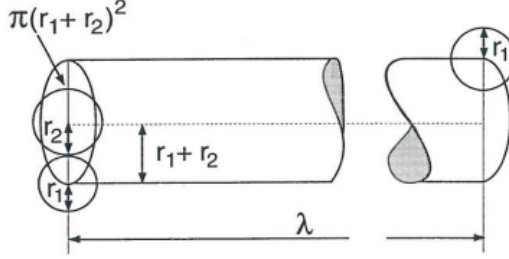


Figure 2.6:

If we consider a hard sphere model, see Figure 2.6, the mean free path can easily be derived in terms of the cross-section

$$\sigma = \pi(r_1 + r_2)^2 \quad (2.7)$$

and the density  $\rho$ . The volume  $\lambda \times \sigma$  equals the volume of one molecule which is  $\rho^{-1}$  leading to

$$\lambda = (\sigma\rho)^{-1} \quad (2.8)$$

For a frozen ideal gas this would give

$$\lambda = \frac{kT}{\sigma P} \quad (2.9)$$

Taking into account the relative motion of the molecules the result is

$$\lambda = \frac{kT}{\sqrt{2}\sigma P} \quad (2.10)$$

Similar considerations can be made for electrons moving in a solid matter except that the cross-section is much more complex and dependent on the underlying mechanisms. Below we will describe the different mechanisms and their importance.

The important result of these mechanisms is summarised in Figure 2.7 where the inelastic mean free path for electrons is plotted against the electron energy in a number of different materials. This particular plot is known as *the universal curve*.

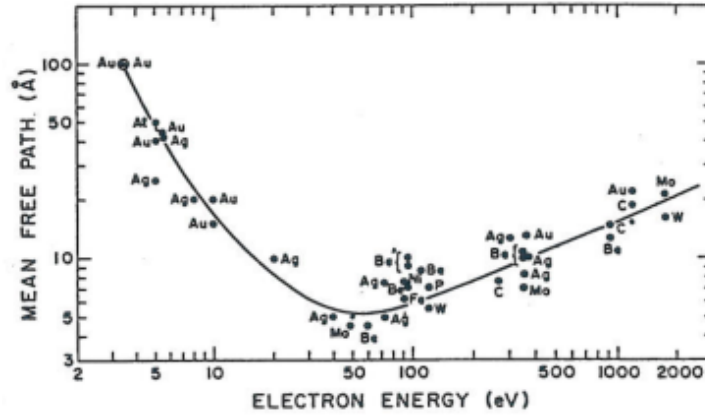


Figure 2.7: The universal curve showing the inelastic mean free path versus kinetic energy for a number of elements.

Notice that the mean free path is only a few atomic layers if we design our experiments so that the electrons have energies in the interval 50 eV to 1000 eV. This means that we are effectively able to set up very surface sensitive experiments when doing for instance XPS, as will be described in chapter 4.

### 2.2.2 The Energy Loss Mechanisms in Solids

There are a number of different energy loss mechanisms that are responsible for the behaviour of the inelastic mean free path observed in Figure 2.7.

We shall here consider the various mechanisms in the order of decreasing importance. Excitations of collective charge density waves also called plasmons is one of the most important mechanisms for energy loss of electrons in a solid medium with valence electrons. Consider a free electron metal like aluminium. The three valence electrons are highly delocalised and the system can be described relatively well by a jellium model where the electrons are smeared out on a background of positive charge. If we introduce a small perturbation of the charge densities of the electrons with respect to the positive background as shown in Figure 2.8 we can estimate the forces introduced on the volume element  $dV$ .

The volume element will have a charge of electrons which is



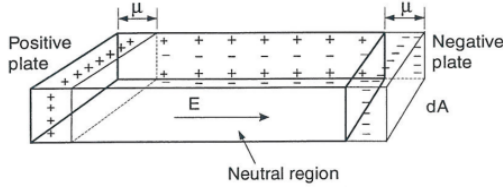


Figure 2.8: A sketch of the simple system used to derive the energy losses due to plasmons.

$$dq = n\mu edA \quad (2.11)$$

where  $n$  is the electron density,  $\mu$  is the displacement,  $e$  is the electronic charge, and  $dA$  is the area element. We can consider the two end plates of the box as a capacitor whereby we have the electric field  $E$

$$E = \frac{dq}{dA\epsilon_0} = \frac{ne\mu}{\epsilon_0} \quad (2.12)$$

By having the electric field we can apply Newton's 2nd law

$$m \frac{d^2\mu}{dt^2} = F_{electron} = -eE = -\frac{ne^2\mu}{\epsilon_0} \quad (2.13)$$

This is a simple 2nd order differential equation describing a harmonic oscillator with the frequency  $\omega_p$

$$\omega_p = \sqrt{\frac{ne^2}{\epsilon_0 m}} \quad (2.14)$$

For typical free electron metals like Mg and Al the models predict plasmon energy losses of 10.9 eV and 15.8 eV respectively which is in good agreement with the observed values of 10.6 eV and 15.3 eV.

This simple model does not work as well for metals where the valence electrons are more localised as is the case for the d-electrons in the transition metals.

By simple considerations of the electric field and its boundary conditions at the surface, it can be shown that a special type of plasmons can be excited in this region namely the surface plasmons. These plasmons will have a frequency which is  $\omega_s = \frac{\omega_p}{\sqrt{2}}$ .

The effect of the plasmon energy losses is easily observed by bombardment of a clean aluminium surface with electrons with increasing energy  $E_p$ . By analysing the electrons reflected from this surface, as illustrated in Figure 2.9, the  $N(E)$  distribution shown in Figure 2.10 is observed.

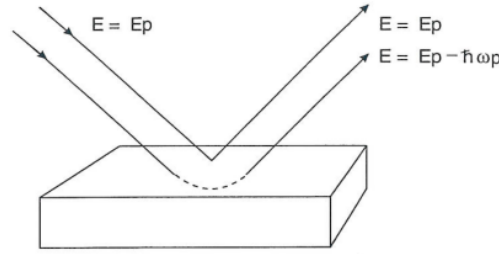


Figure 2.9:

The feature at the primary energy  $E_p$  is due to electrons which are elastically reflected. The features observed towards lower energies are the electrons which have undergone one or more energy losses. The bulk and the surface plasmons are easily seen and notice how the number of energy losses increases with increasing primary energy. Thus electrons emitted from within the aluminium will show similar energy loss spectra, although the surface contribution will only be half compared to the spectra shown in Figure 2.10 as they only have to pass the surface once.

The next mechanism for energy loss is ionisation of the atoms in the solid. In the scattering process the electron loses enough energy so that a bound electron can be lifted above the Fermi level of the solid and here occupy an empty state. The process is illustrated in Figure 2.11 where high energy electrons are transmitted through a 500 Å thin film of NiAl.

Again we clearly identify the plasmon losses, but if we look carefully towards higher energy losses the energy loss by excitation of the 2p electrons of aluminium and the 3p electrons of nickel can be observed. The energy losses observed fit very well with the excitation of the p electrons to just above the Fermi level as indicated in Figure 2.11. Larger energy losses are also possible, but will not lead to such distinct structure in the energy loss spectrum. The cross section for this type of excitation can be approximated by

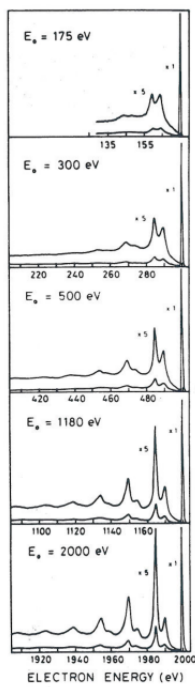


Figure 2.10: The energy loss spectra of aluminium for various primary energies.

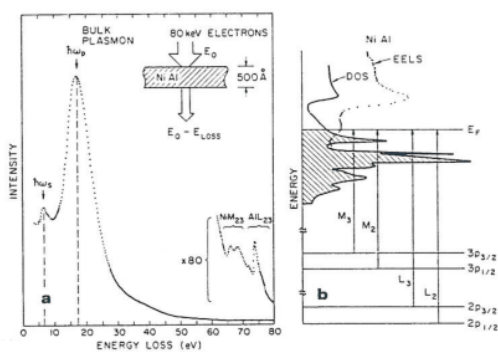


Figure 2.11: Discrete energy losses observed by transmission of 80 keV electrons through a NiAl alloy.

$$\sigma(E) \approx N_x \frac{\ln(\frac{E}{I_x})}{E} \quad (2.15)$$

where  $E$  is the energy of the electron,  $N_x$  is the number of electrons in subshell  $x$ , and  $I_x$  is the energy required for ionisation of this level. It is easily shown that this cross section has a maximum for electrons with an energy roughly three times the ionisation energy. The cross section plotted against  $\frac{E}{I_x}$  is shown in Figure 2.12. The same type of cross section behaviour also applies to excitations of plasmons.

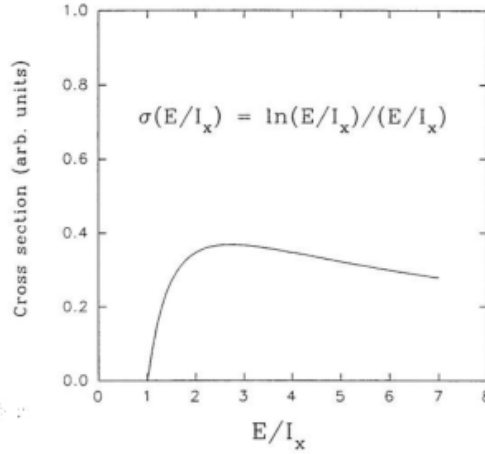


Figure 2.12: The cross-section for discrete energy loss as a function of energy.

Although the primary energy used in Figure 2.11 is atypical for the surface science experiments the relative importance of the two mechanisms is clearly seen. In general the ionisation process will always be present and as we shall see in a later chapter this mechanism actually forms the basis for the Auger Electron Spectroscopy which is nothing else but the relaxation process following such excitation processes.

The next process is weak and contrary to the two previous energy loss mechanisms only involves losses of small energy quanta. Excitations of excitons or electron-hole pairs are usually very small 0 eV to 2 eV and involve excitations of the valence electrons into the empty conduction band. Thus for a metal this will lead to a rather smooth energy loss feature proportional to the joint density of states between the valence band and the conduction band (see Figure 2.13).

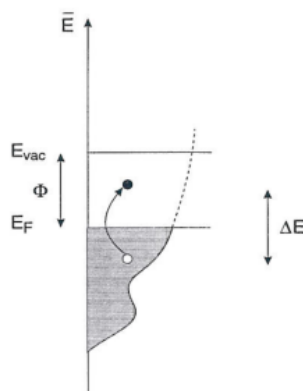


Figure 2.13: Schematics showing excitations of excitons (electron-hole pairs).

The phenomenon may also lead to distinct structures in for example semiconductors where there are distinct bands and a band gap. The same mechanism leads to the so-called Doniach-Sunjić line shapes in the core level spectra observed with XPS as we shall see in Chapter 4.

Another very weak energy loss process is the excitation of phonons or lattice vibrations. The energy quanta involved here are continuous as the phonons form dispersion bands usually below 50 meV. Higher and discrete energy losses can be observed for adsorbed molecules on surfaces depending on the adsorption site and the metal, an adsorbed CO molecule will have an energy loss of 260 meV for instance. This energy loss mechanism is very important for investigations of adsorbed molecules and the method is called High Resolution Electron Energy Loss Spectroscopy (HREELS). An example is shown in Figure 2.14 where a HREELS spectra was measured of formate adsorbed on Cu(100).

The electron energy was only 4.2 eV and the various energy losses are easily identified and an isotope effect can be observed on the C-H stretch vibration when hydrogen is replaced by deuterium. This phonon loss mechanism is not very important in AES and XPS, but it is the mechanism responsible for the well known phenomenon resistivity.

For completeness we shall also mention that electrons which are accelerated will emit radiation [10] and therefore also undergo continuous energy losses when scattered in the solid. It is not identified in the energy loss spectra as it is such a weak effect, but if we consider the radiation from a solid bombarded with high energy electrons it can be observed as indicated

in Figure 4.5.

HREELS of Synthesized Surface Formate on the Cu(100) Surface

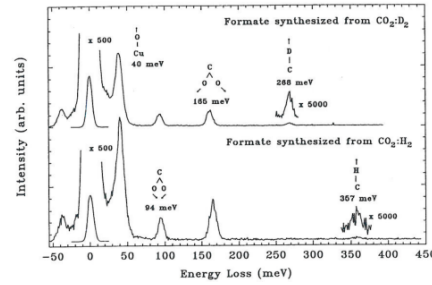


Figure 2.14: Energy loss spectrum of formate adsorbed on Cu(100). The primary energy of the electrons was 4.2 eV and the resolution was 8 meV.

## 2.3 Problems

1. Another type of pump, called a titanium sublimation pump, can be constructed. This pump relies on the high reactivity of titanium. By heating a filament made of a TiMo alloy, Ti will be sublimated out on the surrounding walls (which may or may not be cooled). Assume that a cylinder with a radius of 0.1 m and height of 0.1 m is covered with freshly evaporated titanium. The base pressure in the chamber is  $1 \times 10^{-9}$  mbar.

Estimate the pumping speed of this surface. (Hint: Choose a gas present in the chamber e.g.  $N_2$ )

Are there gases which cannot be pumped by this pump?

In the following we shall assume that the rest gas consist of nitrogen and that the pressure is kept constant. How long time will it take before the pumping speed of the evaporated titanium is reduced to 10 % of its initial speed?

2. Determine the mean free path of a nitrogen molecule at 1 mbar and at  $1 \times 10^{-6}$  mbar. At what pressure is the mean free path smaller than the dimension of an apparatus?
3. Determine the density of valence electrons in Mg and Al. What is the energy of a surface plasmon on metallic Ca?

# Chapter 3

## Energy Analysis

In the following we shall be able to measure the energy distribution of electrons emitted from a surface in the energy range from 10 eV to 2000 eV with a reasonable resolution. The energy analysis is done by electrostatic energy analysers where electrons are selected by a combination of geometry and potentials. Here we shall only consider the two most popular energy analysers, the Concentric Mirror Analyser (CMA) and the Hemi-Spherical Energy Analyser (HSA).

### 3.1 The Concentric Mirror Analyser

The CMA is used mainly for AES where less resolution is necessary, typically 1 eV to 10 eV. The analyser consists of two concentric cylinders as shown in Figure 3.1. The inner cylinder is grounded whilst the outer cylinder is ramped at a negative potential. An electron gun is mounted inside the inner cylinder. In the front there is a defining aperture and the electrons having the appropriate energy defined by the outer cylinder will pass the exit slit and be detected by an electron multiplier. Electrons which do not have the energy defined by the potential difference between the inner and outer cylinder will not be able to pass and are therefore not detected. It can be shown that this set-up is imaging the sample onto the exit slit in front of the channeltron if the geometry is designed correctly. That geometry is obtained if the take-off angle through the entrance slit is  $42.18^\circ$ . Since the analyser has a transmission efficiency of roughly 10% it is a relatively efficient analyser. The only major drawbacks on a CMA is that the sample has to be located



close to the analyser and the limited resolution. If for instance 1000 eV electrons are to be measured with a typical CMA which has a resolution of 0.6% the feature measured at this energy will be 6 eV broad. This is satisfactory for analysis of Auger electrons but certainly not for XPS studies. Higher resolution can be obtained by having two CMA's in series. This is called a Double Pass CMA, but better solutions have been developed.

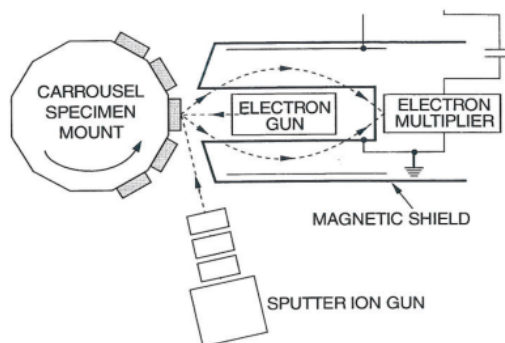


Figure 3.1: Schematics of a CMA.

## 3.2 The Hemi-Spherical Analyser

For XPS there is a demand for an energy resolution better than 1.0 eV or preferably 0.5 eV over a broad energy range, 0 eV to 1500 eV. This is obtainable by applying a different set-up, the so called HSA as shown in Figure 3.2. This analyser consists of two concentric hemi-spheres with an entrance slit and a detector. Usually a lens system will guide the electrons from the sample to the entrance slit by imaging the sample onto the entrance slit. At the entrance slit there is mounted a retarding grid which only allows electrons with a certain energy to pass. The same grid also determines the potential of the central path between the two hemi-spheres. The potential difference between the two spheres determines a pass energy at which electrons will be able to travel through the analyser and be detected at the exit slit where an electron channeltron is mounted. Thus the geometry images the entrance slit on the exit slit.

Again the resolution is a constant percentage of the pass energy (roughly 1%) and it is therefore desirable to only use low pass energies, typically 5 eV

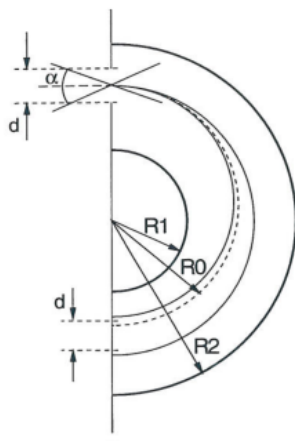


Figure 3.2: Schematics of a HSA.

to 100 eV. On the other hand everything has its price. A high resolution means low signal and thus poor signal to noise ratio. It is therefore always important to realise what level of resolution is necessary.

The electrons that have an energy that allows them to pass through the exit slit are detected by an electron multiplier. This is a ceramic tube covered on the inside with a material from which electrons are easily knocked out (see Figure 3.3).

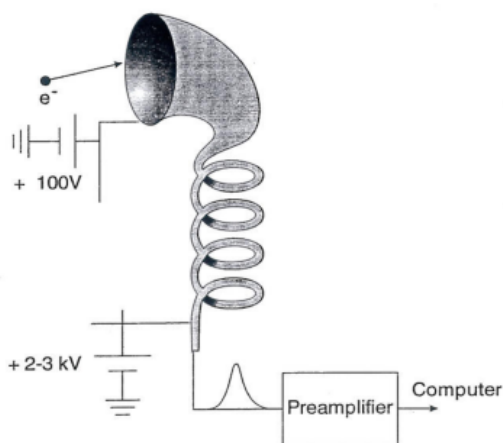


Figure 3.3: Schematics showing an electron multiplier.

The front of the multiplier is typically at 100 V to 200 V while the end is

at 2 kV to 3 kV. Thus electrons are accelerated into the channeltron where they eventually will hit the wall and knock out other electrons which again are accelerated. In this manner a cascade is formed and one electron may become  $10^6$ – $10^7$  in the other end. This is a fairly big pulse which can easily be detected by some preamplifier and converted into a signal that the computer can handle.

The transmission efficiency for both types of analysers depends on the energy of the electrons. Thus when quantitative or comparative studies are undertaken it is important to take into account the transmission function. We shall come back to this under the discussion of quantitative studies of surface composition.

### 3.2.1 Example

Determine what the potential should be on the retarding grid and the two hemi-spheres if we want to detect 1000 eV electrons with a resolution of 0.2 eV with an HSA which has  $R_1 = 0.10$  m and  $R_2 = 0.15$  m.

A resolution of 0.2 eV means that the pass energy should be 20 eV and the retard potential must then be  $-1000 \text{ V} + 20 \text{ V} = -980 \text{ V}$ . This is also the potential right in the middle of the two hemi-spheres  $V_0$ . The electric field between the two hemi-spheres can be found by use of Gauss law

$$\int \vec{E}(r) d\vec{s} = \frac{q}{\epsilon_0} \quad (3.1)$$

by using that

$$\vec{E}(r) = -\vec{\nabla}V(r) \quad (3.2)$$

we can by integration using the appropriate boundary conditions get

$$V(r) = V_0 + \frac{q}{2\pi\epsilon_0} \left( \frac{1}{r} - \frac{1}{R_0} \right) \quad (3.3)$$

where  $R_0 = (R_1 + R_2)/2$ . The force necessary for the orbit motion is supplied by the electric field

$$\vec{F}_c = \vec{F}_E \quad (3.4)$$

leading to

$$\vec{E}(R_0) = \frac{mv^2}{R_0 e} = \frac{2E'_{kin}}{R_0 e} \quad (3.5)$$

where

$$E'_{kin} = E_{kin} - V(R_0)e \quad (3.6)$$

is the kinetic energy of the electron after it has passed the retarding grid. By elimination of  $q$  it is easily found that the potential between the spheres can be described by

$$V(r) = \frac{2E'_{kin}}{e} \left( \frac{R_0}{r} - 1 \right) + V_0 \quad (3.7)$$

In this manner the potential of the inner and outer hemi-spheres is found to be  $-970 \text{ V}$  and  $-988 \text{ V}$  and respectively. Notice that the resolution in this set-up will be constant as we are using constant pass energy.



## Chapter 4

# The XPS Method

X-ray induced Photoelectron Spectroscopy (XPS) relies on a well known principle namely the photo-electric effect, which was explained by Einstein in 1905. When a surface is bombarded with photons with sufficient energy an electron may absorb all the energy of the photon and be able to escape the solid with a kinetic energy reflecting the photon energy as well as the bonding energy of the electron. It was not until in the late sixties that this process was brought into operation by Kai Siegbahn who later received the Nobel prize for his work. The process is illustrated in Figure 4.1

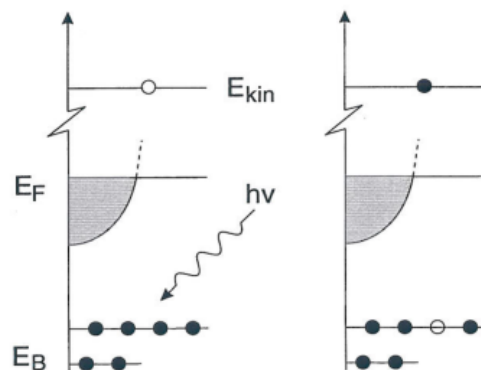


Figure 4.1: Sketch of the photoemission process.

X-rays are generated with a suitable energy so that the electrons, excited from the atoms, have a kinetic energy in the range where high surface sen-

sitivity can be obtained. The kinetic energy of the emitted electron relative to the vacuum level will be given by

$$E_{kin} = h\nu - E_B - \Phi \quad (4.1)$$

where  $h\nu$  is the photon energy of the X-ray,  $E_B$  is the binding energy of the electron in the solid referred to the Fermi level, and  $\Phi$  is the work function for the solid. It is obvious that if we can generate a monochromatic source of X-rays it is possible to map out the electron density as a function of binding energy by measuring the kinetic energy of the emitted electrons. Since the electron density as a function of binding energy is characteristic for each element this is a useful method to determine not only which elements are present in the surface but also how much there is of each. Furthermore, small shifts in the measured binding energy reflect changes of the chemical state of the elements. The XPS method has therefore also been called Electron Spectroscopy for Chemical Analysis (ESCA).

## 4.1 X-ray Sources

When a material is bombarded with electrons there will, as we saw in Chapter 2, be possibilities for ionisation of the atoms in the material. The excited atom will after a very short time relax by a process where a weakly bound electron is dropping down into the created vacancy. The energy released by this process can now be used to either excite another bound electron out of the atom (an Auger process) or in this case more interesting to emit a photon. In Figure 4.2 a dual anode is shown which is bombarded with 15 keV electrons.

A thin aluminium foil is mounted just in front of the anode in order to prevent stray electrons and outgassing to the rest of the chamber.

The process is shown for an aluminium atom in Figure 4.3. Initially a hole is formed in the 1s level. The atom may now relax by either letting an electron from the  $2p_{\frac{3}{2}}$  or  $2p_{\frac{1}{2}}$  fall down and emit a photon. The energy splitting between the two p levels is due to spin-orbit coupling and is very small (0.4 eV to 0.5 eV).

Unfortunately, the short lifetime of the excited states involved will also influence the widths of the emitted X-rays. The relations are given through the Heisenberg uncertainty relation for energy and time

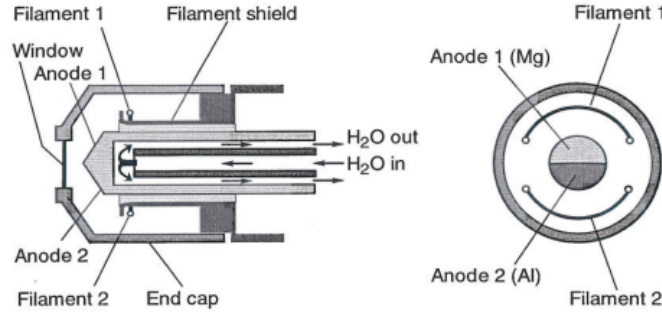
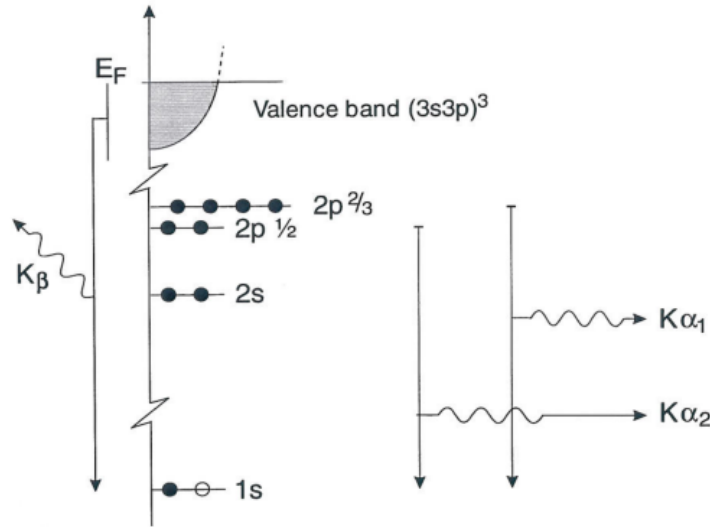


Figure 4.2: Schematics of a commercial dual X-ray anode.

Figure 4.3: Sketch of the transitions in aluminium leading to the  $\text{Al}_{K\alpha}$  radiation.

$$\Delta E \Delta t \geq \frac{h}{2\pi} \quad (4.2)$$

and leads to, as shown in Figure 4.4, a broadening of 0.7 eV for each of the two lines [11]. Thus the X-ray emitted by this transition will effectively be one line which will be roughly 1.0 eV broad at Full Width Half Maximum (FWHM) with an energy of 1486.6 eV.



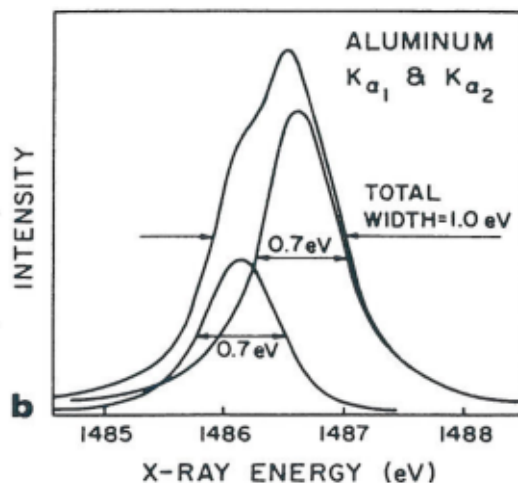


Figure 4.4: The line width of the  $K_{\alpha 1}$  and  $K_{\alpha 2}$  resulting in the  $K_{\alpha 12}$  line [11].

Due to an old X-ray notation this transition is called an  $\text{Al}_{K_{\alpha 12}}$  line indicating that a hole is generated in the  $K$  shell (main quantum number one i.e.  $1s$ ). A quite similar transition exists in magnesium which is a bit more narrow ( $0.7 \text{ eV}$ ) and has an energy of  $1253.6 \text{ eV}$ . Many other materials may be used as anodes as shown in Table 4.1, but in general  $\text{Mg}$  and  $\text{Al}$  are the preferred species to have on a dual anode as shown in Figure 4.2.

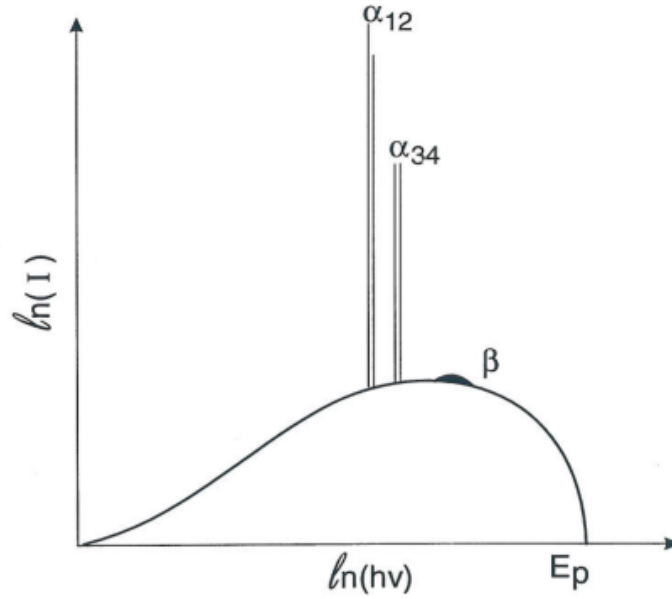
The reason being that a narrow line is desired in combination with sufficient energy in order to be able to reach several core levels in the sample material.

Usually the  $\text{Al}_{K_{\alpha 12}}$  and  $\text{Mg}_{K_{\alpha 12}}$  are sufficient for most purposes, but when detailed studies are necessary it is important to consider the quality of the X-ray source as there will be other possibilities for transitions in the anode. Figure 4.5 shows the number of photons emitted from an aluminium anode as a function of photon energy when it is bombarded with  $E_p = 15 \text{ keV}$  electrons schematically.

There will be a continuously weak background of photons due to the deceleration of the electrons in the anode. Besides this there is a strong and a discrete contribution from the  $1s$ - $2p$  transition as discussed above. However, other transitions can also be observed. This is illustrated in Figure 4.6 where the number of photons from a magnesium anode is plotted against energy

Table 4.1: Energies and FWHMs of various X-ray transitions.

X-ray line	Energy [eV]	FWHM [eV]
$\text{Mg}_{K_\alpha}$	1253.6	0.70
$\text{Al}_{K_\alpha}$	1486.6	0.85
$\text{Si}_{K_\alpha}$	1739.5	1.2
$\text{Zr}_{L_\alpha}$	2042.4	0.77
$\text{Ag}_{L_\alpha}$	2984	< 3
$\text{Ti}_{L_\alpha}$	4511	1.4
$\text{Cr}_{L_\alpha}$	5414.7	1.8
$\text{Cu}_{L_\alpha}$	8048	2.5

Figure 4.5: Sketch of the X-ray emission spectrum for an anode bombarded with high energy ( $E_p$ ) electrons.

measured relative to the  $\text{Mg}_{K_{\alpha 12}}$  line. The  $\alpha_{34}$  lines are due to a double ionisation of the magnesium atom and are located approximately 10 eV above [12]. The  $\beta$  line is due to a transition where a valence electron falls down to the 1s shell and occupies a hole. Usually the  $\beta$  is so weak that it is rarely

noticeable.

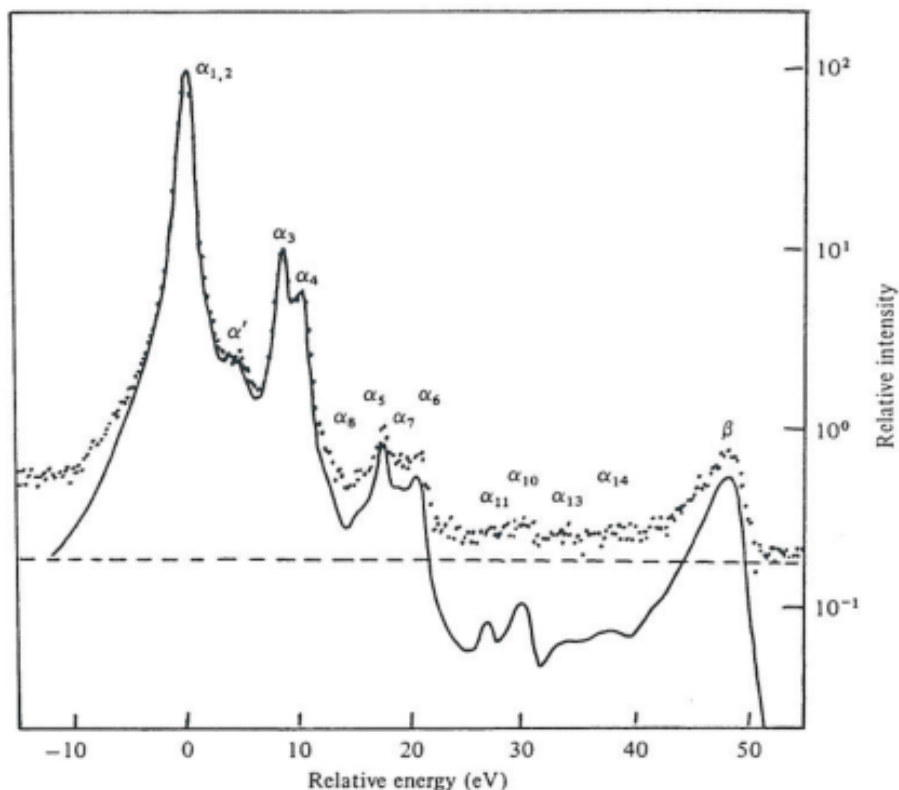


Figure 4.6: The relative intensity of X-rays emitted from a magnesium anode plotted relative to the  $K_{\alpha 12}$  energy. Notice that the intensity is on a logarithmic scale [12].

Shown in Table 4.2 are the X-ray satellite lines of magnesium and aluminium positioned relative to the main lines. Notice that more than 10 % to 15 % of the X-ray intensity will be in the different satellite structures. All these various problems with different X-ray lines can be avoided if we let the X-ray pass a monochromator. This is easily established by diffraction of the X-rays in a Si single crystal. The only major drawback using this procedure is the extensive loss of sensitivity (actually photon intensity) and naturally the investments. Therefore another approach is used when high resolution is called for.

Table 4.2: Relative intensity and shift of various satellite lines compared to the main line.

X-ray Line	Shift [eV]	Relative Intensity [%]
$\text{Mg}_{K_{\alpha 12}}$	0.0	100
$\text{Mg}_{K_{\alpha'}}$	4.5	1.0
$\text{Mg}_{K_{\alpha 3}}$	8.4	9.2
$\text{Mg}_{K_{\alpha 4}}$	10.0	5.1
$\text{Mg}_{K_{\alpha 5}}$	17.3	0.8
$\text{Mg}_{K_{\alpha 6}}$	20.5	0.05
$\text{Mg}_{K_{\beta}}$	48.0	2.0
$\text{Al}_{K_{\alpha 12}}$	0.0	100
$\text{Al}_{K_{\alpha'}}$	5.6	1.0
$\text{Al}_{K_{\alpha 3}}$	9.6	7.8
$\text{Al}_{K_{\alpha 4}}$	11.5	3.3
$\text{Al}_{K_{\alpha 5}}$	19.8	0.4
$\text{Al}_{K_{\alpha 6}}$	23.4	0.3
$\text{Al}_{K_{\beta}}$	70.0	2.0

By using synchrotron facilities it is possible to obtain an extremely brilliant source of X-rays in a broad spectrum of energies (10 eV to 1000 eV). The radiation is formed by confining high energy electrons (5 GeV) into a storage ring, a so-called synchrotron. Accelerated electrons will emit radiation. By establishing suitable monochromators it is possible to select the desired photon energy. This has many advantages experimentally since the photon energy is tuneable (meaning it is possible to select a photon energy where maximum surface sensitivity is obtained) and the broadening can be controlled. The only major drawback on this type of equipment is that it is huge and expensive facilities, located only a few places in Europe.

## 4.2 Spectral Interpretation

Now all the equipment has been established for doing the XPS experiment. A typical XPS spectrum of Cu(100) is shown in Figure 4.7 where the source is the  $\text{Al}_{K_{\alpha 4}}$  radiation from a conventional dual Al/Mg X-ray source. The observed spectrum is a mapping of the energy levels in copper. The features

at the highest kinetic energy, i.e. zero binding energy, are from the valence region of copper. This is not very intensive and can hardly be seen.

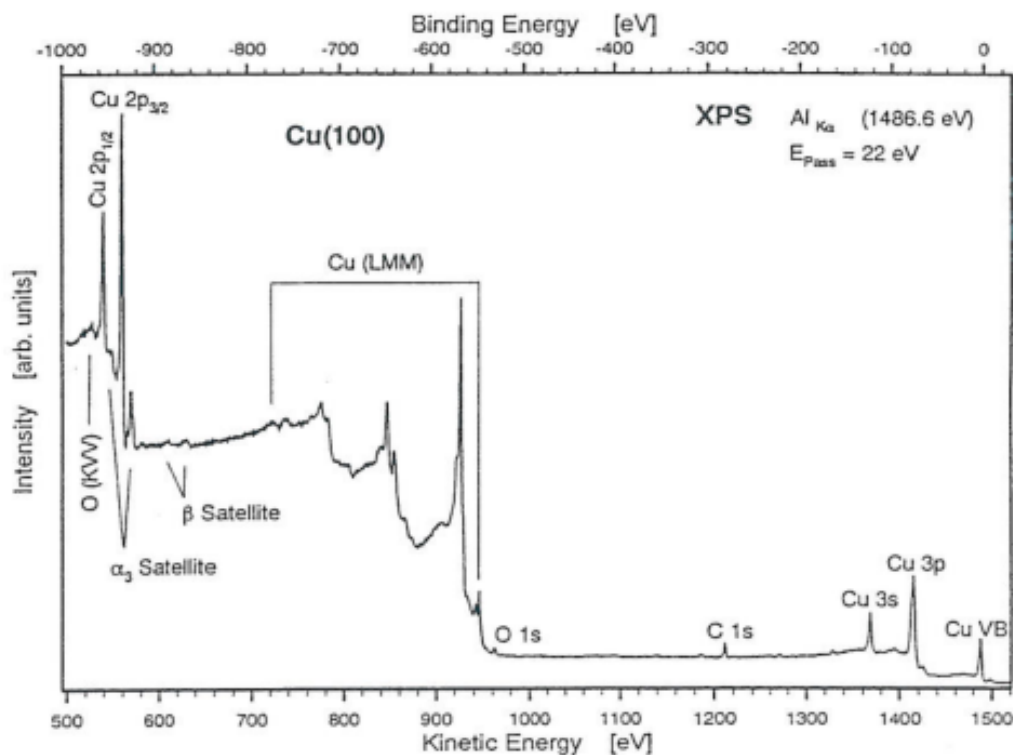


Figure 4.7: XPS spectrum of a Cu(100) surface measured using a HSA analyser.

The small feature that is seen here is the 3d level lying just below the Fermi level. Proceeding towards higher binding energies the 3p and 3s levels around 65 eV and 110 eV respectively. The Auger lines follow naturally from the relaxation of the holes that has been created by the photoemission process. They are not very interesting in this context and we shall leave the discussion of these to the next chapter. At even higher binding energies we find first the  $2p_{3/2}$  and then the  $2p_{1/2}$  lines. Contrary to the 3p line the spin orbit splitting is very obvious and amounts to roughly 20 eV. This splitting will be present for all subshells with an angular momentum higher than zero. Thus the only lines where no splitting should be expected are the lines due

to excitations of s electrons. For careful studies of the surfaces it may be informative to take a closer look at the high energy region of the spectrum as shown in Figure 4.8. It is now easily seen that this surface is contaminated as all the lines cannot be accounted for by copper. Carbon, oxygen and sulphur are easily identified in non-vanishing amounts. Furthermore, it is also possible to identify ghost-peaks from the  $Mg_{K\alpha}$  anode, which are excited when the aluminium source is used. Even some  $\beta$  satellites from the  $Cu_{2p}$  lines can be observed. All such features has to be accounted for in a detailed XPS study.

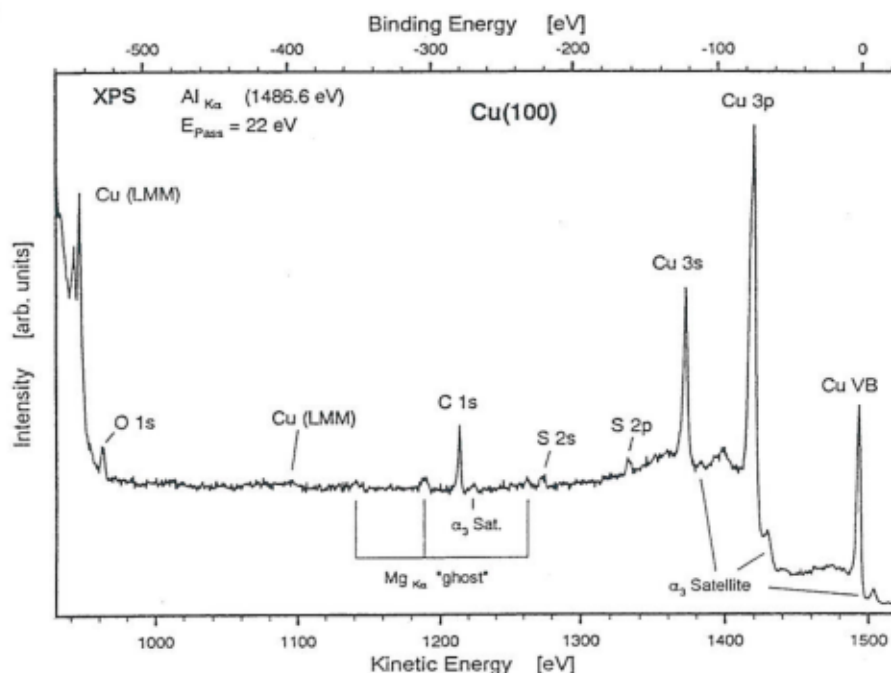


Figure 4.8: As Figure 4.7 but rescaled and only showing the region above 965 eV kinetic energy.

### 4.2.1 Multiplet splitting in XPS

To understand the various features observed by XPS we must look a little into atomic physics. In the following we shall treat all atoms as if they

initially have filled shells, i.e. we will disregard the valence electrons which are highly delocalised in metals. All the electron energy levels can now be determined by finding a solution to the Schrödinger equation with the appropriate Hamiltonian. This can be done iteratively by a self consistent Hartree-Fock calculation. In this case all electron energy levels like 1s, 2s, 2p, 3p, and 3d for the copper atom will be degenerate. This state will in the following be referred to as the *initial state*. This degeneracy of a level will be lifted if an electron is being excited out of the atom leaving a hole in a subshell, say, 2p. The same calculation has to be performed for this system, now referred to as the *final state*, but now the spin-orbit interaction also has to be taken into account since we have an unpaired hole<sup>1</sup>. The spin-orbit coupling is treated as a perturbation of the system and in the present case it is convenient to formulate a new quantum number  $j$  instead of the angular momentum  $l$  and the spin  $s$  as  $\vec{j} = \vec{l} + \vec{s}$ . As  $\vec{s}$  only can take the values  $+\frac{1}{2}$  and  $-\frac{1}{2}$  and as  $j$  only can take the values

$$l + s \geq j \geq |l - s| \quad (4.3)$$

it is obvious why there will always be a splitting for levels with  $l \neq 0$ . The intensity distribution in the two lines will be given by the degeneracy in the two final states which is  $2j + 1$ . Thus the intensity ratio between the two 2p lines observed in Figure 4.7 is 4:2. The same formalism can be used to understand the splitting observed in the 2p, 3d, and 4f shells shown in Figure 4.9 [11].

This was for the simple case where open shells could be neglected, but that is not always the case. If we consider the rare earth metals (which by no means are rare) the 4f shell will be very localised on the atom although it is weakly bound. This is due to the lanthanide contraction and the same phenomenon applies to the actinides. Thus when going through the lanthanide's series where the 4f shell is being filled, the chemistry is not changing because the outermost electron configuration is basically not changing. This also has a strong influence on the observed XPS spectra of these metals. Figure 4.10 shows one of the relatively simple examples of multiplet splitting [13].

In the top panel of Figure 4.10 the 4d region of pure ytterbium is shown. As it has the electron configuration  $[\text{Xe}]4f^{14}6s^2$  it is a divalent metal with otherwise filled shells. Thus the 4d region should just show a simple  $4d_{\frac{5}{2}}$  and

---

<sup>1</sup>A missing electron in an otherwise full shell is equivalent to having only one electron in an otherwise empty shell, except that the spin-orbit interaction changes sign.

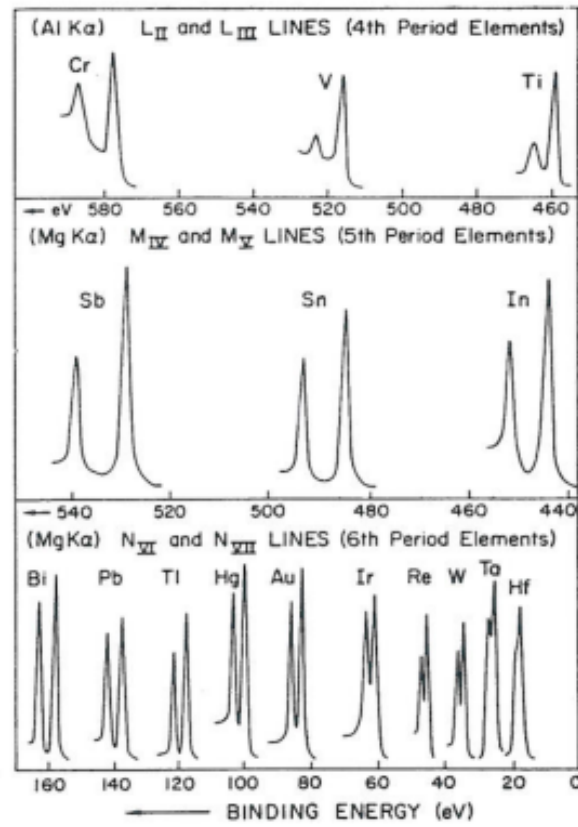


Figure 4.9: The XPS spectra of a variety of elements showing the development in spin-orbit splitting for the 2p, 3d and 4f levels.

$4d_{3/2}$  splitting. At first glance it looks like it does not have the correct intensity distribution, but this can easily be explained by the background of electrons that has undergone energy losses from deeper layers. The background can be estimated as a solid line as shown in Figure 4.10 by studying the energy loss spectra of pure Yb. In order to get a clear view of the feature it has been subtracted and the "true" spectrum is shown in Figure 4.11 together with a fit taking into account the appropriate X-ray satellites [13].

The fit is quite reasonable although not perfect. The reason for the discrepancy is that intrinsic energy loss mechanisms are not included in the background subtraction which is only dealing with the transport of electrons



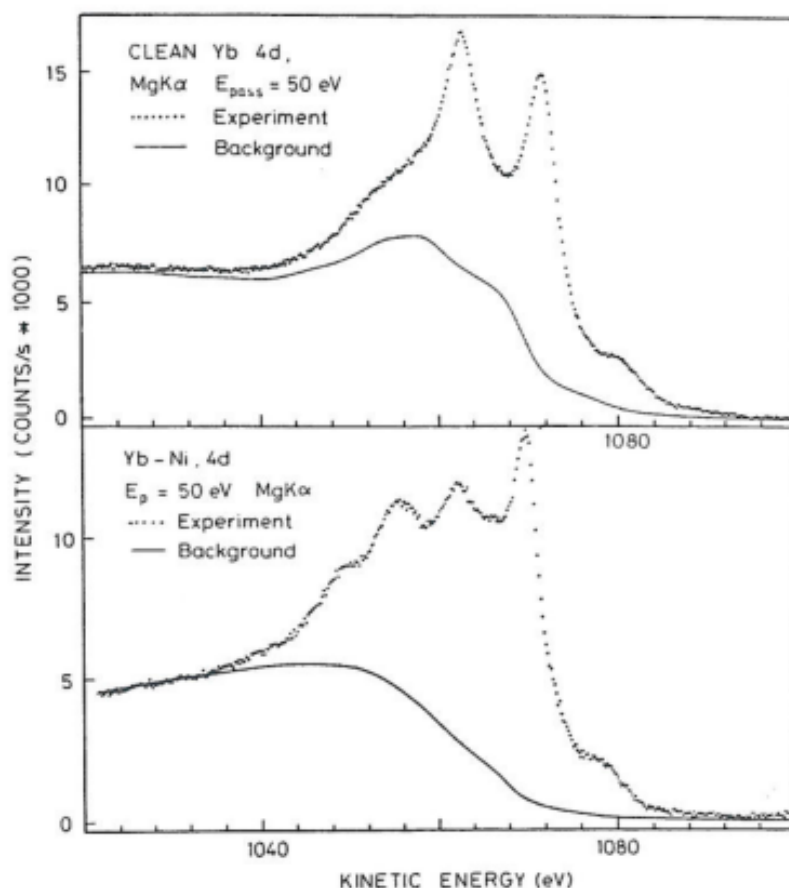


Figure 4.10: XPS spectrum of a) pure Ytterbium and b) an Ytterbium-Nickel alloy. The fully drawn line represents the background due to inelastic energy losses during the transport.

out of the material.

Now if ytterbium is evaporated onto nickel and the sample is heated slightly an alloy is formed and the Yb 4d region changes completely as shown in the lower panel of Figure 4.10 and Figure 4.11. This change can be understood in terms of a change of valence of Yb from being divalent to becoming trivalent. A trivalent Yb atom will initially have a hole in the 4f shell so the final state after the photoemission process will be an atom with a hole both in the 4f shell and one in the 4d shell. These two holes will interact

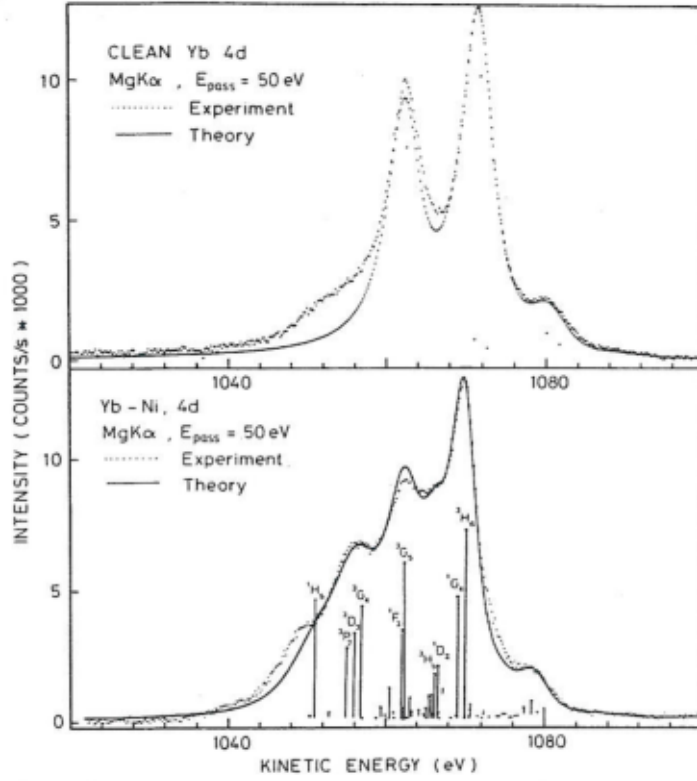


Figure 4.11: The background corrected spectra of Figure 4.10 shown together with theoretical fits relying on multiplet splitting.

strongly through electrostatic interaction. This sort of interaction is treated well through the so-called Russell-Saunders coupling scheme or LS-couplings scheme where the two angular moments  $l_1$  and  $l_2$  are coupled to  $L$  and similar for the two spin values. This immediately leads to large numbers of different final states,  $L = 1, 2, 3, 4, 5$  and  $S = 0, 1$ , which usually are described through the terms

$$^1P, ^3P, ^1D, ^3D, ^1F, ^3F, ^1G, ^3G, ^1H, ^3H$$

a number of singlet or triplet states ( $^{(2S+1)}X$ ). All these ten terms have different energies and will therefore appear in the spectrum. However, this is not all. We have not considered the spin orbit coupling. When that is taken into account  $l$  and  $s$  are no longer good quantum numbers. By treating

the spin-orbit coupling as a perturbation a new set of eigenvalues can be developed on the basis set of  $L$  and  $S$  states and the new coupling scheme will be the so- called intermediate coupling scheme where  $\vec{J} = \vec{L} + \vec{S}$  are the good quantum numbers. The result of this extra perturbation is that the degeneracy of the triplet states is lifted and each of these splits up in three different states. There will now be 20 final states

$$^1P_1, ^3P_0, ^3P_1, ^3P_2, ^1D_2, ^3D_1, ^3D_2, ^3D_3, ^1F_3, ^3F_2, ^3F_3, ^3F_4, ^1G_4, ^3G_3, ^3G_4, ^3G_5, ^1H_5, ^3H_4, ^3H_5, ^3H_6$$

The intensities for the various final states are not given by a simple expression due to the mixing of various  $LS$  states. All these and the appropriate  $\alpha_{34}$  X-ray satellites are taken into account in Figure 4.11 and a good fit is obtained. Thus XPS is very useful for determination of the electronic configuration in such cases.

Figure 4.12 shows the valence band region of Yb studied with a synchrotron facility where the photon frequency is tuneable [14]. The valence electrons  $(6s6p)^2$  can just be observed for the lowest photon energies as a step function at the Fermi level. In this region we should expect a simple doublet resulting from the filled 4f shell, however two doublets are observed.

By increasing the photon energy it is clearly seen that the doublet at the higher binding energy disappears. If we choose to look at the same region with XPS we actually only observe a single doublet. This shows how the surface sensitivity changes with energy (see Fig. 4.13) [14]. The electrons are in this case essentially emitted with the photon energy and we should therefore expect low surface sensitivity when the photon energy is high. Thus the doublet observed at high energy is due to signal from the bulk of the material, whereas the extra doublet observed at low photon energy is due to the surface region. As we shall see, the bonding energy of the electron is dependent not only on the atom and its electron configuration, but also on the chemical surroundings of the atom. In this case the surface atoms are missing a number of neighbours compared to those sitting in the bulk. They will therefore be located in a different electron density which will change the energy of the emitted electron from the bulk value. The observed spectra shown in Figure 4.12 allows for an estimation of the inelastic mean free path which in the present case was found to be roughly 4 Å at 20 eV and 10 Å at 180 eV.

The alloying and change in electron configuration of the Yb could just as well have been studied by following the region of the 4f electrons. This

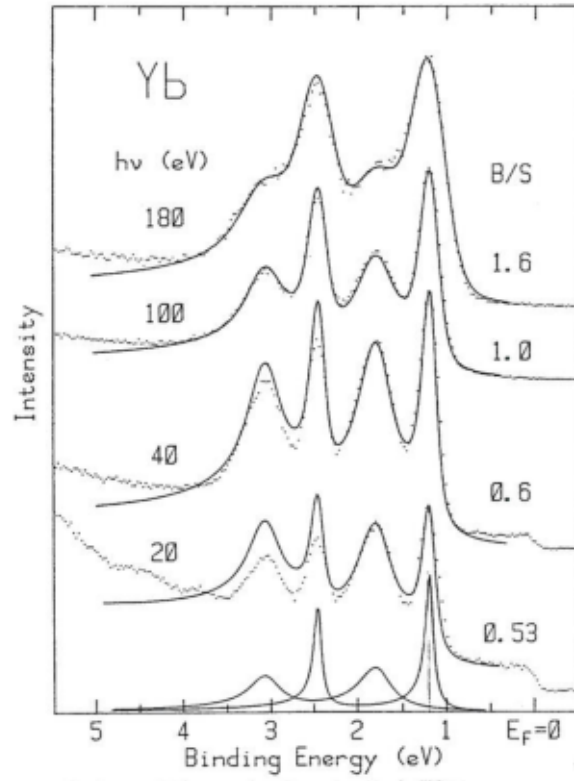


Figure 4.12: The valence band region of ytterbium excited by synchrotron light with increasing energy [14].

demonstrates how surface reactions between metals can be followed quite nicely especially if monochromatised synchrotron light is used.

### 4.2.2 The Binding Energy in XPS

Since the binding energy of the various shells is characteristic for each element, as can be seen from Figure 4.14, this in itself allows for identification of the elements. In the previous section we assumed that the kinetic energy of the emitted electron was given by

$$E_{kin} = h\nu - E_B - \Phi \quad (4.4)$$

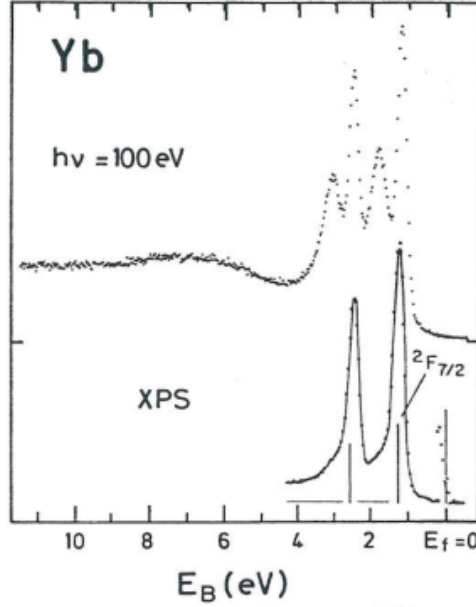


Figure 4.13: Comparison between the valence band region of ytterbium excited by 100 eV photons and by  $\text{Al}_{K\alpha}$  radiation [14].

In the following we will disregard  $\Phi$  and concentrate on the binding energy  $E_B$ . It was earlier assumed that the electron configuration of the atom (except for some splitting) did not change by the photoemission i.e. the energy of all other electrons is the same as before the photoemission process. This energy is referred to as the Koopman's energy. However, this is never observed because the atom is a dynamical system which immediately relaxes during the process screening out the hole made in the core level. Thus higher lying electrons will in principle feel the core change from  $Z$  to approximately  $Z + 1$  whereby they will obtain a higher binding energy. The relaxation will result in a photoelectron with a higher kinetic energy. The gain in energy we shall call the atomic relaxation,  $E_{ar}$ . Including this term the kinetic energy for an atom will be

$$E_{kin} = h\nu - E_B + E_{ar} \quad (4.5)$$

This is only true if the photoemission process is an adiabatic process, i.e. the emission process is slow enough for equilibrium to be obtained. This

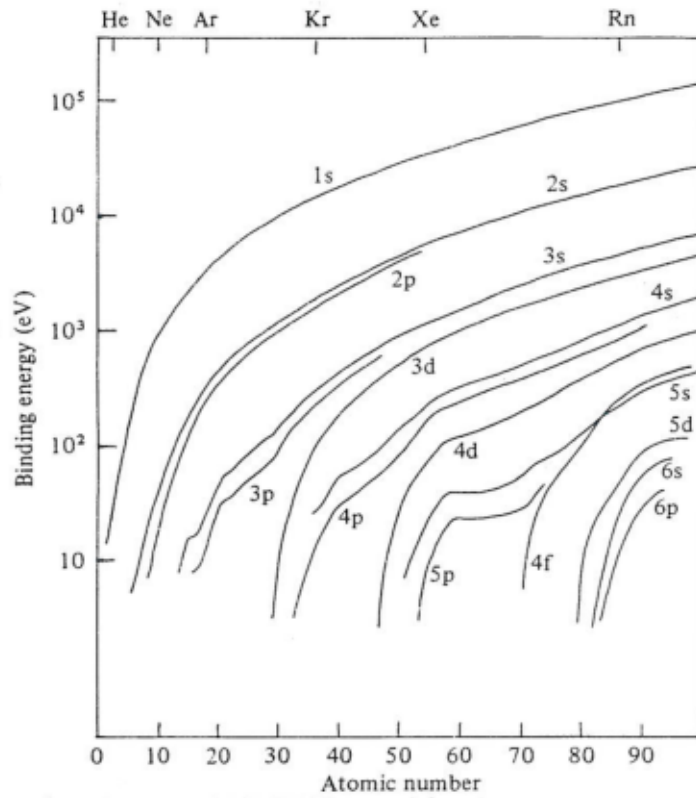


Figure 4.14: The binding energy for a broad variety of levels as a function of atomic number [11].

is not true for the photoemission process where the sudden approximation scheme is much more applicable. All electrons will feel a sudden change in potential which may sometimes lead to excitations of other electrons in the atom. As the ionised atom may now be left in an excited state there will be less energy for the emitted photoelectron and a lower kinetic energy will be measured. The result will therefore be that a number of satellites which will be observed towards lower kinetic energy. An example of such a phenomenon is shown in Figure 4.15 where the Xe 3d spectrum is shown.

The two parent lines are easily identified, but notice the rich structure towards the higher binding energy, which is mainly due to a simultaneous excitation of the 5p electrons to various empty levels. This process is called

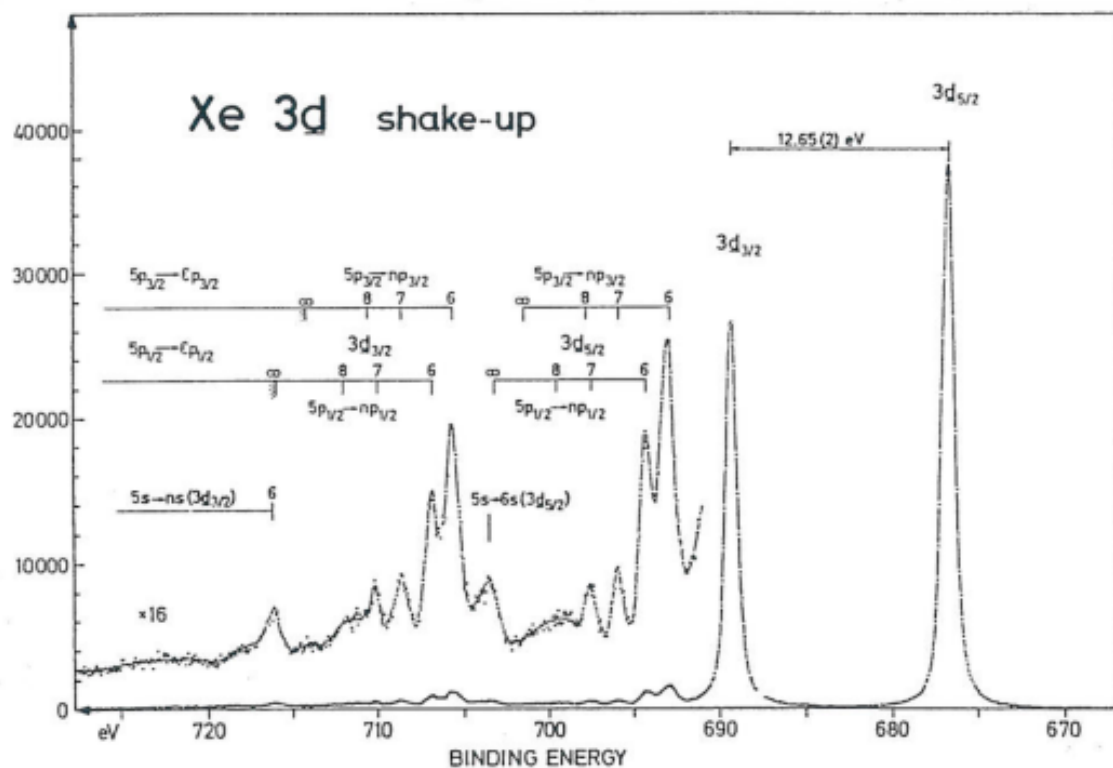


Figure 4.15: The 3d region of atomic Xe clearly showing shake up-satellites [11].

a shake-up process as the electrons are excited to bound states. If they are excited to the continuum they are called shake-off satellites. The real origin of this phenomenon we shall find in the many-body description of the atom. In an accurate description of an atom it is usually necessary to invoke Configuration Interaction (CI). Neither the initial state ( $\Psi_i$ ) nor the final state  $\Psi_f$  can be described by a single electron configuration but are described by a linear combination of wave-functions for different configurations with different energies. Thus when forming the matrix element for finding the transition probability there will be possibilities for some atoms to have strong components of various electron configurations as seen in Figure 4.15. In most cases only configuration interaction has to be considered for the final state.

For further details on this effect the reader is referred to [15].

Let us now consider an atom embedded in a metal. Naturally we will still have the atomic relaxation but now another effect will also influence the kinetic energy of the photoelectron. The weakly bound and delocalised valence electrons will be able to respond swiftly to the potential changes set up by the photoemission process. Charge will flow in and screen the emitted electron from the ionised atom resulting in a higher kinetic energy (see Fig. 4.16).

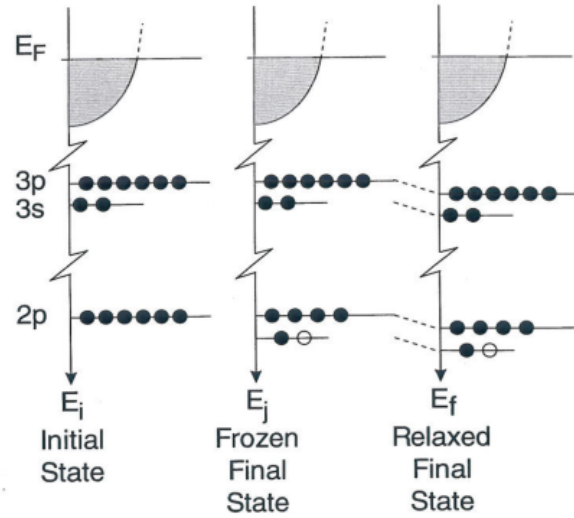


Figure 4.16: Sketch showing the effect of extra atomic relaxation in a metal.

This contribution shall be called extra atomic relaxation  $E_{ear}$  which results in the kinetic energy

$$E_{kin} = h\nu - E_B + E_{ar} + E_{ear} \quad (4.6)$$

The size of  $E_{ar}$  and  $E_{ear}$  can be up to 10 eV to 15 eV so a substantial difference between the spectra of an element in the vapour phase and in the solid state can be observed (see Fig. 4.16). Just as in the atomic case the sudden approximation may lead to excitation of various states. As we are considering a solid there will be no discrete levels above the Fermi level but a band structure so that the CI-picture is not appropriate. Instead we can just consider some of the energy loss mechanisms we discussed in



Chapter 2. Excitations of excitons is equivalent to the shake-up satellites and also excitations of plasmons may be observed. These intrinsic energy losses have to be distinguished from those observed in conjunction with the transport of the electrons through the solid which we shall call extrinsic energy losses. In Figure 4.10 we subtracted a background due to the transport of the electrons through the Yb. However, some discrepancy is still observed in the background corrected spectra when fitted with a theoretical line shape. The observed discrepancy can be explained by a so-called intrinsic energy loss to a plasmon created by the sudden potential change during the photo emission process. The effect of intrinsic excitons are naturally very difficult to separate experimentally from the extrinsic, but they can easily be observed in for instance the Pt 4f spectrum shown in Figure 4.17 [16].

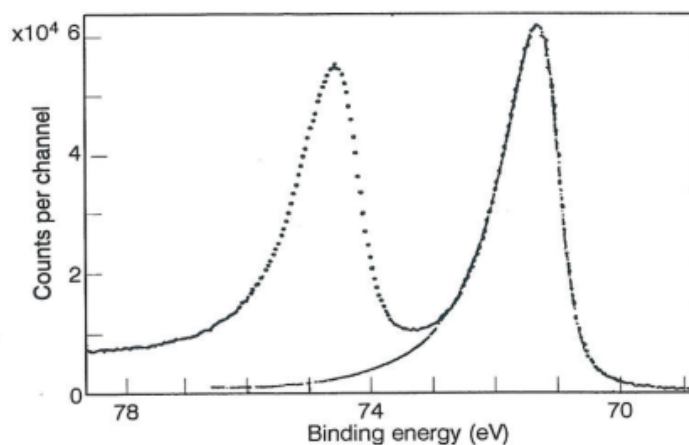


Figure 4.17: The 4f region of platinum displaying an asymmetrical peak shape.

A priori a Lorentzian line shape is to be expected as the broadening primarily is determined by the lifetime of the final state. It is, however, clearly seen that the two lines are slightly asymmetrical towards lower kinetic energy. Usually this sort of line can be fitted by a Doniach-Sunjic line shape which is asymmetrical [17] and explained by excitations of excitons.

The separation of the lines in their different components is very important for obtaining a high accuracy on quantitative determinations of surface compositions. It is therefore very important to understand the origin of the

various effects.

So far we have only discussed the influence of the final state on the binding energy. Different chemical surroundings will also affect the initial state as the electron configuration and density around the atom will be changed. This change in binding energy related to various chemical surroundings is called the chemical shift. However, the final state will also be sensitive to the chemical state of the atom. Thus the phenomenon can only be separated in an initial and a final state effect from a theoretical point of view. The kinetic energy can formally be written as

$$E_{kin} = h\nu - E_B + E_{ar} + E_{ear} + E_{chem} \quad (4.7)$$

where  $E_{chem}$  is dependent on the surroundings of the atom.

An example of a chemical shift is illustrated in Figure 4.18 where the 2p region of Ti and TiO<sub>2</sub> are depicted [18].

It is clearly seen that the Ti 2p lines are shifted roughly 4.5 eV towards higher binding energy by oxidation into TiO<sub>2</sub>. This sort of data has been measured for a number of chemical compounds and the results are shown in Figure 4.19 for Ti [18].

Notice how the binding energy increases with increasing electronegative neighbours. Such information only gives an indication of the chemical state of a surface, but in combination with the possibility to identify which elements are present else and how much, this can be valuable information. One area where the chemical shift plays a strong role is within the field of polymer research where it can be used to identify the role of functional groups and their behaviour by adhesion. As an example the XPS spectrum of ethyltrifluoroacetate (C<sub>4</sub>H<sub>5</sub>F<sub>3</sub>O<sub>2</sub>) is shown in Figure 4.20 where four lines of carbon are easily identified [19].

Sometimes the chemical shift will also be followed by a change in the availability to excite different satellites. This is clearly seen from Figure 4.21 where the copper 2p region undergoes a chemical shift of roughly 1 eV by oxidation, but at the same time a strong feature with equal intensity to the main line is observed at 10 eV higher binding energy [18].

### 4.2.3 Line Width

Especially when chemical shifts and electron structures are studied it is important to consider the line width of the XPS lines. Ideally both the energy

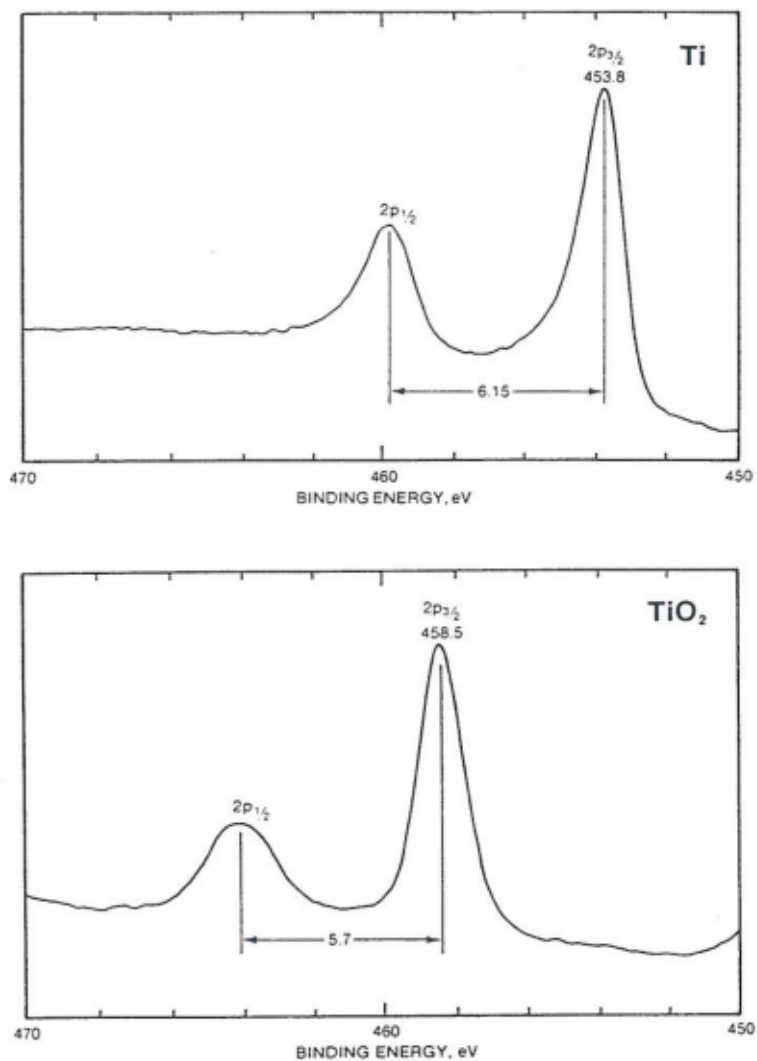


Figure 4.18: The chemical shift of Ti upon oxidation [18]

distribution of the X-ray line and the energy distribution of an emitted electron should be given by the lifetime of the holes left behind (if we disregard any contribution from intrinsic and extrinsic energy losses) and the line shape should therefore be described by a Lorentzian which has the form

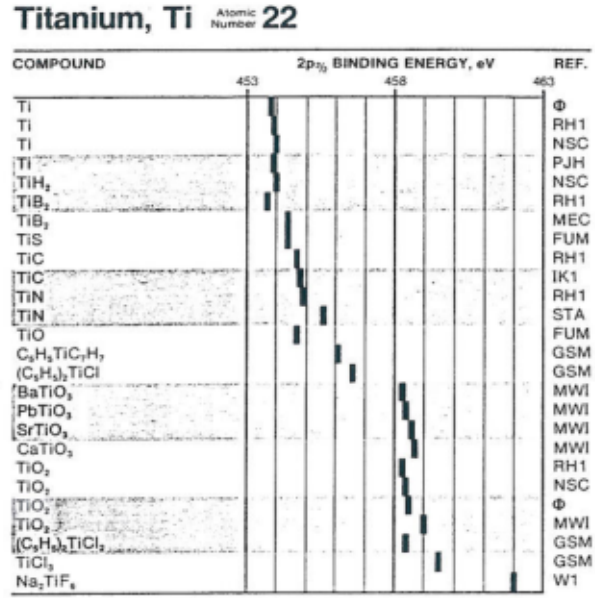


Figure 4.19: The Ti 2p line position for various chemical compounds [18].

$$L(E) = \frac{A}{(E - E_0)^2 + \frac{\Gamma^2}{4}} \quad (4.8)$$

where  $\Gamma$  corresponds to the FWHM. If there were no other sources of broadening the lines than these two, the resulting XPS line shape would be given by

$$P(E) = L_{X\text{-ray}}(E) * L_{\text{Photoemission}}(E) \quad (4.9)$$

where  $*$  refers to a convolution of the two line shapes. The analyser will, however, also always contribute to the broadening of the observed lines. This broadening can usually be described adequately by a Gaussian line shape

$$G(E) = B e^{-\frac{4 \ln(2)(E - E_0)^2}{\Gamma^2}} \quad (4.10)$$

where  $\Gamma$  again corresponds to the FWHM. Thus in order to find the resulting line shape the line shape  $P(E)$  also has to be convoluted by  $G(E)$

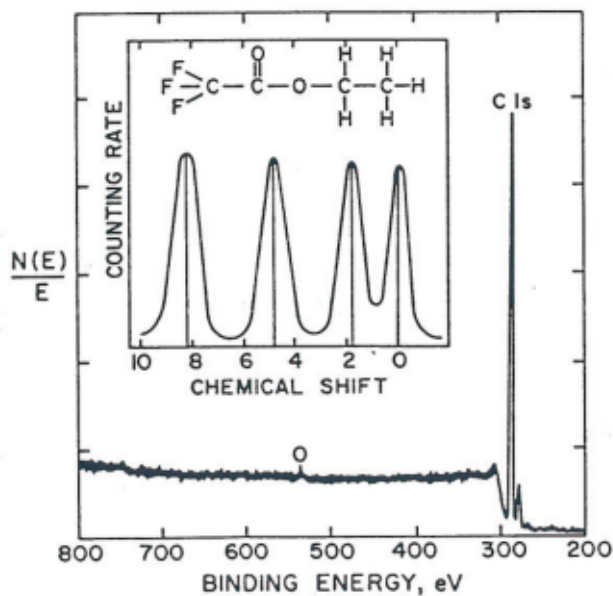


Figure 4.20: The chemical shifts of carbon in ethyltrifluoroacetate.

$$R(E) = P(E) * G(E) \quad (4.11)$$

The resulting line shape  $R(E)$  can be approximated by a Gaussian and the resulting FWHM can be approximated by

$$\Gamma_{res} = \sqrt{\Gamma_{X-ray}^2 + \Gamma_{Photoemission}^2 + \Gamma_{Analyser}^2} \quad (4.12)$$

If for example  $\Gamma_{X-ray} = 0.85$  eV and  $\Gamma_{Photoemission} = 0.5$  eV it would then not be meaningful to press the resolution of the analyser much below 0.5 eV since this would just lead to loss of signal without any significant gain in resolution. As the signal to noise ratio ideally will be proportional to  $\sqrt{Intensity}$  it is important always to counter-balance resolution and intensity.

#### 4.2.4 The Transition Probability

The probability for excitation of an electron from an atom when interacting with an X-ray photon can be described in quantum mechanics as an interaction between the initial and final state through an interaction Hamiltonian.

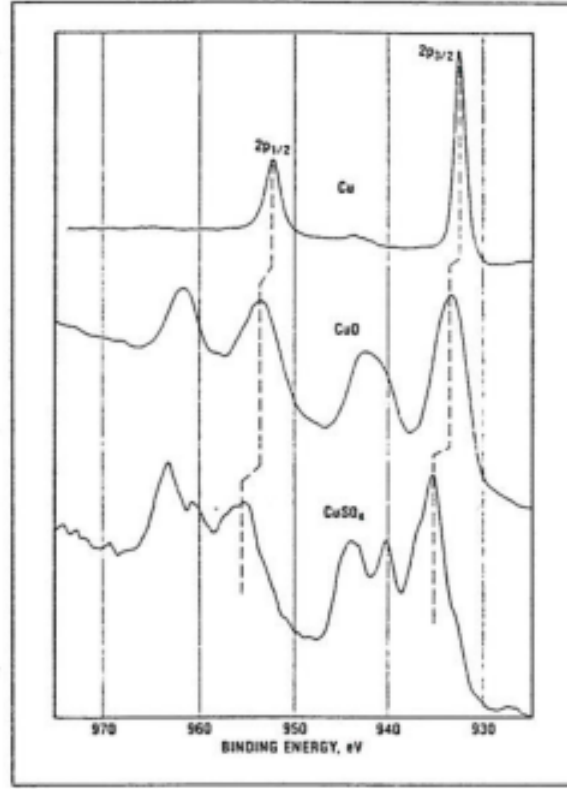


Figure 4.21: The chemical shift of copper and the satellite structure [18].

This Hamiltonian can be approximated by the time-dependent electric field and the problem can be solved by use of time-dependent perturbation theory leading to Fermi's Golden rule:

$$P \propto | \langle \Phi_{initial} | H_{int}(t) | \Phi_{final} \rangle |^2 \quad (4.13)$$

By such a calculation it is possible to estimate the cross section per X-ray photon to excite a photoelectron. The cross section is dependent on the photon energy and is, as can be seen from Figure 4.22 also very dependent on which shell is considered. The above calculation relies on the assumption that the initial and final states can be described by one electron wave functions, though it should not be expected to be very accurate. It will for example

not be able to describe many-body effects like the shake-up and shake-off satellites, but it gives a good indication of which photoemission lines are accessible.

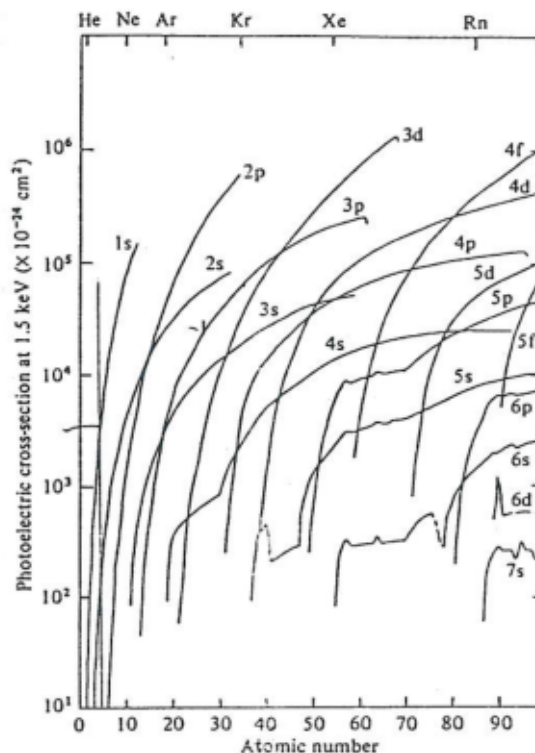


Figure 4.22: The calculated cross-sections for 1.5 keV photons for various levels as a function of atomic number [20].

It is obvious, from Figure 4.22, that it will be very difficult (= impossible) to measure the photoemission lines of hydrogen and helium by  $\text{Al}_{K\alpha}$  radiation. Concerning the satellites, there exists a sum rule saying that the cross section determined by the above one electron approximation equals the cross section for all the possible satellites and the parent line in the many body picture. Thus if strong satellites are involved, like seen in the copper oxide, special care should be taken using these calculated cross sections. Due to the various uncertainties of the calculated cross section, it is much more common but not without problems to rely on empirical parameters for quantitative

analysis by XPS.

### 4.3 Quantitative XPS Analysis

When a surface is exposed to X-rays there will be the following probability for emission of a photoelectron per incident photon

$$P_{xk} = \sigma_{xk} N_x t \quad (4.14)$$

where  $\sigma_{xk}$  is the cross section of level  $k$  in the element  $x$ ,  $N_x$  is the concentration (atoms/cm<sup>3</sup>) of element  $x$  in the surface, and  $t$  is the thickness of the probed area. The probability for exciting electrons in the sample is not the interesting number, what is interesting is the probability for those electrons to escape the surface without undergoing energy losses. If we assume that the surface is homogeneous ( $N_x(z) = N_x$  for  $t \gg \lambda_{xk}$ ) the probability for getting the electrons outside the sample, emitted from a depth of  $z$ , can be approximated by

$$dP_{xk}(z) = \sigma_{xk} N_x e^{-\frac{z}{\lambda_{xk}}} dz \quad (4.15)$$

which by integration over all depths leads to

$$P_{xk}' = \sigma_{xk} N_x \int_0^\infty e^{-\frac{z}{\lambda_{xk}}} dz \quad (4.16)$$

$$P_{xk}' = \sigma_{xk} N_x \lambda_{xk} \quad (4.17)$$

Here  $\lambda_{xk}$  is the inelastic mean free path for an electron emitted from level  $k$  travelling through material  $x$ . Thus the probability of emitting electrons beyond an infinitely thick sample will always be the same as if we were looking at a sample of thickness  $\lambda_{xk}$  without any damping. The X-ray will always penetrate deeply into the surface and excite atoms, but the rather small mean free path for the photoelectrons ensures the surface sensitivity as indicated in Figure 4.23.

The number of electrons detected from shell  $k$  of element  $x$  will, besides the above probability, be proportional to the number of photons  $F_{h\nu}$  and the transmission function for the analyser used  $T(E_{kx})$



$$I_{xk} = \sigma_{xk} N_x \lambda_{xk} F_{h\nu} T(E_{xk}) \quad (4.18)$$

This is the important formula for determining the composition of a surface which is homogeneous.

The intensity contribution from a layer in the depth  $z$  of thickness  $dz$  will be

$$dI_{xk} = dP_{xk} \lambda_{xk} F_{h\nu} T(E_{xk}) \quad (4.19)$$

$$= \sigma_{xk} N_x e^{-\frac{z}{\lambda_{xk}}} F_{h\nu} T(E_{xk}) dz \quad (4.20)$$

$$= \frac{I_{xk}}{\lambda_{xk}} e^{-\frac{z}{\lambda_{xk}}} dz \quad (4.21)$$

### 4.3.1 Example

Estimate the surface composition of an alloy made of NiSi assuming it to be homogeneous. The Intensity ratio  $I_{\text{Si}2p}/I_{\text{Ni}3p}$  is found to be 0.20. The cross section for the two lines can be found in Figure 4.22 to be  $1 \times 10^{-20} \text{ cm}^{-2}$  and  $2.5 \times 10^{-20} \text{ cm}^{-2}$  for Si and Ni respectively. Since the binding energy for the two lines is nearly the same (see Fig. 4.14) it is safe to assume that

$$\frac{I_{\text{Si}2p}}{I_{\text{Ni}3p}} = \frac{\sigma_{\text{Si}2p} N_{\text{Si}} \lambda_{\text{Si}2p} F_{h\nu} T(E_{\text{Si}2p})}{\sigma_{\text{Ni}3p} N_{\text{Ni}} \lambda_{\text{Ni}3p} F_{h\nu} T(E_{\text{Ni}3p})} \quad (4.22)$$

can be approximated by

$$\frac{I_{\text{Si}2p}}{I_{\text{Ni}3p}} = \frac{\sigma_{\text{Si}2p} N_{\text{Si}}}{\sigma_{\text{Ni}3p} N_{\text{Ni}}} \quad (4.23)$$

whereby the atomic composition can be estimated suggesting a  $\text{Ni}_2\text{Si}$  alloy.

The mean free path can alternatively be estimated from Figure 2.7 and the transmission function can be determined so this method can be used more generally. However, these different parameters are often put together in what is called a sensitivity factor  $S_{xk}$  which then is determined for a certain type of analyser. The intensity of a line can then be determined as the area of the

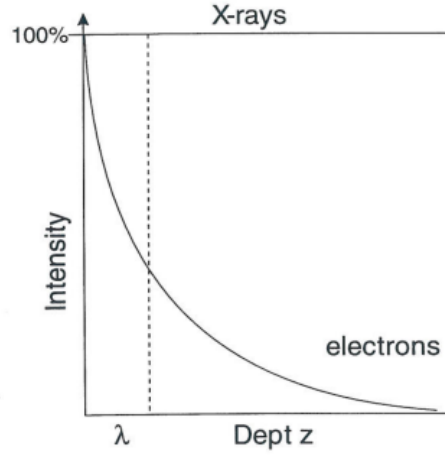


Figure 4.23: Sketch showing the difference in penetration depth of electrons and X-rays.

XPS line (or less accurate simply the peak height) and would then be given by

$$I_{xk} = S_{xk} N_x F_{h\nu} \quad (4.24)$$

and the atomic concentration of each element present in the sample can then be estimated as

$$C_x = \frac{\frac{I_{xk}}{S_x} \times 100\%}{\sum_{i=1}^N \frac{I_i}{S_i}} \quad (4.25)$$

where  $i$  refers to only one subshell in any of the  $N$  observed elements. Also in this case it is assumed that the surface is homogeneous. More elaborate estimations can be done without this assumption, but they will always be model dependent.

The surface sensitivity can be improved considerably if the surface of the sample is tilted relative to the analyser as shown in Figure 4.24.

In this manner the electrons emitted from the depth  $z$  will now have to pass through a layer of thickness  $z/\cos(\theta)$  where  $\theta$  is the angle between the surface normal and the analyser. If we consider a thin overlayer of material  $y$  of thickness  $d$  on top of layer  $x$  we will by integration of Eq. (4.21) get

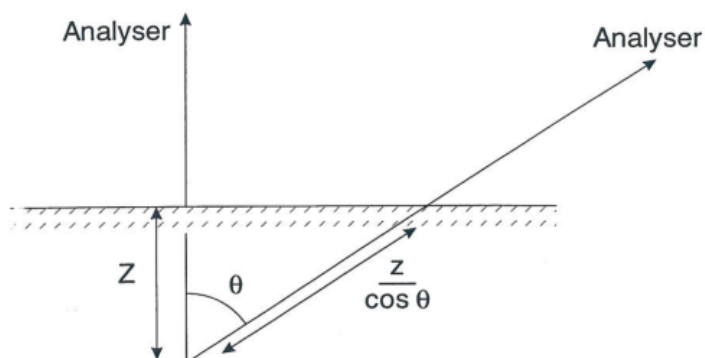


Figure 4.24: Sketch showing the effect of a take-off angle  $\theta$ .

$$I_{xk}(d) = I_{xk} e^{-\frac{d}{\cos(\theta)\lambda_{yk}}} \quad (4.26)$$

and

$$I_{ykt}(d) = I_{ykt} \left( 1 - e^{-\frac{d}{\cos(\theta)\lambda_{ykt}}} \right) \quad (4.27)$$

Thus by varying the angle it is possible to determine if the surface is inhomogeneous in the outermost layers or if it has another electron structure as we saw it in the ytterbium case. Naturally surfaces are not homogeneous, there are several reason why this is not the case. For example the spectra of the Cu(100) single crystal shown in Figures 4.7 and ?? clearly show traces of contaminations that will be confined to the surface. The oxygen and carbon are due to contamination since the crystal has been standing in the vacuum chamber for an extended period without cleaning. The presence of the sulphur, however, is due to segregation from the bulk of the crystal, which under the heat treatment necessary to anneal the crystal and re-establish the order after the cleaning procedure (argon sputtering) has diffused out at the surface. The amount of sulphur in the crystal amounts to the ppm level, but as the sulphur has a much lower surface energy than copper it is energetically favourable for the system to have the sulphur on the surface.

This is a quite general phenomenon and most alloys will therefore be enriched in one component at the surface compared to the bulk values.

The above formalism can be refined in several ways (see [6] and the references therein). We shall not deal further with these problems here, but just mention that one of the major problems when performing quantitative analysis by XPS is the subtraction of the background in the spectra. The intensity mentioned above is proportional to the area of the XPS line, thus the underlying background due to electrons that have undergone energy losses should be eliminated just as it was done in Figure 4.7. In general the energy loss function is not known well enough that such a procedure can be used, and even when it was we saw that there was still a discrepancy because of the intrinsic energy losses. Thus quantitative analysis with XPS will always have a rather large uncertainty and results better than 10 % should never be expected. The satellites will always be a source of errors and the assumption of a homogeneous sample is usually only fulfilled for pure elements. Nevertheless, XPS has proven extremely useful in many cases and no other method for determining the surface composition as accurately as XPS exists today.

## 4.4 Problems

1. What is the fundamental reason for the surface sensitivity of the electron spectroscopic methods?
2. Are there elements which cannot be detected by XPS? What about AES?
3. We want to determine the mean free path of electrons in iron by using the method described in the notes. Thus iron is deposited on a substrate of Ni and the damping of the Ni lines are measured. Two photoemission lines from Ni are used (excitation by  $\text{Al}_{K\alpha}$ ) which are observed at 65 eV and 700 eV binding energy, respectively. Due to the geometry of the experimental set-up only electrons in an angle of  $60^\circ$  from the surface normal will be detected. The intensity of the XPS signal before any deposition was measured to be  $I_{65\text{ eV}} = 10\,000$  counts/s and  $I_{700\text{ eV}} = 60\,000$  counts/s. Now  $8.6 \times 10^{-7} \text{ g/cm}^2$  of iron is deposited whereby the two lines are reduced to  $I_{65\text{ eV}} = 2300$  counts/s and  $I_{700\text{ eV}} = 6600$  counts/s. Under which assumption can we estimate the mean free path of the electrons in iron? Make the assumption and estimate the mean free paths.

Suggest/discuss a method to estimate when  $8.6 \times 10^{-7} \text{ g/cm}^2$  of iron has been deposited.

4. XPS is used to check whether a Ni(100) single crystal is clean enough to be used for surface reactivity experiments. The analyser measures along the surface normal. The acquired spectrum reveals a small carbon feature ( $\text{C}_{1s}$ ) which is measured relative to the  $\text{Ni}_{3p}$  line. The ratio is determined to be 0.018. We shall now interpret these data by use of two models.

In the first model we shall assume that all the carbon is located on top of the Ni surface with coverage  $\Theta$  less than one relative to the Ni atoms. The mean free path for the two lines will be assumed to be equal namely  $\lambda = 15 \text{ \AA}$ . Is that a good approximation? The cross sections for the two lines  $\text{C}_{1s}$  and  $\text{Ni}_{3p}$  can be read from Figure 4.22. Determine within this model the coverage  $\Theta$  of carbon. Will further cleaning of the surface be necessary or can we continue our investigations on the behaviour of clean Ni surfaces?

In the second model we assume that the carbon is distributed homogeneously into the Ni. Determine the carbon concentration and especially the carbon concentration at the surface.

Suggest an experiment that will allow us to determine which of the two models is best.

5. Explain the observed intensity distribution in the enclosed Figure 4.25 of clean samarium excited with different photon energies. Hint: The photoemission lines below 3 eV binding energy are due to divalent samarium, whereas the lines above 3 eV binding energy are due to trivalent samarium. Samarium is considered to be trivalent in the metallic state.
6. Figure 4.26 displays the uptake curves of carbon on a Ni single crystal when it is exposed to  $\text{CH}_4$  at different temperatures [21]. The saturation coverage is known to be 0.5 carbon atom per Ni atom. The carbon coverage as a function of dosage was determined with XPS. Determine from this set of data the sticking probability of methane on this surface in the zero coverage regime at various temperatures and estimate the activation energy for this process. Why are the curves not straight lines? If it took one hour to give the longest exposure, what is then the methane pressure over the crystal?

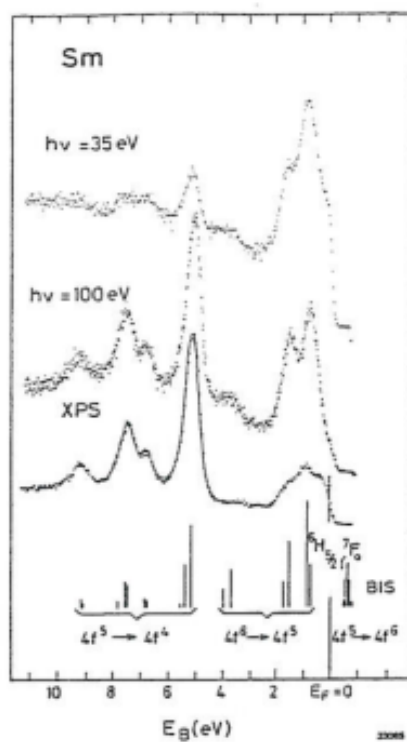


Figure 4.25: Synchrotron and XPS spectra of pure samarium [14].

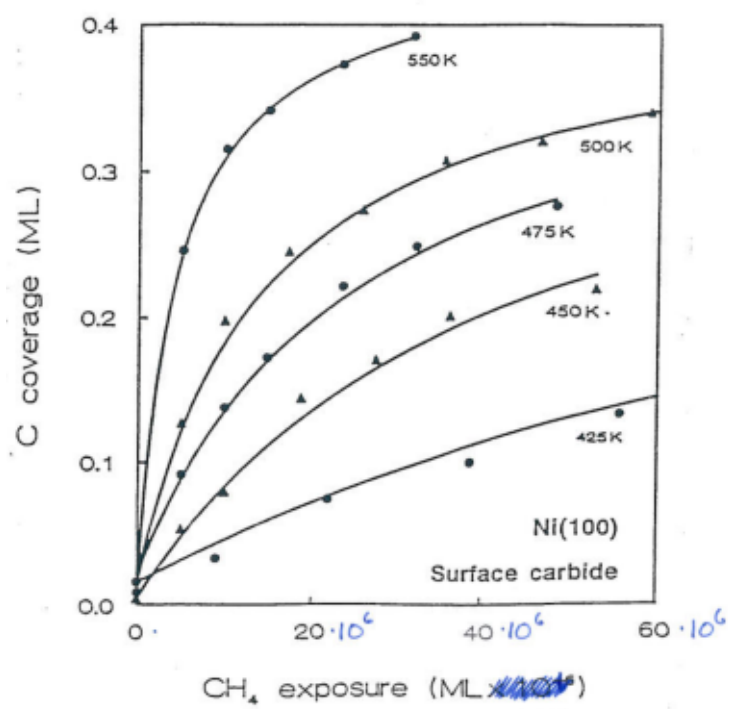


Figure 4.26: Carbon coverage on Ni(100) as a function of methane dosage at various temperatures [21].





# Chapter 5

## Ultraviolet or Synchrotron Photoelectron Spectroscopy

### 5.1 The Experimental Setup

Ultraviolet or Synchrotron Photoelectron Spectroscopy (UPS or SPS) are as the name indicate just a variation of the commonly used XPS using ultraviolet or synchrotron light as the excitation source. Nowadays the much more brilliant synchrotron sources are used since using these it is possible to tune the photon energy and often with much higher intensity. For a more detailed review of this method we shall refer to Plummer and Eberhart [22].

Originally an UV-lamp was used as the photon source. Here a discharge was made in a rare gas like Helium, but other rare gases may also be used. When the ionised atoms relaxes two characteristic emission lines occur: the singly ionised  $\text{He}^{\text{I}}$  and doubly ionised  $\text{He}^{\text{II}}$  with photon energies of  $h\nu = 21.2\text{ eV}$  and  $40.8\text{ eV}$ , respectively. The energy resolution of these lines is very high (on the order of  $\text{meV}$ ) due to the rather long lifetime of the ionized atoms. Since the intensity can be quite high the source can actually compete with many synchrotron sources. The disadvantage being that they are not tuneable like the synchrotron light is where the appropriate photon energy is selected by a monochromator. With the synchrotron it is possible to cover a broad spectrum of photon energies, from the infrared regime all the way up to hard x-rays, although different monochromators must be used. Thus it is always possible to select an energy so the photoelectrons have a maximum surface sensitivity. In the following we shall not worry about the photo

sources, but just consider how especially low energy photons are useful for studying the valence region.

The valence region is of particular interest because it is here we find the electrons participating in the chemical bonding. The energy of the photons should not be too high for two reasons: 1) We want the electrons to have energies at the minima of the mean free path. 2) The cross section for the photoionisation should not be too small. The methods are usually also combined with an analyser which can be moved in the chamber so it is possible to perform Angle Resolved Ultraviolet Photoelectron Spectroscopy (ARUPS). This method has been used widely and is usually a strong method, especially when combined with polarisation of the light, since it then can give detailed information on the

- electron structure of the valence band
- orbitals involved in chemical bonding
- geometry of adsorbed molecules

The principle of the experiment is shown schematically in Figure 5.1.

A typical UPS spectrum of a transition metal is shown in Figure 5.2. Here the d-band finger print can be found just below the Fermi level. It is also seen how the intensity increases towards low kinetic energy due to loss mechanisms. It is obvious that UPS cannot be used for identification of which elements that are present at the surface, since all metals (except for the rare earths) only exhibit broad and featureless structures in this region.

## 5.2 The Electronic Structure

### 5.2.1 The Band Structure

UPS and in particular ARUPS have been used to map out the band structure of solid materials. Here the outer electrons of the atoms react with each other forming a band structure with dispersion dependent on the momentum vector  $\vec{k}$ . Figure 5.3 shows the band structure for a simple free electron metal i.e.  $E(k) = (\hbar k)^2/(2m)$ . The photoemission process have to conserve both energy and momentum. Since the photon does not carry sufficient momentum to account for the momentum carried away by the photoelectron emitted the

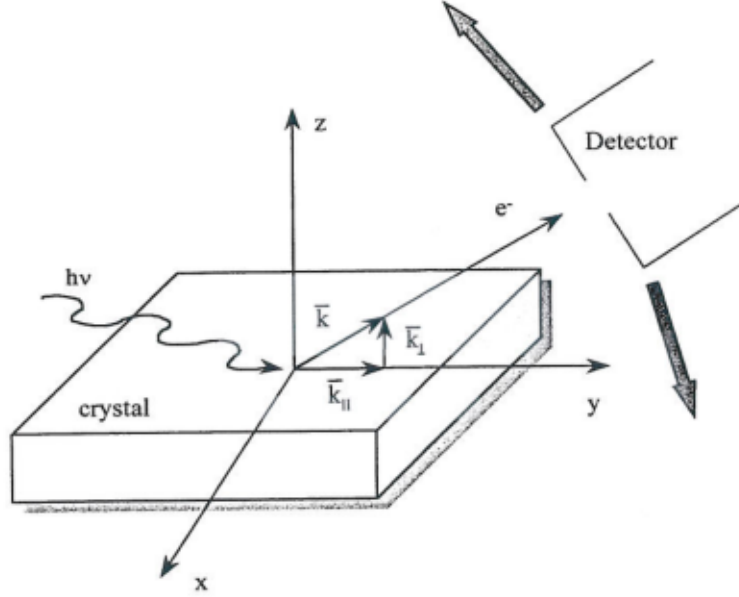


Figure 5.1: Schematics of the experimental set-up in an angle resolved UPS experiment.

crystal must take care of the recoil. This is illustrated in the reduced zone where the electron takes up a reciprocal lattice vector and the process can be depicted as a direct transition in the reduced zone.

By utilising the angle resolved method it is possible to map out the detailed band structure of a solid and in particular the structure at the surface region. An example is shown in Figure 5.4 where the ARUPS spectra of Cu(111) are shown as a function of angle into the analyser using  $h\nu = 11.6$  eV. The kinetic energy of the emitted photoelectrons is given by

$$E_{kin} = h\nu - E_B - e\Phi \quad (5.1)$$

where  $E_B$  is the binding energy of the electron relative to the Fermi level, and  $\Phi$  is the work function of the analyser.

$$E_{kin} = \frac{(\hbar k)^2}{2m} \quad (5.2)$$

leading to

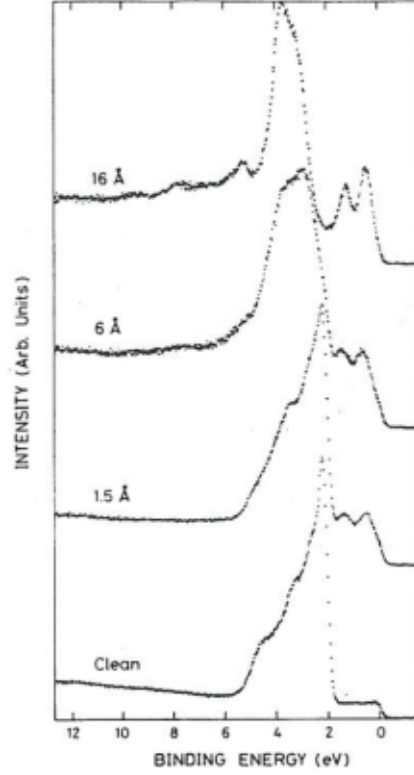


Figure 5.2: A UPS spectrum of clean Cu(100) with increasing amounts of samarium deposited. The photon energy was  $h\nu = 60$  eV. The sp-band of copper is observed just below the Fermi level, whereas the d-band is located at 2 eV to 4 eV binding energy. Taken from [23].

$$k_{\parallel} = \sqrt{\frac{2mE_{kin}}{\hbar}} \sin \theta \quad (5.3)$$

where  $k_{\parallel}$  is the component of the momentum parallel to the surface.

The momentum orthogonal to the surface  $k_{\perp}$  is not conserved due to the work done by leaving the potential barrier at the surface (the work function of the crystal). By determining binding energy and  $k_{\parallel}$  it is possible to map out the band structure around the  $\Gamma$  point for Cu(111) as illustrated in Figure 5.5. The shown example is rather atypical since the shown band is a surface

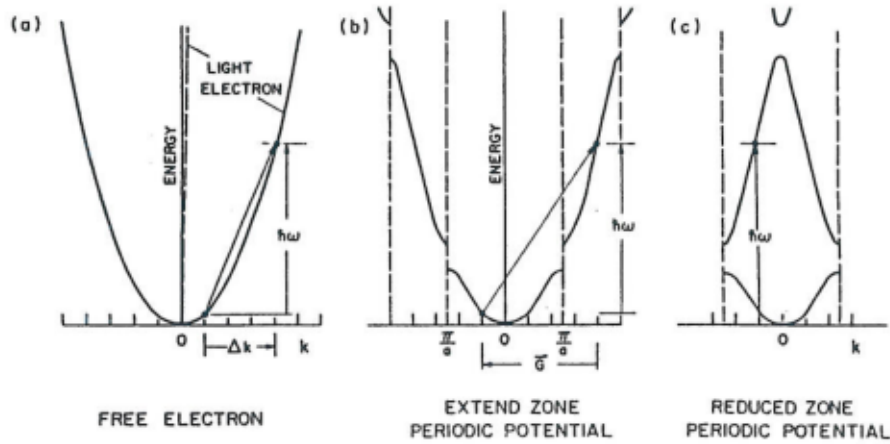


Figure 5.3: Sketch of the band structure of a free electron metal. Note the small momentum the photon carries compared to the electron. The transition can therefore only take place in the reduced zone where the lattice take up the recoil.

state lying in a bandgap. Usually there will be several bands overlapping and the gray zone indicated in Figure 5.5 illustrates such filled states in Cu(111), which in other directions will naturally cross the Fermi level since copper is known to be a metal. For a more detailed description of the band structure and how to measure it we shall refer to [24, 25].

Actually the experiment shown in Figure 5.5 is a very simple example. In reality the measurement of such photoelectrons is a three step process [26] where, firstly, the electron is excited from an initial band up into an empty band, secondly it have to be transported to the surface. In that process it may be diffracted as we shall see later and then finally be detected. Thus diffraction phenomena may also have to be taken into account considering the details of such experiments.

### 5.2.2 The Electronic Structure of Adsorbates

When a molecule like CO (the test molecule of surface science) approaches a surface the electronic states will in general be broadened and lowered due to the interaction with the metal electrons. Thus, although the states are quite

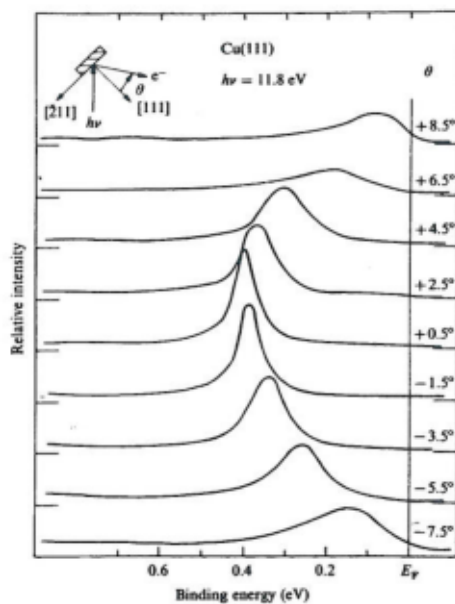


Figure 5.4: The ARUPS of Cu(111) as a function of the angle  $\theta$  from the surface normal.

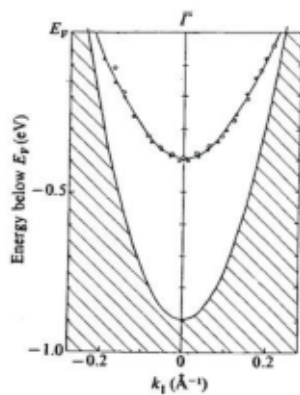


Figure 5.5: The band structure of the surface state in Cu(111) around the  $\Gamma$  point. The gray zone illustrates the occupied bulk states.

well defined in the gas phase they will now be rather broad as seen below in Figure 5.6. This figure shows the UPS spectra for gas phase CO and CO adsorbed on a number of transition metals like Ir, Ru, Pd, Pt, and Ni. The three highest occupied molecular levels of CO are easily identified in the gas phase spectrum, however, when CO chemisorbs the only feature which can be identified is due to the interaction with the valence electrons. The contribution from the d-band is in these late transition metals dominating the spectrum just below the Fermi level.

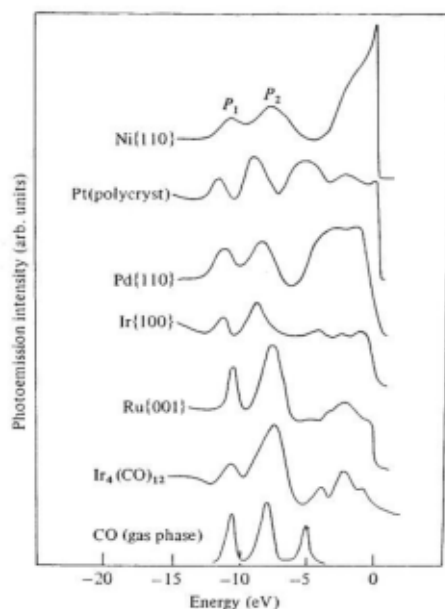


Figure 5.6: UPS of CO in the gas phase as well as CO adsorbed on a number of transition metals. Taken from Gustafson and Plummer [27].

Similar spectra can be observed for other adsorbates. Again it is seen that this cannot be used to identify adsorbates but solely to understand the bonding of already well defined systems. In this manner it was possible to understand the bonding geometry of for instance CO and also how molecules interact with each other as a function of coverage. Initially there was much dispute concerning the orientation of a chemisorbed molecule on a metal surface. Now it is well known that the molecule is bonded through the carbon in the "Blyholder model" and is standing orthogonal on the surface, at least



in the low coverage regime. In the following we shall briefly demonstrate how such information can be obtained by using ARUPS and polarized light. The probability for photoelectron emission in second order time-dependent perturbation theory is given by

$$P_{if} = | \langle \Psi_i | \mathbf{H}_{int} | \Psi_f \rangle |^2 \quad (5.4)$$

$\Psi_i$  and  $\Psi_f$  are the electronic wave functions for the initial and final states and  $\mathbf{H}_{int}$  is the interaction Hamiltonian given by

$$\mathbf{H}_{int} \propto \vec{A} \cdot \vec{P} \quad (5.5)$$

where  $\vec{A}$  is the vector potential set up by the photon and  $\vec{P}$  is the momentum operator

$$\vec{P} = \hbar \vec{\nabla} = \hbar \left( \frac{\partial}{\partial x}, \frac{\partial}{\partial y}, \frac{\partial}{\partial z} \right) \quad (5.6)$$

Now lets assume that the CO molecule is adsorbed on top of a Ni atom on a Ni(100) surface which contains a mirror plane. Then the matrix element  $\langle \Psi_i | \mathbf{H}_{int} | \Psi_f \rangle$  must be invariant to such a symmetry operation, i.e. the matrix element must be even to the operation or zero. The experiment is shown schematically in Figure 5.7

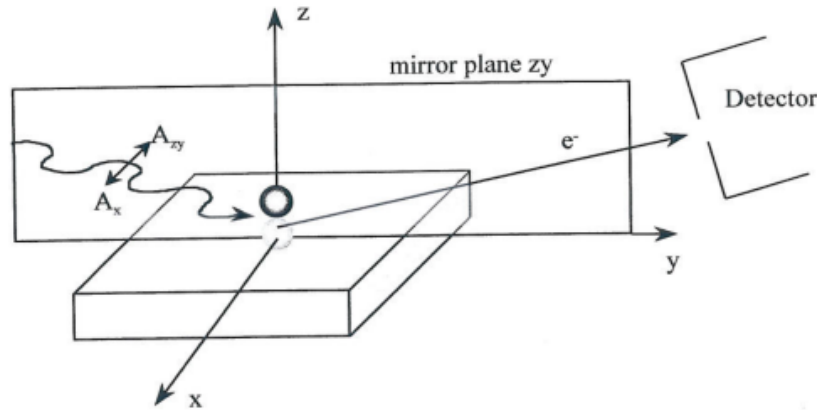


Figure 5.7: An ARUPS experiment using polarised light on a surface containing a mirror plane in the  $zy$ -plane.

Assume the mirror plane is lying in the  $zy$ -plane and the detector is located in this plane as well, then the final state  $\Psi_f$  must be even with respect to the symmetry operation or zero, i.e. no signal in the detector. We then have two possibilities for the incoming light. It can either be s-polarised i.e. the vector potential only has components parallel to the surface or p-polarised where it has components orthogonal to the surface. It is then easily seen that if we consider s-polarised light the product  $\vec{A} \cdot \vec{P}$  will give a product that will be odd with respect to the reflection in the  $zy$ -plane since  $\Psi_f$  should be even if anything should be detected. Thus  $\Psi_i$  must be odd in order for the matrix element to be even. Thus it is only possible to excite molecular orbitals that are odd with s-polarised light in the given configuration. This is clearly illustrated in Figure 5.8 where it is seen that for a certain configuration the even  $4\sigma$  is vanishing in the spectrum, while the odd  $1\pi$  still is observed.

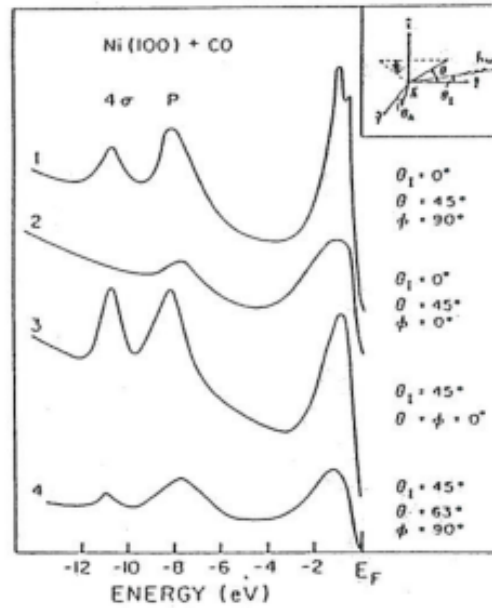


Figure 5.8: The result of an ARUPS experiment where the use of s-polarised light suppresses the signal from the even  $4\sigma$  while the odd  $1\pi$  can still be observed. For other combinations both orbitals are observed.

The symmetry of the various orbitals of CO are reproduced in Figure 5.9. By playing around with the geometry like this it is possible to describe the ge-

ometry of the chemisorbed CO molecule. It has been shown that the molecules tend to tilt when the coverage gets very high in order to accommodate the last CO molecules.

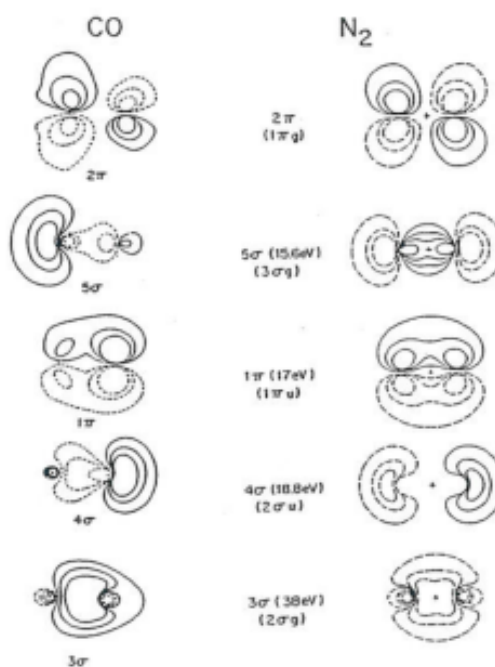


Figure 5.9: Sketches of the molecular orbital for CO and  $N_2$ . Notice that the  $\sigma$  orbitals are even with respect to the molecular axis while the  $\pi$  orbitals are odd.

The method has played a very big role in the infancy of surface science, e.g. to reveal the orientation and bonding geometry of molecules on the surface.

# Chapter 6

## The Auger Process

The Auger process was first explained by Pierre Auger in 1923 who was performing experiments with X-rays in a cloud chamber. He observed that besides the photoelectrons, which had an energy dependent on the energy of the X-rays, there were also emitted electrons with a constant energy and thus independent on which source had been used. These so-called radiationless transitions were due to the relaxation of the electron holes in the atom created by the photoemission process. We shall from here on refer to these processes as Auger transitions. The process is illustrated in Figure 6.1.

The *initial state* in this case consists of an atom where a hole has been created in a deep-lying core level. As we shall see, it is not interesting how this initial state was created. This atom is now highly excited and will eventually undergo a relaxation process. In Chapter 4 we saw that this relaxation can lead to emission of an X-ray photon, however, as long as the binding energy of the initial hole is well below 10 keV this process has a rather low probability of taking place. It is actually much more likely that a weakly bound electron will drop down and fill the initial hole and instead of emitting a photon use the energy to excite another electron out of the atom, leading to the *final state*. As shown in Figure 6.1 the final state consists of an atom with two holes either in some core levels, or in the valence levels or any combination thereof.

As for the photoemission process, the kinetic energy of the emitted electron will simply be the difference between the initial state and the final state. A crude estimate will thus be given by the Koopman binding energies as

$$E_{kin} = E_{initial} - E_{final} \approx E_{Binitial} - E_{Bfinal1} - E_{Bfinal2} \quad (6.1)$$

where  $E_x$  refers to the one electron binding energy of the holes involved.

Just as in the case of XPS it is clear that the energy distribution of the emitted electron will provide a unique identification of which elements and how much of each is present in our sample. If the appropriate energy interval is chosen it will also be surface sensitive. Thus we have a method which is very similar to XPS. However, there are a number of differences which sometimes makes AES more useful than XPS or vice versa.

**Figure 6.1** Schematics of an Auger process. Notice that both initial and final states have two holes.

## 6.1 The Excitation Source

The major difference between AES and XPS is the manner in which we get the atoms to emit electrons. We have earlier seen (see Figure 4.7) that there will always be emitted Auger electrons as a result of the relaxation of the holes created by the photoemission process. This is however a very inconvenient way of generating the necessary initial holes for the Auger process. It is much more useful to use a high energetic electron beam typically from 3 keV to 10 keV. As we saw under the discussion of the various energy loss mechanisms, energetic electrons will have a finite possibility of ionising the atoms in the substrate and hereby creating the necessary initial holes in a deep-lying core level (see Figure 2.10). The advantage of using an electron beam is that it can be focused and manipulated rather well and still have a high current density.

The electron beam is generated by use of an electron gun which is usually mounted inside the CMA as indicated in Figure 3.1. By passing current through a filament it will be heated sufficiently so that electrons can evaporate and be accelerated towards the sample. A number of lenses ensure that the beam diameter can be controlled and deflection plates at the end of the gun ensures that the beam can be manipulated to any desired position on the surface or scan over an area (see Figure 6.2).

**Figure 6.2** Schematics of an electron gun for AES.

As the lens system in the electron gun is an electrostatic imaging of the electron source onto the sample it is advantageous to use a LaB<sub>6</sub> source. By mounting a LaB<sub>6</sub> crystal on a filament a very good point source can be obtained and a spot diameter down to 200 Å can be achieved with a current of 0.1 nA. Actually even higher resolutions can be obtained as in the electron microscopes, but here we must remember that a sufficiently high current density is required if we want to obtain Auger spectra with a reasonable signal to noise ratio. As this demands no less than 0.1 nA and as it is not possible to confine electrons to spots smaller than 200 Å at such high current densities (unless going to much higher energies which then causes other problems) this in reality sets the limit for lateral resolution in AES.

## 6.2 The Fine Structure in AES

As mentioned the kinetic energy of the Auger electrons is given by the difference between the initial and final state. Thus Eq. (6.1) is only very crude as we know that the atom will undergo relaxations when the initial hole is being created. A better approximation is therefore to take the binding energy of the two final holes to be an average of the binding energy for the atom considered  $Z$  and the binding energy it would have in an atom with  $Z + 1$ . The kinetic energy could then be approximated by

$$E_{kin} \approx E_{B_{initial}}^Z - \frac{E_{B_{final1}}^{Z+1} + E_{B_{final1}}^Z + E_{B_{final2}}^{Z+1} + E_{B_{final2}}^Z}{2} \quad (6.2)$$

where  $E_x^Z$  refers to the one electron binding energy of the hole  $x$  in atom  $Z$ . In Figure 6.3 the kinetic energy for the strongest Auger lines is given for most of the elements. It is obvious that it is nearly always possible to find an Auger line with an energy in the interval where the electrons will be surface sensitive.

### 6.2.1 Nomenclature

An Auger transition is always named XYZ describing which energy levels are participating in the transition. The X refers to the initial hole, whereas the

Y and Z refers to the two holes in the final state. In order to make this more complicated than necessary the old X-ray notation is used for these levels. Here the various levels have the following names:

1s	K
2s, $2p_{\frac{1}{2}}$ , $2p_{\frac{3}{2}}$	$L_1$ , $L_2$ , $L_3$
3s, $3p_{\frac{1}{2}}$ , $3p_{\frac{3}{2}}$ , $3d_{\frac{3}{2}}$ , $3d_{\frac{5}{2}}$	$M_1$ , $M_2$ , $M_3$ , $M_4$ , $M_5$
4s, $4p_{\frac{1}{2}}$ , $4p_{\frac{3}{2}}$ , $4d_{\frac{3}{2}}$ , $4d_{\frac{5}{2}}$ , $4f_{\frac{5}{2}}$ , $4f_{\frac{7}{2}}$	$N_1$ , $N_2$ , $N_3$ , $N_4$ , $N_5$ , $N_6$ , $N_7$



**Figure 6.3** Energies of the strongest Auger transitions.

### 6.2.2 Multiplet Splitting in AES

If we consider a transition starting with a hole in the 1s shell which results in two holes in the 2s or 2p shell then the name of the transition would be KLL which is the dominant type of lines for the lighter elements. This type of transition can naturally be divided up into different combinations like:  $KL_1L_1$ ,  $KL_1L_2$ ,  $KL_1L_3$ ,  $KL_2L_3$ ,  $KL_2L_2$ ,  $KL_3L_3$  leading to six lines.

In Figure 6.4 this type of transition is shown for magnesium and it is easily seen that the spectrum cannot be explained by only four lines. The reason that we only got six lines is that we used a notation only appropriate in jj-coupling. We saw earlier that when more than one localised hole is present it is more appropriate to use intermediate coupling starting either from jj-coupling or LS-coupling.

**Figure 6.4** A KLL Auger spectrum of Magnesium

Thus in the intermediate coupling scheme the above transitions would lead to the following final states:

$$\begin{array}{ll}
 \text{KL}_1\text{L}_1 & {}^1S_0 \\
 \text{KL}_1\text{L}_2, \text{KL}_1\text{L}_3 & {}^1P_1, {}^3P_0, {}^3P_1, {}^3P_2 \\
 \text{KL}_2\text{L}_3, \text{KL}_2\text{L}_2, \text{KL}_3\text{L}_3 & {}^1S_0, {}^3P_0, {}^3P_1, {}^3P_2, {}^1D_2
 \end{array}$$

Thus the simplest transition we can think of consists of a substantial number of lines. If the initial state is not an s-electron there will also be a splitting

of the initial state due to a spin orbit splitting doubling the number of Auger lines. An example of this type of transition is shown in Figure 6.5 where the  $M_{45}N_{67}N_{67}$  for ytterbium and gold are shown. The spin-orbit splitting of the  $N_{45}$  level is very large in both cases leading to two well-separated multiples. A theoretical description of the line shape (using the intermediate coupling scheme) is possible for the gold, but not for the ytterbium where other types of Auger transitions obscure the comparison. Due to an  $M_4M_5N_{67}$  there will be a transition starting with a hole both in the  $M_5$  and the  $N_{67}$  level leading to a multiplet structure right on top of the  $M_5N_{67}N_{67}$  lines. The spectra shown in Figure 6.5 was actually induced by the continuous bremsstrahlung emitted from an aluminium anode.

**Figure 6.5** The experimental Auger spectra of Yb and Au and the theoretical fits.

So far we have not discussed the transition probability for the Auger transition. As the relaxation process is due to the Coulomb interaction between the involved electrons, the interaction Hamiltonian will be described by a Coulomb interaction and the transition probability will be given again

by Fermi's golden rule. In the frozen core approximation and one-electron picture this results in [28]:

$$P_{Auger} = \frac{4\pi^2}{h} \left| \left\langle \Phi_{Initial} \left| \frac{e^2}{r_{12}} \right| \Phi_{Final} \right\rangle \right|^2 \quad (6.3)$$

where initial and final states refers to the two vacancies in the initial and final state. This expression has been used to calculate the probability for going from each possible initial state to any available final state as shown in Figure 6.5. In general the multiplet splitting of Auger transitions is quite complex leading to rather broad features as we have already seen. The life-time broadening will contribute significantly as there are three holes involved in the process now. Furthermore, just as was the case for the photoemission process, the Auger process will be followed by various shake-up and shake-off processes leading to satellite structures. They are therefore not as useful for chemical identification and investigations of electron structures as the XPS lines. But if we disregard the details of the structure and simply use the Auger lines as a finger print of the various elements they can be very useful.

### 6.3 AES for Qualitative Analysis

When creating a deep lying hole there are two competing possibilities for relaxation of the excited atom. One is the emission of a photon with the probability  $\omega_X$ , which was very useful for generation of X-rays for XPS, and the other is a decay through emission of an Auger electron with the probability  $\omega_{Auger}$ . The two channels are competing, but in general  $\omega_{Auger}$  will be much larger than  $\omega_X$  for initial holes with binding energy less than 10 keV. For example Figure 5.6 shows the probability of the two types of relaxation plotted for a hole in the 1s shell as a function of the atomic number. The binding energy of the 1s level in element  $Z = 33$  (As) is 11.8 keV. Thus for electron beams with energy less than 10 keV the Auger process will prevail.

**Figure 6.6**  $\omega_X$  and  $\omega_A$   
as a function of  $Z$   
for the 1s shell.

The emission of the X-rays actually has a very useful aspect since they also carry information on which elements are present in the sample. This method is known by the name EDX and is mainly performed in combination with electron microscopy. It is complementary to the methods discussed here as it is not surface sensitive (usually probing  $\sim 1\text{ }\mu\text{m}$ ) on the atomic scale. Besides it is not a very useful method for detection of the light elements ( $Z < 11$ ) as most of the relaxation in this low binding energy regime takes place through Auger transitions.

An Auger spectrum of silver excited by the use of 2 keV electrons is shown in Figure 6.7. The  $N(E)$  spectrum is completely dominated by the elastically scattered electrons and primary electrons which have undergone energy losses in the solid.

**Figure 6.7** The raw  $N(E)$  spectra of Silver excited by 2 keV electrons.

Weak structures can be observed just below the elastic peak (energy loss features of silver) and around 350 eV. This region has also been shown as  $N(E) \times 10$  and it is now easily seen that there is a structure here. By consulting Figure 6.3 these lines can be identified as the silver  $M_{45}N_{45}N_{45}$

transition. The lines are lying on top of the high continuous background of secondary electrons which basically carries no information and it is therefore convenient to differentiate the spectrum as shown in the top panel. The nearly constant background is then eliminated and the structure of the line is easily recognised. The intensity of the lines, assuming a Gaussian line shape, can then be approximated by the peak to peak height. Just as for XPS all the Auger spectra of the elements have been collected in a handbook [29] and Figures 6.8 and 6.9 show a few examples of such standard Auger spectra.

**Figure 6.8** The standard Auger spectrum of Aluminium.

Figure 6.8 shows the Auger spectrum of a relatively clean aluminium surface. Apart from several low level contamination features of Ar, C and O, two main features from aluminium are observed. The low lying line at 68 eV is due to an  $L_{23}VV$  transition. The VV refers to the fact that the two final states are located in the valence band and the shape of the Auger line in this case will actually be a self-convolution of the valence band. The high energetic line at 1396 eV is due to a  $KL_{23}L_{23}$  transition which is much weaker. The features below 1390 eV can be accounted for by energy losses due to plasmons. If this surface is oxidised to  $Al_2O_3$  the spectrum undergoes rather strong changes as shown in Figure 6.9. Both transitions shift downwards in energy by 17 eV to 18 eV and the energy loss features change dramatically. This is a result of chemical shifts and changes in the relaxation mechanisms. The aluminium has by oxidation been changed from a very good conductor to an isolator. Thus the valence electrons have been shifted down in energy



and there are no delocalised electrons around to effectively screen the excited final state. Therefore, the characteristic plasmon energy losses are no longer observed. In this case it is possible to identify the chemical state of the aluminium, especially when the presence of oxygen at 510 eV is taken into account.

**Figure 6.9** The standard Auger spectrum of  $\text{Al}_2\text{O}_3$ .

Similar chemical identification can be done for carbon as seen in Figure 6.10 where the carbon Auger feature is depicted for a number of carbon containing compounds. It is in general possible to differentiate between carbon in covalent bonding and ionic bonding. The carbides display a spectrum characteristic of a filled shell structure like neon. The same features are observed for nitrogen in nitrides and naturally for oxygen and fluorine. Figure 6.11 shows an AES study of the decomposition of methylamine on nickel. At very low temperatures the methylamine is chemisorbed associatively on the surface and the spectrum reflects the line shape expected from molecules to a high degree. As the surface is heated the molecule will decompose and finally all the hydrogen will desorb and the nitrogen and carbon will react with the surface forming carbides and nitrides which can easily be identified by their characteristic line shapes [30].

Thus chemical identification can sometimes be undertaken with AES, but certainly not as efficiently as with XPS. Besides there are other problems with

AES which should be mentioned when discussing chemical identification. Since a high energetic electron beam is used with a relatively high current density, there is always a potential danger that the excitation source itself introduces chemistry. This is not a severe problem for metals and alloys, but it is serious for chemical compounds like polymers or the methylamine shown above.

**Figure 6.10** The auger line shape of the KLL transition in various chemical surroundings.

**Figure 6.11** The Auger spectrum of methylamine adsorbed on Ni(111) during decomposition.

If the AES spectrum of the chemisorbed methylamine shown in the bottom of Figure 6.10 was to be repeated after the surface had been exposed to the electron beam for 5 minutes the spectrum would look exactly as if it had reacted all the way to nickel-nitride and -carbide. Thus great care has to be taken when AES is used on compounds.

## 6.4 AES for Quantitative Analysis

Carrying out quantitative analysis with AES is very similar to XPS, although there are a few complicating factors. The probability for getting an Auger electron  $XYZ$  out from a thin layer of element  $x$  in the depth  $z$  will be given by

$$dI_x^{XYZ}(z) = N_x \sigma_X(z) \omega_{XYZ} e^{-\frac{z}{\lambda_{XYZ}}} i(z) T(E_{XYZ}) dz \quad (6.4)$$

where  $N_x$  is the number of atoms/cm<sup>3</sup>,  $\sigma_X(z)$  is the cross section for generating the initial hole  $X$  at depth  $z$ ,  $\omega_{XYZ}$  is the probability that the initial hole will decay as an Auger process,  $\lambda_{XYZ}$  is the inelastic mean free path of the Auger electron,  $T(E_{XYZ})$  is the probability that the electron will be detected by the analyser,  $i(z)$  is the flux of primary electrons at depth  $z$ . The electron flux of primary electrons vary with the depth because these electrons will undergo energy losses and because they will scatter elastically in the solid.

If we consider a pure element and assume that the dependency on depth is weak all these various factors can be put together in one constant namely

$$I_x^{\infty XYZ} = N_x \sigma_X \omega_{XYZ} i_0 T(E_{XYZ}) \lambda_{XYZ} \quad (6.5)$$

which is the signal we will obtain from the clean sample. Equation (6.4) would then read

$$dI_x^{XYZ}(z) = \frac{I_x^{\infty XYZ}}{\lambda_{XYZ}} e^{-\frac{z}{\lambda_{XYZ}}} dz \quad (6.6)$$

By integration from zero depth to infinity we get

$$I_x^{\infty XYZ} = \int dI_x^{XYZ}(z) = \int_0^{\infty} \frac{I_x^{\infty XYZ}}{\lambda_{XYZ}} e^{-\frac{z}{\lambda_{XYZ}}} dz \quad (6.7)$$

By measuring the signal from the pure elements it is possible to establish a set of sensitivity factors just as it was done for the XPS lines.

$$I_x^{XYZ} = S_x^{XYZ} N_x \quad (6.8)$$

whereby the composition of a sample can be estimated as

$$C_x = \frac{I_x^{XYZ}}{S_x^{XYZ} \sum_i^N \frac{I_i^{XYZ}}{S_i^{XYZ}}} \times 100\% \quad (6.9)$$

where the sum  $i$  goes over all  $N$  elements present in the sample.

The relative sensitivity factors for most of the strongest Auger lines are shown in Figure 6.12 for a primary electron beam of 3 keV and in Figure 6.13 for a primary beam of 10 keV. Both figures are taken from [29].

**Figure 6.12** The sensitivity factors for Auger transitions excited by 3 keV

electrons.

Several approximations were necessary to achieve this simple expression and the compositions determined in this manner will therefore also have a considerable uncertainty. Thus for investigations where accurate determination of the surface composition is mandatory XPS should be used. However, the AES method is very useful especially for determining relative compositions between different areas of the samples or depth analysis.

**Figure 6.13** The sensitivity factors for Auger transitions excited by 10 keV electrons.

### 6.4.1 Example

In this example we shall demonstrate how the attenuation of the Auger signals can be used to study growth mechanisms on surfaces and how it can be used to determine the inelastic mean free path. Figure 6.14 shows the natural logarithm of the Auger signal for two germanium lines relative to the pure germanium as a function of silicon coverage deposited on top of the germanium. It is seen that the germanium signal is damped exponentially. If we assume that the analyser was positioned normal to the surface we can estimate  $\lambda$  for the two different kinetics energies if the coverage of the silicon



is known and if we assume that it is deposited layer by layer. The germanium intensity will be given by

$$I_{\text{Ge}}^{XYZ}(d_{\text{Si}}) = I_{\text{Ge}}^{\infty XYZ} e^{-\frac{d_{\text{Si}}}{\lambda_{\text{Si}}}} \quad (6.10)$$

where  $d_{\text{Si}}$  is the thickness of the overlayer. The germanium signal will be damped through the silicon and it is therefore  $\lambda_{\text{Si}}$  which is determined in this manner.

**Figure 6.14** Attenuation of the Ge LMM (1147 eV) and Ge MVV (52eV) Auger lines as a function of Si Coverage.

By plotting  $\ln(I_{\text{Ge}}^{XYZ}(d_{\text{Si}})/I_{\text{Ge}}^{\infty XYZ})$  vs.  $d_{\text{Si}}$ ,  $\lambda_{\text{Si}}$  can be found for the two energies.

Similarly the signal of the silicon Auger lines can be followed and the intensity of the silicon Auger lines would have the following form as a function of thickness

$$I_{\text{Si}}^{XYZ}(d_{\text{Si}}) = \int_0^{d_{\text{Si}}} \frac{I_{\text{Si}}^{\infty XYZ}}{\lambda_{\text{Si}}} e^{-\frac{z}{\lambda_{\text{Si}}}} dz = I_{\text{Si}}^{\infty XYZ} (1 - e^{-\frac{d_{\text{Si}}}{\lambda_{\text{Si}}}}) \quad (6.11)$$

The above results can easily be made more surface sensitive by changing the detection angle to be  $\theta$  degrees off the normal.  $\lambda$  would then in the above formulas change to  $\lambda \cos \theta$  as we saw in Equation (4.26).

### 6.4.2 Growth Mechanisms

The ability to grow new structures on a substrate is a very important field in material science today. In the above example we assumed that the growth of the silicon was a layer by layer process. Thus one layer of Si is completed before the next layer is started and it is possible to grow perfect macroscopic crystal structures in this manner. If we look carefully at the germanium signal as a function of the silicon coverage, we shall see that the signal actually consists of a number of straight lines which form an exponential decay. The ratio of the germanium signal for a coverage of  $\theta_{\text{Si}}$  less than one monolayer will be given by

$$\frac{I_{\text{Ge}}(\theta_{\text{Si}})}{I_{\text{Ge}}^{\infty}} = (1 - \theta_{\text{Si}}) + \theta_{\text{Si}} e^{-\frac{l_{\text{Si}}}{\lambda_{\text{Si}}}} \quad 0 \leq \theta_{\text{Si}} \leq 1 \quad (6.12)$$

where  $l_{\text{Si}}$  is the thickness of one monolayer of silicon.

The above equation can easily be generalised to the transition from the  $n^{\text{th}}$  layer to the  $(n+1)^{\text{th}}$  layer

$$\frac{I_{\text{Ge}}(\theta_{\text{Si}})}{I_{\text{Ge}}^{\infty}} = (1 - \theta_{\text{Si}}) e^{-\frac{nl_{\text{Si}}}{\lambda_{\text{Si}}}} + \theta_{\text{Si}} e^{-\frac{(n+1)l_{\text{Si}}}{\lambda_{\text{Si}}}} \quad 0 \leq \theta_{\text{Si}} \leq 1 \quad (6.13)$$

where  $\theta_{\text{Si}}$  is the amount of the  $n^{\text{th}}$  layer covered with silicon.

The result of such an attenuation of the germanium signal is shown in Figure 6.15.

**Figure 6.15** The attenuation of the substrate signal as a function of coverage. The different curves represents different growth mechanisms.

Unfortunately the growth mechanisms are in general not as simple as we have just seen. They are dictated by surface diffusion, deposition rates, substrate temperature and surface and interface energies of the elements involved. It is beyond the scope of this review to go further into the various mechanisms, but we shall mention that there are other categories of growth.

- The layer by layer growth is called a **Frank-van der Merwe growth**.
- Another possibility is that the first layer is completed before the second layer is started, but then the layer by layer growth stops and islands are formed. This is called a **Stranski-Krastanov growth** mode.
- Finally there is the possibility that islands are formed right from the beginning and that is referred to as a **Volmer-Weber growth** mode.

It is only in the first case it is possible to describe the process easily. In the other modes the unknown distribution of islands and their sizes makes an analysis very difficult. The effects of the various mechanisms are illustrated in Figure 6.15.

Recent experiments using Scanning Tunnelling Microscopy, where it is possible to investigate the individual atoms deposited on the surface, have shown that alloying also complicates the above picture.

## 6.5 Scanning Auger Microscopy SAM

The biggest advantage of AES might be the ability to focus the primary electron beam on a small spot as we discussed in Section 6.1. Thus very small areas can be analysed. If this is combined with the possibility to scan the electron beam over the surface it is possible to obtain a lateral resolution of the surface composition.

Figure 6.16 shows an Auger spectrum of a copper grid placed on top of a silver foil. The distance between each mask of the grid is  $25\text{ }\mu\text{m}$  and the Auger spectrum was obtained while the electron beam was scanned over an area of  $65 \times 100\text{ }\mu\text{m}^2$  with TV scan rate.

If the amount of secondary electrons emitted from the surface is measured as a function of the beam position it is possible to construct an image of the surface. This is usually referred to as a secondary electron micrograph which can give topologic information of the surface. The top panel of Figure 6.17 shows such a SEM picture of the copper grid.

If the analyser is now set to measure the intensity in a narrow window around, for example, the silver line at 355 eV it is possible to measure the amount of silver in the surface as a function of the electron beam position. This is exactly what has been done in the rest of the panels in Figure 6.17 for a number of the elements seen in Figure 6.16. It is easily seen that the grid consists of copper and that it is placed on top of a silver foil. Furthermore it is observed that the contamination by sulphur is primarily located on the silver, whereas the chlorine is mainly adsorbed on the copper grid. The resolution in this picture is around 1  $\mu\text{m}$ .

**Figure 6.16** The Auger spectrum of a Copper grid mounted on a Silver foil and averaged over an area of  $65 \times 100 \mu\text{m}$ .

The methods can be refined by measuring not only the intensity of the Auger line, but also the intensity of the background before and after the peak. In this manner the (Signal-Background)/Background can be used for the imaging and hereby topologic effects will be reduced.

SAM is a rather time consuming process dependent on the resolution required and the size of the area investigated. In general at least 10 ms is required for each point measured (dependent on the primary current and thus dependent on the resolution of the electron beam) and if a high resolution is needed  $512 \times 512$  points may be required. Such a picture will then take 2500 seconds and three times as long if the background needs to

be eliminated.

The method is very useful in many contexts, especially in applied material science.

**Figure 6.17** a) The SAM picture of a Copper grid mounted on a Silver foil.

The first picture is a Secondary Electron Micrograph picture showing the grid. Then follows the SAM pictures of b) Cu, c) Ag, d) S, and e) Cl.



## 6.6 Problems

1. Estimate from Figure 6.14 the mean free path for electrons with energies of 52 eV and 1147 eV, respectively, through Si.

How does this fit into the universal curve shown in Figure 2.6?

Discuss how the signals in Figure 6.14 would behave if we did not have Frank-van der Merwe growth.

2. Determine how the signal of Si will behave as a function of dosage when it is evaporated onto Ge as in Figure 6.14. (Hint: Plot  $\ln(1 - \frac{I(d)}{I_0\lambda})$  vs.  $d$ , where  $d$  is the thickness of the overlayer.)
3. In order to get a reasonable signal to noise ratio it is necessary to have an electron beam current of at least 2 nA when doing AES or SAM. Estimate the fluency when the beam (10 keV) is focused on a diameter of 1  $\mu\text{m}$  and 200  $\text{\AA}$  respectively. 200  $\text{\AA}$  is the ultimate resolution that can be achieved with SAM in dedicated equipment. In the following we shall assume that the cross section for dissociation of an adsorbed molecule by the above electrons is  $\sim 1 \times 10^{-20} \text{ m}^{-2}$  and that we are measuring on a monolayer of molecules with an area of  $5 \times 10^{14} \text{ cm}^{-2}$ . How long time can we allow ourselves to measure at the same spot if we only allow 10 % of the molecules to dissociate.
4. Figure 6.18 shows an AES spectrum of a fractured interface between an inconel 600 plate on which a ceramic containing  $\text{Al}_2\text{O}_3$  and  $\text{MgO}$  was adhered. Estimate the surface composition of the fracture if it is assumed that the surface region is homogeneous. The relevant surface sensitivity factors are given for peak to peak measurements. (Inconel 600 is an alloy containing roughly 76 % Ni, 17 % Cr and 7 % Fe).

**Figure 6.18**



## Chapter 7

# Depth Profiling with XPS and AES

In the previous chapters we have discussed the XPS and AES methods for surface analysis. Both methods are very useful for determination of the qualitative composition, although XPS clearly is the most advantageous for identifications of chemical composition and when an accurate quantitative determination is called for. On the other hand, AES is advantageous if information of the lateral composition is necessary. Both methods can also be used for a determination deeper into the material. We have already seen that some depth information can be obtained by tilting the sample relative to the analyser. This, however, only gives a depth resolution of a few atomic layers. Therefore, the methods must be combined with other methods so that the interesting layer can be exposed to the surface sensitive analysis. This can be done mechanically by a broad variety of polishing procedures or by sputtering.

### 7.1 Instrumentation

The first class of methods is the mechanical type where the interesting part of the sample can be exposed simply by making a cut orthogonal to the surface or by ball cratering. In the first case the deep lying layers can then be analysed by use of SAM (see Figure 7.1). It is immediately seen that the resolution of this analysis will be limited by the resolution of the SAM available. This may not be trivial as it is not always easy to prepare a sample

with a perfect cut orthogonal to the surface, especially not in the cases where the region is very inhomogeneous. The ball cratering method, as shown in Figure 7.2, is very similar except that a crater is polished in the surface. Different layers will then be exposed and can again be analysed by use of SAM with sufficient resolution.

In both cases the depth resolution is given by SAM (200 Å and upwards), although it can be improved considerably in the ball cratering method due to the fact that we here have a cut under an angle. These methods are seldom used because in general it is much more convenient to use EDX on such samples.

**Figure 7.1** Schematics of SAM analysis of an orthogonal cut.

**Figure 7.2** Schematics of the ball cratering method.

However, in the range 0 Å to 1000 Å there is another method by which the surface can easily be exposed and analysed by use of both AES or XPS, namely by sputtering with rare gas atoms, preferentially argon. By ionising Argon at a high potential the ions created can be manipulated just like the electrons and be focused into a spot on the surface and scanned if necessary. The formation of the beam is very similar to the way we measured the pressure in the chamber as shown in Figure 2.4. Instead of collecting the ions on the collector they are extracted from the cage formed by the grid and accelerated towards the sample which is usually kept grounded. In this manner ion beams with energies of 1 keV to 5 keV and with currents of 0 µA to 10 µA can be formed. The argon is supplied by leaking in argon in the chamber to the required pressure of roughly  $1 \times 10^{-5}$  mbar. This is a high pressure in the context of UHV and might also cause problems for some types of pumps, like for instance the ion pumps, but as the gas is inert it does not influence the surface analysis if the argon is sufficiently clean. The pressure in the chamber can be reduced about three orders of magnitude if a differentially pumped ion gun is used instead. In this case a high pressure is still needed in the ionising region but the beam is then passing through a small hole into the main chamber. By pumping the ion-gun and the main chamber by separate pumps (differentially pumped) the pressure in the main chamber may be kept in the  $10^{-8}$  mbar region. The spot size diameter is, as for the electron beam, determined by the current density and will typically be on the order of 100 µm in standard equipment. The beam can be scanned to give a homogeneous exposure over a rather large area (10 mm × 10 mm) of the surface so depth analysis with XPS can be carried out. For other applications, like for instance Secondary Ion Mass Spectroscopy (SIMS), the beam can be focused down to much smaller spots sizes.

## 7.2 Ion Sputtering

Several types of rare gases can be used for sputter profiling, but usually argon is the preferred gas as it is cheap to purify and has a high sputter yield. When a high energetic ion is hitting the surface the ion will be neutralised and transfer energy to the surface atoms through a number of essentially binary collisions. Some of the surface atoms will obtain sufficient energy and momentum to be able to escape the surface (see Figure 7.3). The atoms which in this manner are scattered off the surface will mostly leave as neutral

species and only a small fraction will survive as ions. Since the ions are essentially coming from the top most layer and since they are easily detected by a mass spectrometer this is a method very useful for determining the depth composition into the surface as the atoms are sputtered away. This method is called SIMS as mentioned above and can be carried out in small spots. The method is extremely sensitive (ppm level) but is rather difficult to quantify since the survival of the ions depend exponentially on the work function of the surface. For further details on this method we shall refer the reader to [31]. A method has been developed which overcomes this problem by detecting all the atoms coming off the surface. This is a much more reliable way to determine the surface depth composition. However, since this method relies on resonance ionisation by two lasers it is not economically viable.

Therefore, it is much more convenient to simply use either XPS, or preferentially AES, to measure what is left on the surface after a certain number of atoms have been sputtered away by bombarding the surface with energetic  $\text{Ar}^+$  ions. The measurements can be made simultaneously with sputtering or by alternating between sputtering and measuring. The AES method is the preferred method because it is in general much faster than the XPS method.

**Figure 7.3** Schematics of the sputtering process.

If we define a sputter yield  $Y$  as the number of atoms removed from the surface per incoming ion it is possible, under ideal conditions, to convert time sputtered to a depth.

The flux of ions  $F$  can be written as

$$F = \frac{I}{eA} \quad (7.1)$$

where  $I$  is the ion current and  $A$  is the area exposed to the ion beam. In a pure element the number of atoms removed per second per area will be given by

$$g_i = FY_i \quad (7.2)$$

$g_i$  can be converted to a depth by

$$\frac{dz_i}{dt} = \dot{z}_i = \frac{g_i}{N_i(z)} = \frac{FY_i(z)M_i}{\rho_i(z)N_A} = \frac{IY_i(z)M_i}{eA\rho_i(z)N_A} \quad (7.3)$$

where  $N_i$  is the density of atoms in the surface,  $M_i$  is the mol weight,  $N_A$  is Avogadro's number, and  $\rho_i$  is the density of this particular element  $i$ . If we assume that  $F$ ,  $Y_i$ , and  $\rho_i$  are constants with respect to time this differential equation can easily be solved and the result is

$$z(t) = \int_0^t \dot{z} dt = \frac{FYM}{\rho N_A} t = \frac{IYM}{eA\rho N_A} t \quad (7.4)$$

This was a rather trivial example since it only applies for pure elements. Let us instead look at a two component mixture of  $A$  and  $B$  where we want to determine the depth compositions ( $C_A(z)$  and  $C_B(z)$ ). If we have two components, there will most likely be a difference in sputter yield for the two components leading to

$$z(t) = \int_0^t [C_A(t)\dot{z}_A + C_B(t)\dot{z}_B] dt \quad (7.5)$$

Since  $C_A(z)$  and  $C_B(z)$  can be estimated by the surface analysis as a function of time and since  $\dot{z}$  can be estimated if the sputtering yield is known, it is possible to construct a plot showing the concentration profile of  $A$  and  $B$  into the material as a function of depth. Unfortunately it is generally not so simple since the sputtering yields for different compositions and compounds are not well known.



### 7.2.1 The Sputter Yield

The essential parameter for doing sputter profiling is the yield  $Y$ ; the number of particles that is removed from the surface per incoming ion. The yield from a pure amorphous target can formally be written as

$$Y = \Delta F(E_0) \quad (7.6)$$

where  $\Delta$  is a factor containing all the material properties such as the surface binding energy of the atoms sputtered and  $F(E_0)$  is the energy deposited at the surface depending upon the type of ions, the energy  $E_0$ , the incidence angle of the ions, the target atoms, and the density of the atoms in the target.

The parameter  $\Delta$  can be derived describing the number of target atoms that obtains sufficient energy and momentum in the correct direction so that they can overcome the barrier and escape the surface. The result is

$$\Delta \approx \frac{0.042}{NU_0} \quad (7.7)$$

in units of [ $\text{\AA}/\text{eV}$ ] where  $N$  [ $\text{\AA}^{-3}$ ] is the density of atoms in the target and  $U_0$  [eV] is the surface binding energy of the target atoms. For details of the derivation of this expression we shall refer the reader to [32]. In Figure 7.4 the sputter yield for 400 eV  $\text{Xe}^+$  ions is plotted for most of the elements. It is clearly seen that there is a rather strong variation. More relevant data can be found in [34] where sputter yields for various ions, energies, and elements have been collected. All this works relatively well for the pure elements, but as soon as we turn to inhomogeneous samples consisting of alloys or compounds these sputter yields are in general not valid any longer since the surface binding energy changes for instance. Thus there is a general problem in converting the sputter time into a depth for more complex samples.

**Figure 7.4** The sputter yield for 500 eV Xe ions.

### 7.3 Factors Limiting Depth Resolution and Accuracy of Profiles

It is straight forward to perform a sputter profile and plot the concentration of the various components as a function of sputter time or even better as a function of ion dosage. The problem arises when we want to interpret these data in terms of depth and depth resolution.

### 7.3.1 The Effect of Attenuation

First of all, the AES-signals are not coming from a single layer but are exponentially damped signals from several layers. This means that we can never expect to obtain extremely sharp features, although the sample studied consists of such. Consider for example a thin layer of gold ( $d_{\text{Au}} = 25 \text{ \AA}$ ) deposited on top of a germanium surface and then covered by another layer of germanium  $d_{\text{Ge}} = 30 \text{ \AA}$ . It is assumed that the deposition is ideal, i.e. it is a layer by layer growth mode (see Figure 6.15). We can easily adapt Equations (6.10) and (??) to describe the intensities from the constructed sandwich. The signal from the gold will be given by

$$I_{\text{Au}} = I_{\text{Au}}^{\infty} \left( 1 - e^{-\frac{d_{\text{Au}}}{\lambda_{\text{Au in Au}}}} \right) e^{-\frac{d_{\text{Ge}}}{\lambda_{\text{Au in Ge}}}} \quad (7.8)$$

which is the gold signal from a gold layer of thickness  $d_{\text{Au}}$  damped through a germanium layer of thickness  $d_{\text{Ge}}$ . The term  $\lambda_{xiny}$  refers to the mean free path of an Auger electron from element  $x$  moving through element  $y$ . Similarly, the signal from the germanium can be written as

$$I_{\text{Ge}} = I_{\text{Ge}}^{\infty} \left( 1 - e^{-\frac{d_{\text{Ge}}}{\lambda_{\text{Ge in Ge}}}} \right) + I_{\text{Ge}}^{\infty} e^{-\frac{d_{\text{Ge}}}{\lambda_{\text{Ge in Ge}}}} e^{-\frac{d_{\text{Au}}}{\lambda_{\text{Ge in Au}}}} \quad (7.9)$$

where the first term is due to the germanium overlayer and the second term is due to the germanium substrate which is damped both through the gold layer and the germanium overlayer.

This sandwich can now be analysed by sputter profiling. If it is assumed that the sputter profiling, just as the deposition, is ideal i.e. the removal takes place layer by layer it is easy to set up the equations describing the signals as a function of time. The sputter rate can be evaluated for each of the elements (Eq. (7.4)) and the thickness of the various layers can then be estimated as a function of time as  $d = \dot{z}t$ . If it takes  $t_{\text{Ge}}$  seconds to sputter through the germanium overlayer and  $t_{\text{Au}}$  for the gold layer the time dependence of the signals are naturally divided into two intervals. The signal for the gold layer is given by

$$I_{\text{Au}}(t) = I_{\text{Au}}^{\infty} \left( 1 - e^{-\frac{d_{\text{Au}}}{\lambda_{\text{Au in Au}}}} \right) e^{-\frac{d_{\text{Ge}} - \dot{z}_{\text{Ge}} t}{\lambda_{\text{Au in Ge}}}} \quad 0 \leq t \leq t_{\text{Ge}} \quad (7.10)$$

and

$$I_{\text{Au}}(t) = I_{\text{Au}}^{\infty} \left( 1 - e^{-\frac{d_{\text{Au}} - \dot{z}_{\text{Au}}(t - t_{\text{Ge}})}{\lambda_{\text{Au in Au}}}} \right) \quad t_{\text{Ge}} \leq t \leq t_{\text{Ge}} + t_{\text{Au}} \quad (7.11)$$

The result for  $(I_{\text{Au}}(t)/I_{\text{Au}}^{\infty})$  is plotted vs. sputter time for the values  $\lambda_{\text{Au in Au}} = 5 \text{ \AA}$  and  $\lambda_{\text{Au in Ge}} = 10 \text{ \AA}$  is shown in Figure 7.5. So even in this very ideal case the profile of the gold layer is broadened. Naturally it is possible to correct for this broadening as its origin is well understood. The above intensities are all special cases of

$$I_i = \frac{I_i^{\infty}}{\lambda_i} \int_0^{\infty} C_i(z') e^{-\frac{z'}{\lambda_i}} dz' \quad (7.12)$$

where  $C_i(z')$  is the concentration of element  $i$  in depth  $z$ .

Ideally we started out with a concentration profile  $C_i(z')$  which in general is the unknown function we want to determine. The resulting intensity  $I_i(z)$  where the sputter depth  $z$  is a result of a convolution of a resolution function  $g(z - z')$  and the true concentration profile is thus

$$I_i(z) = \frac{I_i^{\infty}}{\lambda_i} C_i(z') * g(z - z') \quad (7.13)$$

$$I_i(z) = \frac{I_i^{\infty}}{\lambda_i} \int_{-\infty}^{\infty} C_i(z') g(z - z') dz' \quad (7.14)$$

So in this case where

$$g(z - z') = e^{-\frac{z - z'}{\lambda_i}} dz \quad (7.15)$$

it is well established that a routine exists for elimination of this broadening. The broadening in the profile can as a rule of thumb be estimated as  $\Delta z_{\lambda} = 1.6\lambda$ .

**Figure 6.5** The relative intensity of Gold from the sandwich as a function of sputter depth.

### 7.3.2 Other Effects

There are other effects leading both to broadening and shifts of the true profile which are not as easily dealt with. The sputtering process itself is quite a complex process and we shall here briefly mention a number of the effects that may lead to a broadening and introduce various errors when evaluating sputtering profiles.

#### Statistical Broadening

First of all the sputtering process is a random process, meaning that we should never expect to have a layer by layer removal. After some sputtering time we may have removed five layers off at one place of the surface, whereas seven layers have been removed at other places. This will lead to an additional broadening which is usually considered to be proportional to the square root of the depth in the region below 100 Å. For higher values of  $z$ ,

$\Delta z$  appears to saturate at roughly 10 Å to 20 Å.

### Broadening by Surface Roughness

Surface roughness will naturally also influence the resolution as will surface crystallography. Both effects can strongly influence the resolution as the sputter yield depends on the incoming angle of the ions. If for example a polycrystalline sample is sputtered for a long time, the sputtering itself may introduce structural changes of the surface leading to substantial broadening. This is clearly seen in Figure 7.6 where a polycrystalline zinc sample has been sputtered to a depth of 3 μm to 4 μm and subsequently studied by electron microscopy.

**Figure 7.6** Electron microscope picture of a polycrystalline crustalline Zinc sample sputtered to 3-4 μm depth.

The surface which initially appeared flat is now extremely rough and it is clear that any concentration profiles measured on such a surface will be completely smeared out. This problem can to some extent be eliminated by averaging the incidence angle of the ion beam by rotating the sample during the sputtering process. The effect is shown in Figure 7.7 where a sputter profile of a multi sandwich of Cr/Ni (each layer 500 Å thick) has been analysed with and without rotating the sample. The incident beam was  $\text{Ar}^+$  ions at 1 keV at an incidence angle of  $68^\circ$  [35]. The depth resolution for the rotated sample is clearly improved as seen in the lower panel of Figure 7.7.

**Figure 7.7** Sputter profile of a multi Ni/Cr sandwich without (top panel) and with (lower panel) simultaneous rotation of the sample.

### Preferential Sputtering

If there is a large difference in sputter yield for the various components in the sample the surface concentration of the components may be changed due to the sputtering. Thus the surface composition will change from its true value to a composition determined by the steady state solution of the removal rates of the various components. This leads to an enrichment of the component which has the lower sputter yield and the sputter profiling will reflect a too high concentration of this particular component.

### Recoil Mixing

The high energy ions hitting the surface will transfer energy and momentum to the surface atoms whereby there will be a mixing of the atoms at the surface. This in itself leads to a broadening of the profiles, but furthermore there will also be a possibility that some atoms are recoiled into the surface. This will result in a shift of the profiles to higher depths as some of the atoms are recoiled further into the sample before they are removed.

### Radiation Enhanced Diffusion and Segregation

These effects both lead to broadening and errors in the concentration profiles. Due to the many defects the sputtering inevitably introduces in the surface region it will be much easier for the atoms to diffuse around. Thus if there is a component which has a very low surface energy, this component will prefer to segregate to the surface and cause an enrichment here which does not reflect the true composition of the sample. Similarly, any sharp interface will be smeared out by diffusion.

Several of the above effects will lead to broadening and as they all have to be convoluted it is appropriate to approximate the resolution function by a Gaussian

$$g(z - z') = \frac{\pi \Delta z^2}{2} e^{-2 \left( \frac{z' - z}{\Delta z} \right)^2} \quad (7.16)$$

In general the resolution will decrease with depth as several of the discussed broadening effects are proportional to the depth sputtered. For a more detailed and rigorous treatment of the above discussed effects, the reader is referred to an excellent review by Hoffman [36] and references therein.



## **7.4 Practical Sputter Profiling**

It is seen that there are many effects which make an accurate interpretation of a sputter profile a difficult task, even in cases where sandwiches of pure elements are studied. Sputter profiles are therefore generally presented as concentration profiles as a function of ion dosage. This is often sufficient as in many cases it is only necessary to discuss qualitative differences between different samples. In the following we shall go through a few such examples.

### **7.4.1 Sputter Profile of Stainless Steel**

In Figure 7.8 and Figure 7.9 the sputter profiles of a 18-8 stainless steel sample are shown just after it had been cut off a rod and after a heat treatment at 600 °C for 600 seconds respectively.

**Figure 7.8** Sputter profile of stainless steel.

**Figure 7.9** Sputter profile of heat treated stainless steel.

In both cases a carbon contamination was observed at the surface prior to sputtering. Such a thin layer of surface contamination, is always observed on a sample that has been introduced into the apparatus from atmospheric pressure. It is readily removed after 10-20 seconds of sputtering. Also other forms of contamination like sulphur and chlorine can be observed. It is noticed that even on the non-treated surface (Figure 7.8) there is a substantial oxide layer and an enrichment of chromium at the cost of iron and nickel in the surface region. This enrichment is further developed when the sample has been heated in atmospheric air at 600 °C for 600 seconds as shown in Figure 7.9. The surface layer can be identified by XPS as seen in Figure 7.10 and consists mainly of  $\text{Cr}_2\text{O}_3$  although less than 10 % iron can still be observed.

**Figure 7.10** XPS spectra of the stainless steel sample before and after sputtering.

Approximately 500 Å to 1000 Å must be removed before bulk values of

the components are observed. The fact that it is chromium which is forming the protective oxide layer on the steel is in good agreement with the rule of thumb that it is always the most reactive component which will segregate to the surface region and be oxidised. The reactivity of the transition metals is increasing from the right to the left. Therefore, if titanium had been present in the steel we would expect this to form an oxide overlayer as well. This simple picture holds well as long as the oxide layer grown is not too thick. For very thick layers (several  $\mu\text{m}$ ) formed at high temperatures, the process becomes much more complex and NiO overlayers may be observed on top of the  $\text{Cr}_2\text{O}_3$  [37].

### 7.4.2 Investigations of Electrical Contacts

It has been mentioned that a substantial amount of all analysis performed by use of XPS and especially AES is done within the field of microelectronics. There are several problems which can be advantageously investigated with these methods and one of them is the formation of good contacts to the various semiconductors. Here we have chosen to show the contact formation to silicon. Gold usually forms good electrical contacts, but if it is deposited directly on the silicon it will readily diffuse into the silicon and be diluted. Therefore a layer of chromium is deposited on the silicon prior to the gold deposition. In Figure 7.11 the sputter profile of the contact is shown as deposited. In order to simulate ageing and use of the component it has been heated to  $300^\circ\text{C}$  for two hours and the result is shown in Figure 7.12 where it is clearly seen that the chromium layer itself is not a sufficient diffusion barrier since silicon is observed in the gold overlayer and vice versa. If the procedure is repeated but the chromium is deposited in a background gas of nitrogen some chromium nitride will be formed as shown in Figure 7.13. Performing the same ageing experiment clearly shows (see Figure 7.14) that this construction is much better since the mixing has been minimised. Thus, the chromium nitride forms a diffusion barrier for gold and silicon.

### 7.4.3 Control of Thin Coatings

Coatings are used widely in industrial processes mainly for corrosion protection or for chemical inertness. In the latter case it is very common to deposit a thin layer of gold on the surface. For example many metals that are used for bijouterie and the rim of glasses will contain nickel. This is a highly

non-desirable situation for metals in contact with the human body since it may cause allergic reactions. On the other hand, gold is a rather expensive material so the manufacturer wants to keep the layer as thin as possible. Figure 7.15 shows a sputter profile of a sample where the manufacturer was cutting the expenses too low since he was not successful in avoiding nickel at the surface. Only a few hundred Å of gold had been deposited and since gold in this sort of industrial process is usually growing in an island growth mode, there will be areas free of gold exposing the nickel.

**Figure 7.11a** Sputter profile of Gold film on Chromium on Silicon as deposited.

**Figure 7.11b** Sputter profile of Gold film on Chromium on Silicon heat treated to 300 C° for 2 hours.

**Figure 7.12a** Sputter profile of Gold film on Chromium-nitride on Silicon as deposited.



**Figure 7.12b** Sputter profile of Gold film on Chromium-nitride on Silicon heat treated to 300 C° for 2 hours.

**Figure 7.13** Sputter profile of glass rim consisting of Nickel coated with Gold.

## 7.5 Problems

1. In the semiconductor industry it is often a requirement to be able to make good electrical contact to silicon wafers. This is often done by evaporating a thin film of gold upon the silicon. The evaporation rate is, however, in our case not known. The rate is, therefore, estimated by sputter profiling, that is measuring the surface composition while bombarding it with 2.0 keV Ar ions. The ion fluency is measured to be  $5 \mu\text{A}/\text{cm}^2$ . It takes 22 minutes before the gold disappears and the silicon appears. This is idealised, how does it look in reality?. The sputter yield has earlier been determined to be 2.6 Au atoms per Ar ion. Determine the thickness of the gold overlayer. How long time will it take to sputter through a silicon layer of a similar thickness when the sputter yield for Si is  $\sim 0.4$ ? Which assumptions/complications must be considered using this method? Propose another and better method for determination of film thickness in this thickness regime.
2. Consider a sandwich structure consisting of a Si substrate on which one monolayer of Ge ( $2.5 \text{ \AA}$ ) has been deposited and then  $25 \text{ \AA}$  Si on top. Finally the sandwich was terminated by another monolayer of Ge. All layers were grown epitaxially i.e. layer by layer. In order to test the process the sample was controlled by sputter profiling using AES. The Ge LMM (1147 eV), MVV (52 eV) Auger lines and the Si LVV (92 eV) are measured as a function of sputter time. In the following we will assume that the sputter process is ideal and removes the overlayer layer by layer (discuss the complications of sputter profiling). Show how the intensities of the Ge lines as well as the Si line develops with sputter time. Give the relevant equations and discuss the approximations. Which of the two Ge lines would you use in order to get a good quality control? Are there ways to improve the profile?

## Chapter 8

# Vibrational Spectroscopies HREELS and IR

Both the High Resolution Electron Energy Loss Spectroscopy (HREELS) and Infrared Adsorption Spectroscopy (IRAS) or just IR rely on vibrational excitation of molecules adsorbed on surfaces. HREELS can in general only be used on nice and plane single crystal surfaces under UHV conditions, whereas the IR method is much more applicable and can be used both on well defined surfaces (reflection IR) and on real catalysts (transmission IR and Diffuse Reflectance IR). It can even be used at relatively high pressures, making it useful for investigating real catalysts *in situ*. One of the advantages of using HREELS is that it can even go to very low frequencies meaning that energy losses due to phonons etc. can be investigated. The resolution in the IR experiments are usually much better than HREELS, but when molecules are adsorbed on surfaces the relaxation time is short due to the coupling to the surface eliminating some of this advantage. For more extensive treatment of these methods we will refer to [38, 5, 1].

### 8.1 High Resolution Electron Energy Loss Spectroscopy

#### 8.1.1 Experimental Set-up

The HREELS experiments refers as the name says to high energy resolution since the energy loss spectroscopy also comes in a version where that is not

the case. Earlier in Chapter 3 we saw how electrons generated by an electron gun could be used to investigate the various energy losses mechanisms such as plasmon energy losses or losses by ionisation. However, energy losses to vibrations and phonons are very small and cannot be observed if the energy distribution of the electrons is not very narrow, say, below 10 meV. The way to achieve monochromatised electron beams is by using low primary energies and then use an energy analyser to select the appropriate energy. This is illustrated in Figure 8.1.

**Figure 8.1** Schematic drawing of a HREELS experiment.

The electrons are generated the usual way by heating a filament at a desired potential, the primary energy, which typically is less than 10 eV. The electrons are then energy analysed by passing through an analyser, typically with a resolution in the range 1 meV to 5 meV, and then directed onto the sample. The electrons are interacting (reflected) with the sample and will

in some cases also undergo an energy loss. The energy distribution of the reflected electrons is analysed by a second analyser which can be rotated around the specular direction. The experiment is not as easy to perform as those mentioned earlier. It is not trivial to get optimum resolution and at the same time a reasonable intensity. Also special precautions must be taken so that the slow electrons does not get detracted by any external fields, i.e. the set-up must be screened from magnetic fields (also the earth's field) by being encapsulated in a  $\mu$ -metal. The  $\mu$ -metal is a special alloy which leads the magnetic field lines in the metal screening the interior. Similarly the electron beam is also disturbed easily by changes in work function of the materials used in the analysers. The inside of the analyser is therefore coated with a graphite ensuring a uniform work function.

### 8.1.2 The Energy Loss Spectrum

A typical HREEL spectrum is shown in Figure 8.2. At zero energy loss we find the elastically scattered electrons that have only been reflected from the surface. The overall resolution of the experiment is determined by the FWHM of this elastic peak. The intensity of the energy losses are typically two orders of magnitude weaker and depends on the nature of the excitation

mechanism which can be divided into dipole scattering and impact scattering.

**Figure 8.2** A HREEL spectrum of CO adsorbed on Ir(100). Notice that the resolution is below one meV. Taken from [39]

### Dipole Scattering

In this mechanism the electron is first of all reflected elastically by the surface leading to a high intensity of electrons in the specular direction. An electron approaching a metal surface will set up a time dependent electric field that will be screened by the metal surface so that there is no field in the metal. This is described by an image charge with opposite sign travelling in the metal. The resulting electric field will be orthogonal to the surface and can be described in the frequency domain as

$$E(t) = \int E(\omega) e^{-i\omega t} d\omega \quad (8.1)$$

This electric field will thus contain a frequency component equal to that of the vibrating molecule and couple with any dynamic (time-dependent) dipole moment on the surface. Consider for example a CO molecule adsorbed standing on the surface. The CO molecule is polarised and possesses a very strong dynamic dipole moment along the molecular axis. This dipole moment is further enhanced by the fact that the field from this dipole is screened by the metal resulting in a mirror dipole with the same sign. The interaction Hamiltonian for this will naturally be

$$\mathbf{H}_{int} \propto \vec{E} \cdot \vec{\mu} \quad (8.2)$$

where  $\vec{E}$  is the time-dependent electric field from the electron and  $\vec{\mu}$  is the dipole moment operator for the CO molecule. The probability of exciting the vibration of the molecule will then again be given by Fermi's golden rule where

$$P_{if} = | \langle \Psi_i | \mathbf{H}_{int} | \Psi_f \rangle |^2 \quad (8.3)$$

Since the electron undergoing the elastic scattering on the surface is setting up the electric field over a long range this energy loss may already start to happen when the electron is far from the surface ( $< 100 \text{ \AA}$ ). The inelastic scattering is predominantly a forward scattering so the change in momentum to reflect the electron is supplied by the substrate.

It is now obvious that there will be a simple selection rule for the dipole scattering since vibrations involving dipoles parallel with the surface will be extinguished due to the metallic screening and no transitions will be possible. This is illustrated schematically in Figure 8.3

It is seen that the probability depends strongly on the size of the dipole. For example CO has a strong dipole orthogonal to the surface when it is adsorbed in an up right position. This makes it possible to measure even remote amounts of CO (typically a few per mille of a monolayer) on a surface. Unfortunately the size of the dipole is only constant in the low coverage regime. When the coverage increase the dipoles will start to interact with each other leading to screening and depolarisation so the energy loss intensity



is no longer simply proportional to the coverage.

**Figure 8.3** Schematic drawing of the selection rules for dipole scattering.

### **Impact Scattering**

In the case of impact scattering short range interactions are involved taking place when the electron interact with the potential of the atoms i.e. distances on the order of 1 Å. In this case the electrons are scattered over a wide range of angles and are, contrary to dipole scattering, not directed in the specular direction. The mechanism for excitations are also very different and there are no simple selection rules like in the dipole scattering. This means that in principle, it is possible to measure the dipole forbidden energy losses. Unfortunately the impact scattering is in general rather weak and is most often only observed when going away from the specular direction. Here

the dipole component dies off rather quickly whereas the impact scattering persists as mentioned above as it is much more isotropic. In this manner it is possible to distinguish the two contributions from each other. It should for completeness' sake also be mentioned that there is a third mechanism called *Negative ion resonances*. Here the electron is captured in an orbital forming a short lived negative intermediate losing energy before being re-emitted.

### 8.1.3 Experimental Results

The method can be used to identify unknown intermediates on a surface and in some cases also be used to investigate the orientation of the adsorbate and even at what sort of site it is adsorbed. For example HREELS was used to identify that formate is formed when a Cu(100) crystal is exposed to several bars of CO<sub>2</sub> and H<sub>2</sub> at a temperature below 363 K. The spectrum shows the energy losses characteristic for formate bound bidentate to the surface and the appropriate isotope shift for the C-H and C-D vibration was also found. The spectrum is shown in Figure 8.4. Please note that it is also possible for the electrons to gain energy from excited vibrations if the population is

sufficiently high.

**Figure 8.4** The HREEL spectra of the intermediates formed by exposing a Cu(100) crystal to gas mixtures of  $\text{CO}_2 + \text{H}_2$  and  $\text{CO}_2 + \text{D}_2$  respectively. The energy losses are characteristic for formate and the C-H vibration undergoes the expected shift upon isotropical labeling. Taken from [40]

Any gas phase molecule with  $N$  atoms will have  $3N$  degrees of freedom. Thus a CO molecule in the gas phase will have 6 degrees of freedom, 3 translational, two rotational, and one vibrational mode. When the molecule adsorbs on the surface the rotational and translational modes become converted into frustrated vibrational modes as 2 frustrated rotational modes and 3 frustrated translational modes. Of these modes only the frustrated translational mode is orthogonal to the surface, dipole active, whereas the other modes usually only have weak dipoles in the surface plane and therefore forbidden. The different modes for atomic hydrogen and CO adsorbed on a substrate is

shown in Figure 8.5.

**Figure 8.5** The number of modes of atomic hydrogen and CO in different adsorption symmetries. Degenerate mode are shown next to each other [41].

Thus only two energy losses should be expected for a CO molecule adsorbed standing up on the surface. These are observed at roughly 260 meV (C-O vibration) and at 60 meV (substrate-CO or frustrated translational mode, see Figure 8.2). (Simply divide by 8 for conversion from  $\text{cm}^{-1}$  to meV). The other modes should in principle also be observable in the off-specular mode where impact scattering dominate, but they are weak and have low frequencies making them difficult to observe on the high background from the elastic peak. One example where the number of the dipole forbidden modes have been used to identify the bonding site is H on W [42] (see figure 8.6). Here the vibration of the H atom normal to the surface is easily identified in specular scattering as  $\nu_1$ . However when going away from the specular

direction two other modes are identified as the two translational frustrated modes along the surface. Since there are two and not one mode, which then would be degenerated, the H atom must be bridge bonded since an on top or a four fold hollow site would lead to degeneration of  $\nu_2$  and  $\nu_3$ .

**Figure 8.6** HREEL spectra of H-W(100)( $\sqrt{2} \times \sqrt{2}$ )R45° measured with an electron beam with primary energy of 5.5 eV at 60° [42].

The size of the energy loss for a specific surface mode may also give information on the bonding site, although much care must be exercised here. According to Effective Medium Theory (EMT) any adsorbate will adsorb on a surface in a distance from the surface where it obtains its optimum electron density  $n_s$ . The binding energy will always have a minimum as a function of  $n_s$  since at low electron density there are no overlap and thus no binding and at the very high electron density the Pauli repulsion takes over. Thus in this simple picture the bonding geometry only depends on  $n_s$  and there will be no distinction between different adsorption sites like on-top, bridge or hollow sites. There are, however corrections to this model where the binding energy is given by

$$\Delta_{Bonding} = E(n_s) + E_{AS} + E_{1El} \quad (8.4)$$

These correction terms determines where the adsorption will take place. The term  $E_{AS}$ , which is the Atomic Sphere correction, describes the repulsion occurring when to atoms comes close to each other. This means that it is in general most favourable for atoms to adsorb in high coordination sites since this gives the highest distance to the other atoms minimising the repulsion term when located in the optimum electron density. This explains why species like carbon, nitrogen, oxygen and sulphur usually are found in three or four fold hollow sites. When this is not the case it is due to the last

correction term, the one electron correction.

**Figure 8.7** HREEL spectra of CO adsorbed on Ni(111) and Pt(111) [38].

Which trends can then be expected for atoms adsorbed on different sites on the surface? It is obvious that an atom sitting in a fourfold coordinated site will feel a much slower variation in the electron density (and thus the resulting binding potential) as it vibrates orthogonal to the surface compared to an atom sitting for example in an on top site. In the latter case there will in principle only be one atom to supply the necessary electron density and as the electron density decays exponentially from the atom in the EMT the potential will vary much faster resulting in a steeper potential and thus in

a higher frequency. Thus the trends for vibration energies predicted from this simple picture are hollow  $\downarrow$  bridge  $\downarrow$  on top adsorption sites. An example of this behavior is shown in Figure 8.7 where the HREEL spectra of CO adsorbed on Ni(111) and Pt(111) are shown. It is seen how the on top sites on Pt(111) leads to a significantly higher frequency for both the energy losses to CO.

## 8.2 Infrared Adsorption Spectroscopy

Infrared spectroscopy is well known from analysis of chemical compounds in the gas phase. It can also be used for studying adsorbates on solid surfaces. One way to this is very similar to the HREELS experiment where the infrared light is deflected from a plane surface for example a single crystal surface. This method is referred to as Infrared Reflectance Adsorption Spectroscopy (IRAS) or (RAIRS) depending on where the "infrared" is put in. Here the light is sent in nearly parallel to the surface and again only the components that are dipole active on the surface may adsorb the light. The reflected light is measured and the absorbance can be measured. The advantage here is that it is possible to measure in a background of gas although care should be taken not to confuse gas phase adsorption with adsorbate adsorption.

The greatest advantage of IR is that it can be used to study real catalysts *in situ* in the transmission or reflectance mode. In the first case less than 0.1 g of catalyst is pressed into a thin disk a few tenths of a mm thick. Transmission IR can then be used if the absorbance of the catalyst support material is low. This is typically the case when using oxides and considering wavenumbers greater than  $1000\text{ cm}^{-1}$  which is equivalent to 125 meV. It is also important that the size of the catalyst particles are smaller than the wavelength of the infrared light since otherwise scattering would ruin the experiment. Often the absorbance of the catalyst itself make transmission impossible and then Diffuse Reflectance Infrared Fourier Transform Spectroscopy (DRIFTS) may be used to measure the adsorption by surface species. Here the diffuse light scattered from a powder sample of catalyst is collected and analysed. Just as in the transmission mode the adsorption is measured and it is in this manner possible to study different intermediates adsorbed on the catalyst while running in almost realistic conditions taking the same precautions as mentioned above. By comparing observed absorbance bands to those measured on well defined surfaces it is possible to identify various species on the active cata-



lyst. An important step towards closing the material gap. Figure 8.8 depicts a typical DRIFT spectrum of methanol synthesis.

**Figure 8.8** DRIFT spectrum of a working methanol catalyst Cu/ZnO/Al<sub>2</sub>O<sub>3</sub> in steady state at 30 bar and 413 K taken from [43]

# Chapter 9

## Low Energy Electron Diffraction LEED

### 9.1 Surface Crystallography

Surface crystallography is just a special case of bulk crystallography where the crystal has been divided by a mathematical plane. We will only consider the terminology involving surfaces and some of the most often used concepts and encountered structures for metals namely Face Centered Cubic (FCC) Body Centered Cubic (BCC) and Hexagonal Close-Packed (HCP) lattices shown in Figure 9.1. For the more special structures like for instance the

diamond structure we will refer to the literature [44, 45].

**Figure 9.1** The unit cell for the FCC, BCC, and HPC lattices.

### 9.1.1 Crystal Planes

Since the surface structure and geometry is very important in many cases, for example when considering reactivity, and since it differs a lot from one surface structure to another it is important to have a notation that describes the various surfaces in a unique manner. The crystal surfaces are described by the vector normal to the surface given by

$$\vec{H} = h\vec{x} + k\vec{y} + l\vec{z} \quad (9.1)$$

and the notation is the name of the substrate and the surface normal vector ( $hkl$ ), for example Cu(100). Please note that the permutations Cu(100), Cu(010), and Cu(001) all describes the same surface as shown in Figure 9.2 for the cubic crystals. Negative numbers are noted by a bar over the number so Cu(100) is naturally equal Cu(0 $\bar{1}$ 0). The three basal planes for the cubic crystals are (100), (110) and the (111). The respective cuts are shown

in Figure 9.2 and the relative positions of the surface atoms are shown in Figure 9.3.

**Figure 9.2** The basal planes formed by cuts of the unit cells of the simple crystal structures.

An important parameter for surfaces are often the density of atoms in the surface. Note that for FCC crystals the (110) is the most open whereas the (111) is the most close packed. For BCC crystals it is the opposite order i.e. the (111) most open and (110) most close packed. Also more complicated surface structures containing steps or even kinks may be described in this notation as  $n(h_t k_t l_t) \times (h_s k_s l_s)$  where  $n$  describes that the surface contains  $n$  rows of atoms forming a terrace of  $(h_t k_t l_t)$  and one step of type  $(h_s k_s l_s)$ . Thus a (775) surface is equivalent to  $6(111) \times (11\bar{1})$ . In this manner all sorts of surfaces may be constructed, but the question is naturally whether they

are stable or will facet into other structures.

**Figure 9.3** The surface structures of the basal planes for the FCC and BCC.

A particular surface structure may be prepared by spark cutting a single crystal normal to the desired direction. The crystal is usually oriented by Laue X-ray diffraction with an accuracy better than  $0.5^\circ$ . The surface is then polished with polish paste with decreasing grain size until all scratches etc. are removed and a mirror like surface is obtained. Sometimes, in particular for the soft materials like Cu, an additional electro polish is needed to remove damaged layers. Finally the crystal is mounted in the UHV chamber and is cleaned by repeated cycles of sputtering and annealing. Getting a clean single crystal surface may be tedious work and may take several months. The cleaning procedure varies from element to element and usually effective and successful recipes can be found in the literature.

### 9.1.2 Adsorbate Sites

The definition of the most frequent adsorption sites are shown in Figure 9.4. They are named on-top site, bridge sites (may be long or short bridged), and hollow sites which may be three fold hollow or four fold hollow. In for example the FCC(111) cases it is also necessary to distinguish between HCP and FCC sites describing whether there is an atom just below the site or it is in the second layer.

**Figure 9.4** The adsorption sites for various surfaces geometries.

### 9.1.3 The Two-Dimensional Lattice

A two-dimensional structure processing periodicity can be described by a two dimensional lattice. Any point in this lattice can be reached by a suitable combination of basis vectors. Two unit vectors will describe the smallest cell

in which an identical arrangement of the atoms is found. The whole lattice can then be described by moving this unit cell by any linear combination of the unit vectors. These vectors form the *Bravais* lattice which is the set of vectors by which all points in the lattice can be reached.

## 9.2 Low Electron Energy Diffraction

### 9.2.1 Experimental Set-up

Having defined the fundamental structure we will now turn to the Low Electron Energy Diffraction Experiment (LEED). The first experiment made realising that electrons could be used for investigating surface structures was made by Davidson and Germer in 1927 [46], but as the crystals could not be kept clean (due to poor vacuum) it was not until the late sixties that the method started to take off. Several excellent reviews and monographs have been written on this subject [47, 48, 49, 5]. The experiment relies on the duality of electrons which in some case should be considered as particles and under other conditions as wave packets. If we choose to use electrons with energy around the minimum in the universal curve (40 eV to 200 eV) where we have the maximum surface sensitivity the wavelength of the electrons will be comparable with the lattice distance of single crystals considered here.

$$\lambda = \frac{h}{p} \quad (9.2)$$

$$p = \hbar k = \sqrt{2mE_p} \quad (9.3)$$

$$\lambda(\text{\AA}) = \sqrt{\frac{150.4}{E_p(\text{eV})}} \quad (9.4)$$

This means that the electrons may be scattered elastically in the surface and undergo constructive and destructive interference. The back scattered electrons are then analysed and from that the symmetry of the surface may be deduced.

The experimental set-up is shown in Figure 9.5. A beam of electrons with energy  $E_p$  from a relative simple electron gun mounted in the center of the LEED optics is directed towards the surface. The crystal is mounted so it can be positioned in the center of four concentric hemispherical grids. The inner

grid is grounded whereas the two middle grids are kept on a negative potential slightly below  $E_p$  so only electrons which has not undergone any energy losses are allowed to pass. Between the last grid and an outer fluorescent screen there are a potential difference between 2 kV to 5 kV so the electrons that passes are accelerated towards the fluorescent screen where they will form observable spots. The screen is transparent so the spots can be observed from behind it as well without being obstructed by the sample mount. The spots can then be photographed or followed by a CCD camera. More elaborate set-ups have been constructed for Spot Profile Analysis LEED (SPALED) where the detailed profile can reveal details on the long range structure, but that will not be considered here.

**Figure 9.5** Schematic drawing of a LEED optics.



In Figure 9.6 is such a LEED pattern reproduced from [50].

**Figure 9.6** LEED pattern obtained from a Cu(100) surface reconstructed by adsorption of atomic hydrogen. The energy of the electrons was relative high  $E_p = 178$  eV and the beam was normal to the surface. On a clean Cu(100) only the bright spots are observed. From [50].

The principle of the experiment is shown schematically in Figure 9.7 where an incoming electron beam interacts with a crystal described by  $\vec{a}_1$  and  $\vec{a}_2$ . The (00) beam is reflected directly back into the electron gun and can therefore not be observed unless the crystal is tilted.

The intensity of the spots formed on the screen can also be followed as a function of primary energy  $E_p$ . The spots will move towards the zero order spot with increasing energy and then varying strongly in intensity. The diffraction in the two-dimensional lattice lead to the diffracted beams indicated in Figure 9.7 whereas the  $d$  modulation of the intensity as a function

of  $E_p$  is due to diffraction between subsequent layers into the crystal. We will first concentrate on understanding the diffraction pattern which reveals the two-dimensional symmetry of the surface layers and in the end of this chapter briefly touch upon the intensity variation, which can be used to determine the distances in the surface structure.

**Figure 9.7** Schematic drawing of the LEED experiment on a single crystal spanned by  $\vec{a}_1$  and  $\vec{a}_2$ .

### 9.2.2 Kinematic Theory

The direction of the diffraction beams can be found by first considering what happens when an electron interacts with atoms in the surface. The differential scattering cross section for an elastic collision of an electron with a fixed atom is given by the asymptotic solution to the Schrödinger equation:

$$\frac{-\hbar^2}{2m}\nabla^2\Psi + V\Psi = E\Psi \quad (9.5)$$

Far away from the atom  $V = 0$  and the asymptotic solution to  $\Psi$  can be written as a sum of an incoming plane wave and an outgoing spherical wave:

$$\Psi = e^{i\vec{k}\vec{r}} + f(\alpha, \phi) \frac{e^{i\vec{k}\vec{r}}}{r} \quad (9.6)$$

where  $f(\alpha, \phi)$  is the amplitude of the outgoing electron and  $|f(\alpha, \phi)|^2$  is the differential scattering cross section which must be found by solving the Schrödinger equation in the vicinity of the atom where  $V \neq 0$ .  $\alpha$  and  $\phi$  are the angles of the scattering. Assuming that the potential is spherically symmetrical the solutions to the Schrödinger equations are separable in the coordinates  $r, \alpha, \phi$  and the wave functions are of the hydrogen type namely a product of radial and spherical harmonic:

$$\Psi_n(r, \alpha, \phi) = R_n(r)Y_{l,m}(\alpha, \phi) \quad (9.7)$$

where  $n, l$  and  $m$  are the principal, azimuthal and magnetic quantum numbers, respectively.

The amplitude of the scattered electrons can be described as an expansion of phase shifted Legendre polynomials where the phase shift comes from the interaction with the potential  $V$ . Usually a band structure potential have been used for  $V$  when describing atoms in a solid. For details on scattering of electrons on potentials we will refer to standard quantum mechanics [51, 52].

What happens when considering more than one atom scattering the incoming electrons? Firstly, consider a plane wave scattering on two atoms separated by a distance of  $R$ . This would lead to two spherical waves interfering at the position of the observer (see Figure 9.8). The difference in

phase of the two waves  $\Delta$  is given by

**Figure 9.8** An incoming electron with wave vector  $\vec{k}$  scatters on two atoms with distance  $\vec{R}$ .

$$\Delta = e^{i\vec{k}\vec{R} + i\vec{k}r_1 - i\vec{k}r_2} \quad (9.8)$$

If the observer is far away, which is always the case here, then  $r_1 \approx r_2 \gg \vec{R}$  leading to  $r_2 \approx r_1 + R \cos(\theta)$ , thus

$$\Delta \approx e^{i\vec{k}\vec{R} + ikr_1 - ik(r_1 + R \cos(\theta))} \quad (9.9)$$

$$\Delta \approx e^{i\vec{R}(\vec{k} - \vec{k}')} \quad (9.10)$$

$$\Delta \approx e^{i\vec{R}\Delta\vec{k}} \quad (9.11)$$

where  $\vec{k}'$  is parallel to  $\vec{r}_2$  and  $\Delta\vec{k}$  is the difference between  $\vec{k}$  and  $\vec{k}'$ .

The amplitude of the wave seen by the observer will be proportional to the phase difference. If we now turn to a unit cell which may contain several different atoms the amplitude from this  $F(\Delta k)$  can be found by summing over the contributions from the  $i$ 'th atom in the unit cell as

$$F(\vec{\Delta k}) = \sum_i f_i(\vec{\Delta k}) e^{i\vec{r}_i \cdot \vec{\Delta k}} \quad (9.12)$$

where  $f_i$  is the so called "form factor" which is dependent on the potential for the various atoms.

Let us now consider a two-dimensional lattice described by the vectors  $\vec{a}_1$  and  $\vec{a}_2$  as shown in Figure 9.7. The crystal is considered to be finite and consisting of  $M$  atoms in the  $\vec{a}_1$  direction and  $N$  in the  $\vec{a}_2$  direction.

The amplitude  $\Delta(\vec{\Delta k})$  from this plane can be found by summing over all the phase differences between the electrons scattered on each unit cell leading to:

$$\Delta(\vec{\Delta k}) = F(\vec{\Delta k}) \sum_{m=0}^{M-1} e^{im\vec{a}_1 \cdot \vec{\Delta k}} \sum_{n=0}^{N-1} e^{in\vec{a}_2 \cdot \vec{\Delta k}} \quad (9.13)$$

Remembering that

$$\sum_{m=0}^{M-1} x^m = \frac{1 - x^M}{1 - x} \quad (9.14)$$

$$\Delta(\vec{\Delta k}) = F(\vec{\Delta k}) \frac{(1 - e^{iM\vec{a}_1 \cdot \vec{\Delta k}})(1 - e^{iN\vec{a}_2 \cdot \vec{\Delta k}})}{(1 - e^{i\vec{a}_1 \cdot \vec{\Delta k}})(1 - e^{i\vec{a}_2 \cdot \vec{\Delta k}})} \quad (9.15)$$

It is not the amplitude but the intensity which is interesting so we would have to multiply the amplitude by its complex conjugate and by using the cosine relations we find

$$I(\vec{\Delta k}) = \frac{\sin^2 \left( M/2 \vec{a}_1 \cdot \vec{\Delta k}_{\parallel} \right) \sin^2 \left( n/2 \vec{a}_2 \cdot \vec{\Delta k}_{\parallel} \right)}{\sin^2 \left( 1/2 \vec{a}_1 \cdot \vec{\Delta k}_{\parallel} \right) \sin^2 \left( 1/2 \vec{a}_2 \cdot \vec{\Delta k}_{\parallel} \right)} \quad (9.16)$$

since  $\vec{a}_1 \cdot \vec{\Delta k} = \vec{a}_1 \cdot \vec{\Delta k}_{\parallel}$  as  $\vec{a}_1$  is located in the surface plane.

Now it is possible to see that there will only be an intensity in specific directions namely when the denominator goes towards zero i.e. when:

$$\vec{a}_1 \Delta \vec{k}_{\parallel} = h 2\pi \quad (9.17)$$

$$\vec{a}_2 \Delta \vec{k}_{\parallel} = l 2\pi \quad (9.18)$$

$$h, l \in \mathbb{Z} \quad (9.19)$$

Thus for a plane of sufficient dimensions and when the observer is far away from the plane the spherical waves scattered from each unit cell will give rise to localised beams diffracted in directions parallel to the surface so they obey the above relations characterised by the indices  $h$  and  $l$ .

### The Reciprocal Lattice

When having a real-space lattice defined as above where for example

$$\vec{r}_{m,n} = m\vec{a}_1 + n\vec{a}_2 \quad (9.20)$$

it is possible to define a reciprocal lattice vector in the plane given by

$$\vec{g}_{h,l} \equiv h\vec{a}_1^* + l\vec{a}_2^* \quad (9.21)$$

where the basis vectors of the reciprocal lattice are defined as:

$$\vec{a}_1^* \equiv 2\pi \frac{\vec{a}_2 \times \vec{z}}{\vec{a}_1 \cdot \vec{a}_2 \times \vec{z}} \quad (9.22)$$

$$\vec{a}_2^* \equiv 2\pi \frac{\vec{z} \times \vec{a}_1}{\vec{a}_1 \cdot \vec{a}_2 \times \vec{z}} \quad (9.23)$$

where  $\vec{z}$  is the vector normal to the surface and the denominator is the volume of the unit cell.

$$\Delta \vec{k}_{\parallel} = \vec{g}_{h,l} \quad (9.24)$$

This means the diffracted beam occurs when the change in momentum parallel to the surface equals a reciprocal vector or linear combination thereof. Let us try to relate this information to the spot we see on our screen. That we have a spot means that a diffracted beam  $(h, l)$  crosses our LEED optics as shown in Figure 9.9. In a conventional LEED optic the radius of the screen

$R$  is known. By observing the position of the spot we can thus determine the angle  $\theta_{h,l}$  the diffracted beam has been scattered.

**Figure 9.9** Cross section of the experimental setup. Radius of the screen is  $R$  and the beam  $(h,l)$  gives a spot a distance  $d_{h,l}$  measured from the zero order spot.

$$\sin \theta_{h,l} = \frac{d_{h,l}}{R} = \frac{g_{h,l}}{k} \quad (9.25)$$

where  $k$  is the wave vector of the electron. (We are assuming normal incidence of the incoming beam. This is not a necessity, but simplifies the experiment). It is seen that the distance seen on the screen  $d_{h,l}$  is inversely proportional to the square root of the energy, meaning that all spots will converge towards the zeroth order spot for high energies as mentioned earlier. This is a good method for identifying the zero order spot. It is also possible to give an

estimate of the lattice distance of the crystal by measuring the distance  $d_{1,0}$ , which is between the first order spot  $(1, 0)$  and the zeroth order spot  $(0, 0)$ . Since  $g_{1,0} = 2\pi/a_1$  the lattice distance is given by:

$$a_1 = \frac{2\pi R\hbar}{d_{1,0}\sqrt{2mE_p}} \quad (9.26)$$

Since the spots are usually not extremely sharp this is not a very accurate method for determining lattice distances.

### The Coherence Length

The diameter of the spot seen on the screen depends critically on the level of order on the surface, the quality of the electron beam used and the temperature of the crystal. Let us first assume that we have an ideal electron beam i.e. the electron trajectories are all parallel and the beam is monochromatised. If we look at a spot profile the intensity will be given by:

$$I(\vec{\Delta k}) = \frac{\sin^2(M/2\vec{a}_1\vec{\Delta k}_{\parallel})}{\sin^2(1/2\vec{a}_1\vec{\Delta k}_{\parallel})} \quad (9.27)$$

which can be approximated as

$$I(x) \propto \frac{\sin^2(x)}{x^2} \quad (9.28)$$



where  $x = M/2\vec{a}_1\Delta\vec{k}_{\parallel}$  and the intensity profile is shown in Figure 9.10.

**Figure 9.10** The intensity of spot profile as a function of  $x$  defined in the text.

It can be shown that the FWHM of the spot is given by  $\vec{a}_1\Delta\vec{k}_{\parallel} = 0.44\pi/M$  meaning that if there are just ordered areas bigger than, say, 30 by 30 atoms this effect will no longer contribute significantly to the broadening of the observed spots. Thus LEED is not very useful for determining the overall order of a surface since it only reflects the areas that are ordered and discriminates those which are disordered. If one however observes a LEED pattern with diffuse spots the surface order is certainly of poor quality.

Usually it is the quality of the electron gun that sets the limit of how sharp the spots can be. The beam diameter will normally be of the order of 0.1 mm to 1.0 mm, which is the area the LEED experiment is probing. Unfortunately the beam energy is not monochromatised and completely parallel.

The energy resolution is as we shall see of less importance, but both effects contribute to an uncertainty of the parallel momentum  $\Delta\Delta k_{\parallel}$  of the incoming beam, which will be reflected in the outgoing beams. This uncertainty in the beam can be translated into a transfer width  $W$  given by

$$W = \frac{2\pi}{\Delta\Delta k_{\parallel}} \quad (9.29)$$

where

$$\Delta k_{\parallel} = 2\pi\sqrt{\frac{E_p}{150.4}}(\sin(\theta_{out}) - \sin(\theta_{in})) \quad (9.30)$$

By neglecting contributions from  $\theta_{out}$  and assuming normal incidence we find the respective uncertainties for divergence and energy by differentiation. From those we can estimate the respective transfer widths to:

$$W_{\theta_{in}} = \frac{\lambda}{\cos(\theta_{in})\Delta\theta_{in}} \quad (9.31)$$

and

$$W_{E_p} = \frac{4\pi E_p}{\Delta k_{\parallel}\Delta E_p} \quad (9.32)$$

Substituting realistic values for a conventional LEED system like  $E_p = 100$  eV,  $\Delta E_p = 0.5$  eV,  $\Delta\theta_{in} = 0.6^\circ$  and  $2\pi/\Delta k_{\parallel} = 2.5$  Å we get  $W_{\theta} = 100$  Å and  $W_E = 1000$  Å. It is obvious that the uncertainty of the beam convergence is dominating meaning that as long as we have ordered islands on the surface that are larger than the transfer width of our LEED optics we will not be able to notice an effect on the sharpness of the spots. Normally we are talking about a coherence length on the order of 100 Å to 200 Å meaning that we can have a crystal which in LEED will appear well ordered, but locally may have areas that are completely disordered. This may first be realised when Scanning Tunneling Microscopy (STM) experiments are performed since that method is very sensitive to the local order. By optimising the experimental set-up it is possible to obtain electron beams in which the electron trajectories are parallel to a high degree. In this manner the uncertainty of the angle can be eliminated and long range order may be observed. The detail are investigated by spot profile analysis and referred to as SPALEED. The experiment requires dedicated equipment and is commercially available.

For completeness it should also be mentioned that the temperature of the sample have a profound effect on the spot profile since the atoms in the surface oscillates due to the phonons. This gives an uncertainty of the positions of the surface atoms which will naturally result in a decreasing intensity and broadening of the LEED spots. Thus it is preferable to stay at room temperature or lower when doing LEED experiments. The intensity is given by:

$$I = I_0 e^{-2M} \quad (9.33)$$

where

$$2M = \frac{12h^2T}{mk_B\theta_D^2} \left( \frac{\cos(\phi)}{\lambda} \right)^2 \quad (9.34)$$

where  $\phi$  is the scattering angle,  $\lambda$  is the wavelength, and  $\theta_D$  is the Debye temperature. By plotting  $\log I$  vs. temperature the Debye temperature can be extracted. At low mean free paths it will primarily be the Debye temperature of the surface layer which is lower than that of the bulk.

### 9.2.3 Multiple Scattering

Above we have only considered one plane of atoms but the scattering process will in general always take place in several non-equivalent layers. This is the effect that will cause modulation of the diffracted beam as mentioned earlier leading to the IV-curves. A first glance one could expect the resulting LEED patterns just to be a sum of the scattering in the different non-equivalent planes. This would be the case if the electrons were only scattered once, but that is not the case since the cross section for scattering is rather large. Electrons scattered in the second layer may also be scattered in the first layer and vice versa leading to a convolution of the diffraction. The resulting LEED patterns must therefore be found by determining the coincidence lattice which is the lattice formed by all the non-equivalent layers. I.e. when determining the unit cell of the adsorbate and the substrate one must find the unit cell that repeats the symmetry of both. We shall look at an example later to demonstrate this principle.

### 9.2.4 Notation and Examples

In the following will first look at the notation for the different surface structures and then give some examples.

As we have seen a real space surface lattice in a LEED experiment will be reflected as a reciprocal lattice on the LEED screen. We can say that the LEED pattern is just a Fourier transform of the real space lattice. Starting out with the simple basal planes the respective LEED patterns are found by finding the respective reciprocal lattice vectors. This is the typical starting situation when doing experiments where the first LEED pattern is obtained in order to check the structure and to some extend the quality of the crystal. This pattern is referred to as the  $1 \times 1$  structure. Now lets consider what happens if we adsorb 0.25 monolayer of sulphur on for example a Ni(100) surface. The sulphur is known to prefer four fold hollow sites as indicated in the real space model shown in Figure 9.11. The new unit vectors in real space will be the same as those of the Ni(100) substrate except that they are twice as long. The respective LEED pattern is found by finding the respective reciprocal basis vectors using the formulas above. Since the new basis vectors was twice as long in real space they will now be half as long in reciprocal space leading four times as many spots in the respective LEED

pattern.

**Figure 9.11** Schematic real space model of a quarter and a half monolayer of sulphur adsorbed on Ni(100) and the respective LEED pattern.

### Woods Notation

Assume that the substrate is described by the basis vectors  $\vec{a}_1$  and  $\vec{a}_2$ . The new basis vectors describing the surface structure are then  $\vec{b}_1$  and  $\vec{b}_2$ . In Woods notation this is described as S-Ni(100)  $(\vec{b}_1/\vec{a}_1 \times \vec{b}_2/\vec{a}_2)R\theta^\circ$  telling us that it is a  $2 \times 2$  structure of sulphur on Ni(100) rotated  $\theta$  degrees. Woods notation is quite convenient, but cannot be used to describe all LEED structures. When the angle between the new basis vectors in real space is changed with respect to the angle between the substrate vectors the notation is no longer valid and we must use the matrix notation which is always valid.

### The Matrix Notation

The substrate is in real space represented by a matrix:

$$\mathbf{A} = \begin{pmatrix} a_{11} & a_{12} \\ a_{21} & a_{22} \end{pmatrix} \quad (9.35)$$

Similarly the new basis set can be described by the matrix:

$$\mathbf{B} = \begin{pmatrix} b_{11} & b_{12} \\ b_{21} & b_{22} \end{pmatrix} \quad (9.36)$$

We can now find the matrix  $\mathbf{G}$  which maps  $\mathbf{A}$  on  $\mathbf{B}$

$$\mathbf{B} = \mathbf{G}\mathbf{A} \quad (9.37)$$

which is the one used in matrix notation i.e. S-Ni(100)  $\begin{pmatrix} g_{11} & g_{12} \\ g_{21} & g_{22} \end{pmatrix}$ , which in this specific case gives S-Ni(100)  $\begin{pmatrix} 2 & 0 \\ 0 & 2 \end{pmatrix}$ . Please note that the same set of equations also applies for the reciprocal set of vectors i.e.

$$\mathbf{B}^* = \mathbf{G}^* \mathbf{A}^* \quad (9.38)$$

In many cases it is convenient to determine  $\mathbf{G}^*$  from the LEED pattern and then find  $\vec{b}_1$  and  $\vec{b}_2$  in terms of  $\vec{a}_1$  and  $\vec{a}_2$  by the relation

$$\mathbf{G} = ((\mathbf{G}^*)^T)^{-1} \quad (9.39)$$

The area of the new unit cell is conveniently found as  $\det(\mathbf{G})$ .

The various types of overlayer structures can be classified by  $\mathbf{G}$ , but that is beyond the scope of these notes and we will refer to for example [5, 8] for details.

### Other Examples

Now we have the machinery ready for investigating surface structures. If we reconsider the structure above with sulphur on Ni(100) and add another quarter of a monolayer the center positions will also be occupied. The first LEED structure is often called a  $p(2 \times 2)$  structure while the second is called a  $c(2 \times 2) - p$  for primitive  $2 \times 2$  and  $c$  for centred  $2 \times 2$ . The correct notation for the latter is in Woods notation S-Ni(100) $(\sqrt{2} \times \sqrt{2})R45^\circ$  or in the matrix notation S-Ni(100)  $\begin{pmatrix} 1 & 1 \\ -1 & 1 \end{pmatrix}$ , since this cell is smaller than the  $2 \times 2$ . In the above examples the adsorbate lattice automatically also included the

substrate lattice. Let us now look at an example where we need to look for a coincidence cell as mentioned earlier. Consider a Ni(110) surface and the respective LEED structure when oxygen is added as shown in Figure 9.12.

**Figure 9.12** Schematic model of the real space model and the respective LEED patterns for the substrate, the overlayer, and the coincidence cell for oxygen on Ni(110).

Let us assume that  $2/3$  of a monolayer oxygen has been adsorbed and that the oxygen is sitting in two non-equivalent positions. The LEED pattern from the substrate is indicated as dots. The LEED pattern from the oxygen overlayer is indicated as triangles, whereas the spots occurring from the coincidence cell is shown as open squares. Please note that the correct LEED pattern is not just the sum of the substrate and the overlayer diffraction pattern, but that the coincidence cell which describes both at the same time must be found in order to determine the correct pattern.

The LEED pattern only gives us the size and orientation of the new unit cell formed by the substrate and the adsorbate together. It is not possible to say anything about the actual binding site or coverage of the adsorbate from the LEED pattern alone. (The adsorbate layer can be shifted in the unit cell of the substrate without any consequence for the resulting LEED pattern.) This must be determined from other experiments such as XPS and AES concerning the coverage and HREELS, STM and UPS concerning the actual binding site.

### 9.2.5 Domains

**Figure 9.13** Schematic model of the real space model for two different domains of  $4 \times 1$  structure on Ni(100). The respective LEED pattern shows the result of both types of domains present on the surface.

Yet another effect may complicate the analysis of LEED patterns namely *domains*. Remember that in a typical LEED experiment the electron beam



probes an area of a diameter of 0.1 mm to 1.0 mm and that if we just have islands which are larger than the transfer width then we will obtain nice LEED patterns from these islands (the intensity naturally being proportional to the coverage of these islands). Due to the surface symmetry these islands may differ in orientation. Consider for example a simple  $4 \times 1$  structure on Ni(100) as shown in Figure 9.13. When this structure nucleate there will be two equal possibilities of orienting the island on a (100) surface. As we will be sampling over many islands that are randomly oriented in two-dimensions the resulting LEED pattern will simply be the sum of the LEED patterns for each type domain.

In some cases for instance if the temperature is kept low there will not be any high mobility on the surface and there will be many small domains resulting in broadening of the spots since the number of scatters in each island are too low. This occurs if there are many small domains that are out of phase. If the different domains are in phase a sharp LEED pattern is still

obtained. See figure 9.16 for an example.

**Figure 9.14** Schematic model of the real space model for two 2x2 domains in phase and out of phase on a Ni(100) surface. Please note that in the out of phase mode the half order spots broadens if the domains are small enough.

### 9.3 Dynamical Scattering and IV-Curves

Strong oscillations appears in the intensity versus the primary energy of the electrons due to the multiple scattering in the different layers. The resulting curves are called IV-curves as shown in Figure 9.15. The modulation are due to Bragg reflections into the crystal, but as the intensity into the bulk is exponentially damped and thus only few layers contribute to this effect the modulation will be rather broad and the intensity will never go to zero com-

pletely. By performing very detailed analysis of the electrons scattered in the surface and calculate the resulting beam intensity for a number of different beams as a function of energy it is possible to compare to the experimental measured IV curves.

**Figure 9.15** The IV curve for Ni(100) at normal incidence.

In this manner it is possible to obtain models which gives the best fit to the data and obtain not only information on the two-dimensional structure in the surface but also the in depth distances between the different layers. In this manner it is for example possible to show that a clean surface introduces an inward relaxation of the first layer towards the second while the second layer usually expands compared to the bulk lattice distances. The relaxations are typically  $-5\%$  to  $10\%$  for the first layer and  $1\%$  to  $3\%$  for the second layer. These relaxations are easily explained in terms of EMT. The outermost atoms are less coordinated and are therefore missing electron density. They

can compensate for this and obtain the optimum electron density by shifting slightly towards the atoms below leading to the contraction. This on the other hand leads to a too high electron density for the atoms in the second layer which then expands to compensate, resulting in the so called Friedel oscillations which are exponentially damped into the material. Similarly detailed models can be constructed for adsorbate system and the distances can be extracted being the source of many accurate determinations of surface structures, see [2]. Unfortunately this scheme only works for relative simple structures since the number of fitting parameter describing the IV-curves are becoming too large for big unit cells like for instance a  $\sqrt{19} \times \sqrt{19}$ .



# Chapter 10

## Microscopy

When investigating materials and specifically catalysts it is always of interest to get an impression of the three dimensional structure of the sample. This may be obtained through a strongly magnified picture of the material. Usually the conventional light microscopes are not supplying much help if we are going for the finer details such as nano-particles since their resolution is limited by the wave length of the visible light to around  $1\text{ }\mu\text{m}$ . Thus if want nanometer or even atomic resolution we must turn to electron microscopes and Scanning Tunnelling Microscopes (STM). We have already in connection with scanning Auger seen that a scanning electron beam can make an excellent picture of the three dimensional structure. This can be improved considerably by using several different methods for detection and by using much higher electron energies (200 keV to 300 keV) as it is done in dedicated electron microscopes. The ultimate resolution of electron microscopes allows a point resolution of about  $1\text{ }\text{\AA}$ , sufficient for atomic resolution. The resolution is strongly dependent on the nature of the sample and it is in general not surface sensitive. The main emphasis here will, however, be put on the relative new STM method. Compared to EM it is much less generally applicable, but on the other hand it offers a much more detailed view of the surface structure and dynamics, which have not been within reach before. The resolution in STM is extremely good, less than  $0.1\text{ }\text{\AA}$ , but in general it requires very flat and well defined surfaces and is therefore in reality only applicable for model systems.

## 10.1 The Scanning Probe Methods

The idea of scanning probe microscopes is quite simple and now exists in several versions of which the most prominent are the STMs and Atomic Force Microscopes (AFM). The STM method was at first developed by Binnig and Rohrer [53, 54, 55] (who got the Nobel prize for their invention) and this is also the most mature of the scanning probe methods (see also [56]). A sharp tip (curvature on the order of  $100 \text{ \AA}$ ) is brought close to a surface and a low potential difference (the bias voltage) is put between the sample and the tip. Classically there should not be a current between the sample and tip, but as the distance gets small ( $5 \text{ \AA}$  to  $10 \text{ \AA}$ ) quantum mechanics take over and the electron can now tunnel through the barrier. This leads to a current which can be measured and is typically set to be around  $1 \text{ nA}$ . The experimental set-up is shown schematically in Figure 10.1

**Figure 10.1** Schematic drawing of the STM setup.

The experiment can be performed in several modes i.e. constant current or constant distance while scanning the tip over a desired surface area. The constant current mode is the most common. Here the current is kept constant by varying the tip-surface distance in a feedback loop. The tip is mounted on a piezoelectric tube which can expand or contract depending on the potential difference. Similarly the scanning in the  $x$  and  $y$  directions is obtained by applying potential differences on a tube that is split in four parts. The coarse approach of the tip to the surface is taken care of by applying a so called inch worm also based on piezoelectric elements. The scanning in the  $x$  and  $y$  directions goes from the Å regime to a few  $\mu\text{m}$ . The inch worm allows the tip to be moved several mm per minute while the much more accurate  $z$  motion is taken care of by a tube that can expand or contract typically 1000 Å with a resolution of 0.01 Å! The whole arrangement is kept small to obtain high resonance frequencies and mounted on a set-up which negates external disturbances. For obtaining a typical STM picture the tip is scanning 256 lines measuring 256 points in each line. The scan rate is very fast and it takes between 1 and 10 seconds to obtain a picture. By acquiring subsequent pictures it is possible to make movies of dynamical processes on the surface such as diffusion and chemical reactions. Usually a tungsten tip is used. There are good recipes for preparing sharp tips which is necessary if the surfaces are not flat, but blunt tips prepared just by cutting a tungsten wire with pliers may also work since as long as just one atom is sticking further out than the rest this will conduct all the current as we shall see later. The disadvantage of STM is that it unfortunately only works on reasonable well defined flat conducting surfaces.

The other scanning probe microscopy method that should be mentioned in this context is AFM. The set-up is in many ways similar to STM, although here the tip is mounted on a cantilever which is just a spring. When the tip is brought close to the surface there will be van der Waals interactions due to coulomb interactions of quantum fluctuations in the tip and substrate. This interaction sets up a potential and the tip will first feel a force when it approaches the surface. This force can be measured by measuring how much the cantilever (spring) is deflected knowing the force constant. The forces involved are extremely weak (nN) and very sensitive methods must be used to measure how much the cantilever is deflected. This is typically done by shining laser light on the cantilever which is reflected into a position sensitive detector so the motion up and down can be measured. The whole arrangement is again mounted on a piezoelectric scanner so it can be scanned



over the desired area. In this manner it is possible to get atomic resolution on flat samples, or determining the surface morphology on a larger scale. The advantage of this method is that it does not require a substrate that is conducting meaning that it can be used on real catalyst samples where the support material often is an oxide. The drawback is that the shape of the tip, as for STM, put rather strong restrictions on the resolution and the topography that can be depicted. Like STM the method does not give any information about the composition of the surface so this information must be obtained by using complementary methods like XPS. The AFM method still undergoes strong development and may be improved considerably in the future.

In the following we will concentrate on the STM since this is the superior method and where the most interesting research is performed at the moment.

### 10.1.1 Theory of STM

A relatively simple and adequate theory for the tunnelling effect seen in STM was presented by Tersoff and Haman [57]. Here we will only give a brief review of the involved theory and derive an expression for the essential tunnelling current. The experiment is shown schematically in Figure 10.2 where the energy levels of the electron in the tip and the sample are illustrated. Both are assumed to be free electron metals with monotone density of states (DOS) around the Fermi level and work function  $\phi_\mu$  for the tip and  $\phi_\nu$  for the crystal. Figure 10.2 a illustrates the situation when the distance

between tip and surface is large.

**Figure 10.2** Schematic drawing of the surface potential of the crystal and the tip.

The distance in Figure 10.2b is now reduced to  $d$  and the tip is biased negatively with a few mV with respect to the crystal. The potential for the electrons is reduced to a potential barrier with an average height of  $\phi = \frac{\phi_\mu + \phi_\nu}{2}$  and as the wave functions for the electrons do not decay completely to zero they may tunnel through the barrier. The expression for the tunnel current is in 1st order perturbation theory given by:

$$I = \frac{2\pi|e|}{\hbar} \sum_{\mu\nu} (f(E_\mu)(1 - F(E_\nu))) |M_{\mu\nu}| \delta(E_\mu + |e|V - E_\nu) \quad (10.1)$$

where  $E_\mu$  and  $E_\nu$  are the energy relative to the Fermi level  $E_F$  and

$$f(E) = \frac{1}{e^{\frac{(E - E_F)}{k_B T}} + 1} \quad (10.2)$$

is the Fermi function giving the occupation as a function of  $E$ .  $V$  is the applied voltage difference and if  $V|e| \simeq 0$  and  $T \rightarrow 0$  then  $f(E_\mu) \simeq 1$  for  $E_\mu < 0$  and  $f(E_\nu) \simeq 0$  for  $E_\nu > 0$ , thus electrons are tunnelling from full states in the tip into the empty conduction states above the Fermi level of the crystal. The delta function ensures energy conservation, i.e. it is assumed that the electrons do not undergo energy losses during the mechanism. This assumption is easily seen to be fulfilled by considering that typical bias voltages are on the order of 10 mV and the universal curve discussed earlier. This will be truly ballistic electrons moving far into the crystal before undergoing energy losses. Using  $V \simeq 0$  and the other approximations we get

$$I = \frac{2\pi e^2 V}{\hbar} \sum_{\mu\nu} |M_{\mu\nu}| \delta(E_\mu - E_F) \delta(E_\nu - E_F) \quad (10.3)$$

The essential problem of calculating the tunnelling matrix element  $M_{\mu\nu}$  was solved by Bardeen [58] giving

$$M_{\mu\nu} = -\frac{\hbar^2}{2m} \int (\Psi_\nu^\dagger \nabla \Psi_\mu - \Psi_\mu \nabla \Psi_\nu^\dagger) d\vec{S} \quad (10.4)$$

Remembering that  $i\hbar\nabla$  is the momentum operator it is seen that this integral evaluates the flux of electrons through a surface  $S$  lying in the vacuum region.

In order to get any further we must introduce the appropriate wave functions. The wave functions at the surface of the crystal are straightforwardly described by the two-dimensional Bloch expansion as:

$$\Psi_\nu(\vec{r}_\parallel, z) = \frac{1}{\sqrt{\Omega}} \sum_G a_G e^{i\kappa_G \vec{r}_\parallel} e^{-z\sqrt{\kappa^2 + \kappa_G^2}} \quad (10.5)$$

where  $G$  is a surface reciprocal lattice vector,  $\Omega$  is a normalisation volume, and  $\kappa$  is the decay constant of the surface wave into the vacuum region.  $\kappa$  is given by

$$\kappa = \sqrt{\frac{2m\phi}{\hbar^2}} \quad (10.6)$$

Thus the surface wave function is just an expansion on plane Bloch waves that are exponentially damped out in the vacuum region with the potential  $\Phi$  as indicated in Figure 10.2. The evaluation of the tip wave functions  $\Psi_\mu$  is much more difficult since its structure is not known in detail. One way to approach this problem is to assume that the end of the tip can be approximated by a sphere with radius  $R$  centred at position  $\vec{r}_0$  as indicated in Figure 10.3. Then the tip waves can be approximated by s-waves of the type

$$\psi_\mu = \frac{1}{\sqrt{\Omega_t}} c_t \kappa R e^{\kappa R} \frac{e^{-\kappa|r-r_0|}}{\kappa|r-r_0|} \quad (10.7)$$

where  $\Omega_t$  is the normalisation volume and  $c_t$  is a normalisation constant.

**Figure 10.3** Schematic drawing of the tunneling geometry.

The matrix element can now be calculated leading to

$$M_{\nu\mu} = \frac{1}{\sqrt{\Omega_t}} \frac{4\pi\hbar^2}{2m} R e^{\kappa R} \Psi_\nu(\vec{r}_0) \quad (10.8)$$

inserting this in the equation for the current  $I$  we get

$$I = \frac{8\pi\hbar^3 e^2 R^2 V}{m} e^{\kappa R} D_t(E_F) \rho(\vec{r}_0, E_f) \quad (10.9)$$

where  $D_t = \frac{1}{\Omega_t} \sum_{\mu} \delta(E_{\mu} - E)$  is the density of states per volume of the tip and

$$\rho(\vec{r}, E_f) = \sum_{\nu} |\Psi_{\nu}|^2 \delta(E_{\nu} - E) \quad (10.10)$$

is the local density of states at the crystal. The surface wave functions are exponentially damped out in vacuum where there is a mean potential  $\Phi$  resulting in

$$|\Psi_{\mu}|^2 \propto e^{-2\kappa z} \quad (10.11)$$

leading to the final equation

$$I \propto e^{-2\kappa z} = e^{-1.025 \sqrt{\Phi(\text{eV})} z(\text{\AA})} \quad (10.12)$$

The main result is that the current is exponentially dependent on the distance between the tip and the surface, mainly because the overlap between the empty and filled wave is dependent on the tails of the wave function out in the vacuum region. This explains why it is not extremely difficult to get a good and localised tip. Consider one atom on the tip that sticks out with just 1 Å compared to the rest, then it will carry 90 % of the current. This also explains why it is possible to obtain atomic resolution in STM. Finally it should be mentioned that for fixed tip conditions we will probe the density of states (either empty if the tip is negatively biased or filled states if the tip is positively biased) of the crystal just below the tip. Thus what is depicted in an STM experiment is **not** the atoms but the density of states around the Fermi level. That this density varies around the atoms leading to the observed corrugation is not a surprise.

The above model involved many approximations and assumptions, nevertheless, it captures the most important features of the STM experiment. Naturally there are regions where this picture will break down due to its simplicity. If for example the tip surface distance is getting very small the potential barrier will not be a simple average any longer and eventually there will be formed a contact. This contact can consist of a single atom and it is then seen how the conductance becomes quantised. This is an interesting

phenomenon but beyond the scope of these notes. Also if the current is getting very high this simple picture will break down since we have completely neglected the interaction between the tunnelling electrons. Thus care must be exercised.

### 10.1.2 Results from the Yellium Model

In order to elucidate how adsorbates will be depicted in STM N. Lang [59] undertook a number of investigations using a simple model system. The tip was modelled by a Na atom adsorbed on a high electron density metal which can be described by the so called yellium model. Here the positive charge from the nuclei are smeared out and the free electron gas is solved on this positive background. One advantage of such models is that it is relatively easy to map out the difference in eigenstate density introduced by adding an adsorbate to the yellium. Figure 10.4 shows such differences when Mo, Na and S is adsorbed on a yellium. The calculation is only shown for  $m = 0$  component of the wavefunctions since it is these states that are mainly responsible for the tunnelling current. The figure shows that Na introduces a resonance above the Fermi level while S introduces one below and all three components result in additional charge density at the Fermi level.

Using this set-up and positioning the "tip" i.e. the yellium with an adsorbed Na atom in front of another yellium it was shown that the current density was indeed localised to the Na atom as shown in Figure 10.5. The largest current density arrow is a factor of 25 bigger than the smallest current density  $j_0$ . The length and the thickness of the current arrows are propor-

tional to  $1 + \ln(j/j_0)$ .

**Figure 10.4** Difference in eigenstate density between the yllium-adsorbate system and the clean yllium for different adsorbates as indicated, taken from [59]

**Figure 10.5** Current density for a “tip” consisting of a Na atom adsorbed on a Yellium positioned in front of a clean yellium surface. The length and thickness of the arrows are proportional to  $1 + \ln(j/j_0)$ . Taken from [59]

If this “tip” is now used to scan over another yellium where adsorbates like Na, S and He have been adsorbed it is possible to estimate how much the tip have to be displaced vertically in order to keep the current constant when a small bias voltage is applied. This is depicted in Figure 10.6 showing that Na will appear as a much larger protrusion than S while He will be depicted as a depression in the yellium. This is in good agreement with Figure 10.4 showing that Na introduces a much higher electron density at the Fermi level than S does and since the tunnelling current was proportional to the density of states at the Fermi level it will lead to a larger retraction of the tip in the Na case. The He will naturally not adsorb at all, but will, due to the Pauli principle, exclude the electron leading to a lowering of density of states with



respect to the clean surface.

**Figure 10.6** Displacement of the “tip” in the constant current mode for Na, S, and He adsorbed on yllium, taken from [59]

The important thing to be learned from this, is that adsorbates may not necessarily be depicted as protrusions, although they are geometrically. It all depends on the effective charge density at the Fermi level and it is well known that adsorbates like carbon, nitrogen, and oxygen all are depicted as holes, since they are relatively electronegative and removes charge density from the Fermi level. This also shows that we must know what sort of adsorbates we are dealing with i.e. the experiment must be conducted under well defined conditions.

## 10.2 Spectroscopy

In all the considerations above the bias voltage was kept low so only the states around the Fermi level participated in the tunnelling phenomenon. If we now changed this condition and used higher potentials  $V$  the tunnelling current will be dependent on the density of states at higher energy levels, making it possible to map out the DOS below and above the Fermi level

doing spectroscopy. The current can be approximated by

$$I \propto \int_{E_F}^{E_F + |e|V} \rho_\nu(\vec{r}_0, E) \rho_\mu(E - \dim e \dim V) dE \quad (10.13)$$

where  $\rho_\mu$  is the total density of states of the tip and  $\rho_\nu$  is the local density of the sample. The  $\rho_\nu$  can be approximated by a product of the density at the surface times a penetration factor out into the forbidden vacuum region as:

$$\rho_\nu(\vec{r}_0, E) \sim \rho_\nu(E) e^{-\frac{2d\sqrt{2m(W - E + \frac{1}{2})|e|V}}{\hbar}} \quad (10.14)$$

where  $W$  is the height of the potential barrier. This is intuitively easy to understand. The lower the energy  $E$  the broader and higher the barrier will be and the current will therefore be dampened exponentially. If we want to isolate  $\rho_\nu(E)$  we must clean it from the influence of the penetration factor and  $\rho_\mu$ . By measuring relations between  $I$  and  $V$  for a fixed distance and by plotting  $(dI/dV)/(I/V)$  any sharp feature in the surface (or tip) density of states will become apparent. An example was given by Lang shown in Figure 10.7 where the Na "tip" was used on a Ca atom adsorbed on yllium. The left panel shows the difference in density of states for the two adsorbates and the left panel shows the resulting  $(dI/dV)/(I/V)$  analysis. Only broad features are in general observed for metals so this method is, like UPS, useless

for elemental analysis.

**Figure 10.7** Left the introduced difference in density of states by adsorbing Na and Ca on yllium. Right the resulting  $(dI/dV)/(I/V)$  analysis, taken from [59]

It is worth noticing that if we look at S adsorbed on the yllium we see that the appearance in an STM experiment will depend very much on the bias potential, since it, as shown in Figure 10.8, leads to a reduced density of states at high voltages. Thus, as indicated in Figure 10.8, the S atom will appear as a protrusion for voltages below 1 V, will vanish around 1.3 V and become a depression for higher voltages. Thus the picture obtainable will be very dependent on the chosen bias voltage. This is in particular illustrated in semiconductors where there is a bandgap and dangling bond pairs to form occupied bonding states and empty anti bonding states at the surface. By making  $(dI/dV)/(I/V)$  analysis the various states can be found for a constant distance and by scanning at well chosen voltages the different

orbitals can be mapped out on the surface.

**Figure 10.8** Left the introduced difference in density of states by adsorbing Na and S on yllium. Right the vertical displacement of the “tip” over the S atom as a function of bias voltage, taken from [59]

In the above we have assumed that the tip behaves like a metal. Not much is in reality known for sure about the states of the tip and the ad atom actually conducting the current. Sometimes the tip changes in the middle of a scan and what earlier appeared as protrusions may suddenly in the middle of a frame be depicted as depressions or vice versa. Such sudden and unexplained changes are often interpreted as tip changes, where the tip for example is picking up an atom from the surface changing its nature.

## 10.3 Examples of STM Investigations

STM has had a very strong impact on the field of surface science and STM have to some extent also revolutionised the structural investigation. Still, it is not a trivial method to use like LEED where it is possible to obtain a LEED pattern within than half an hour if the surface is well ordered. It can be somewhat tricky to prepare the tip so that high resolution pictures can be obtained. Sometimes, the STM is working immediately, other times one may spend a day at the microscope and only occasionally see a structure. It is particularly difficult to obtain atomic resolution on metal surfaces since the corrugation here usually is less than  $0.1 \text{ \AA}$ .

The STM and LEED methods complement each other in the sense that LEED rather quickly gives an idea of the overall order on the surface, but not much information on the atomic level if that is not ordered. Luckily STM works very well at this level. In principle STM does not require any order on the surface meaning that domain boundaries and positions of single atoms can be investigated in great detail. So in principle the STM is much more versatile, although it should be remembered that just because we see an interesting structure within an area of  $100 \times 100 \text{ \AA}^2$ , it is not necessarily representative for the rest of the surface. Therefore several areas must be investigated before any conclusions can be drawn. In the following we will give a few examples on the use of STM.

### 10.3.1 Surface Structure

Acquiring an STM picture of a surface structure actually provides us with a real space picture of the surface topography, although care should be exercised, since it is the electron density at the Fermi level we are mapping out. Atoms that sticks out from the surface may not necessarily become depicted as protrusions. Usually it is possible to recognise the unit cell although that does not provide a solution to the structure. An example is shown in Figure 10.9 where the STM pictures and the LEED pattern of the S-Cu(100) ( $\sqrt{17} \times \sqrt{17}$ ) $R14^\circ$  is shown.

Although it is known from AES studies that this surface contains eight sulphur atoms per unit cell only four of them can be identified as protrusions in the STM picture. The corresponding LEED pattern is quite complex as there are two domains. A model based on the STM picture have been

proposed and is shown in Figure 10.10.

**Figure 10.9** STM and LEED picture of the S-Cu(100) ( $\sqrt{17} \times \sqrt{17}$ )R14°

structure, taken from [60]

**Figure 10.10** A schematic model of the S-Cu(100) ( $\sqrt{17} \times \sqrt{17}$ )R14° structure with 8 sulphur atoms per unit cell, taken from [60]

Sometimes it is possible to observe both regions of the clean metal and regions covered with an adsorbate so it is possible to extend the metal lattice into the adsorbate structure. This is demonstrated in Figure 10.11 taken from Besenbacher *et al.* [61] where the STM picture of the Cu(110) and the

missing O-Cu(110)  $(2 \times 1)$  row are shown.

### Figure 10.11

Also by detailed analysis of the surface as a function of adsorbate dose it is possible to estimate how much of the substrate is being build into a new structure by following the mass transport of the substrate, i.e. following the development of steps and holes made in the crystal as a function of dose. By making movies of the oxidation of Cu(110) it was for example possible to suggest a structure for the high coverage structure O-Cu(110)  $c(6 \times 2)$  which, quite surprisingly, showed that Cu atoms were sitting highly uncoordinated on top of the previously formed missing row reconstructions as shown in Figure 10.12 [61]. A structure where the unit cell is very difficult to solve in



the conventional LEED-IV analysis.

**Figure 10.12**

### **10.3.2 Two-Dimensional Alloys and Overlayers**

Since there is no help to be found from spectroscopic analysis for distinguishing two metals from each other it can be a difficult task to investigate metal overlayers and alloy formations. But again if the development of the surface can be followed as a function of deposition time, changes can be related to the amount of metal added. It is in this manner possible to study growth and diffusion mechanisms even on homo epitaxial systems like Pt deposited on a Pt single crystal. Earlier, the growth mechanisms on surfaces were classified into three modes as mentioned in Chapter 6 (Frank-van der Merwe, Stranski-Krastanov and Volmer-Weber growth modes). However, the STM

have shown that that was a much too simplified picture and that there is many other complex ways the growth process may proceed. Also alloy formation can be investigated and it was recently shown by use of STM that even metals which are known to be immiscible can form two-dimensional alloys in the surface. It has now been found to be a quite common phenomenon [62] and we shall here describe one of the first systems that was found.

If Au is deposited on Ni(111) it was expected that the Au would grow epitaxially on the Ni surface because the system was known to be immiscible and the surface energy of Au is significantly smaller than Ni. Thus it was surprising when STM pictures, like the one shown in Figure 10.13, were measured [63]. Since the coverage of the black holes increased with increasing Au dose these were identified as being due to gold. At the same time some very bright atoms also appeared and it turned out to be Ni atoms pressed out from the surface by the gold. Thus a two-dimensional nearly random surface alloy was being formed in this case. Actually the Au atoms have been calculated to protrude by about a quarter of an Å from the Ni surface, but again due to the electron density around the Fermi level they appear like depressions in the Ni lattice. This two-dimensional surface structure proved to be a very good way to control the reactivity of Ni particles and a catalyst

was later developed on that basis [64].

### Figure 10.13

The Co-Cu(111) system is an example of studying overlayers on the surface. Again the structures that was found when depositing Co at room temperature were not simple islands in the submonolayer regime. Instead, two layer high islands were found surrounded by a single layer high island. By adsorbing CO it was possible to identify, that the central island consisted of Co while the surrounding island consisted of Cu. An STM picture of CO on Co/Cu(111) at room temperature is shown in Figure 10.14 taken from [65]. CO was only adsorbed on Co sites at this temperature, and the  $(\sqrt{3} \times \sqrt{3})R30^\circ$  of CO on Co can be recognized in the top layer [65]. Around the apparent double layered Co island there is a Cu brim which with time

will become double layered at room temperature.

### Figure 10.14

Based on such STM pictures with atomic resolution, a model was proposed which is schematically illustrated in Figure 10.15. Thus co-adsorption of for example CO made it possible to distinguish the Co from Cu. It should in this context be mentioned that it is usually very difficult to obtain pictures of CO adsorbed on surfaces, since this species diffuse very fast compared to the time scale of the STM experiment. Only in the saturation coverage regime the CO structure will freeze out and pictures like the one shown in

Figure 10.14 are obtainable.

**Figure 10.15**

### 10.3.3 Dynamics and Chemical Reactions

By acquiring sequences of pictures it is possible to follow the dynamics on the surface if the processes are taking place on the same time scale as the measurements. This is mainly a matter of being able to control the temperature of the sample while scanning. Unfortunately, that is not a trivial problem, since the sample must be isolated from vibrations and any temperature difference may lead to thermal drift in the system. Nevertheless, there is a strong development in the field and there have recently been many studies both below and above room temperature.

Diffusion of ad atoms or adsorbates can for example be studied and by

following their two-dimensional movement the diffusion constant can be extracted. Also regular chemical reactions may be followed. One example is the oxidation of methanol on the O-Cu(110) ( $2 \times 1$ ) structure where it has been shown that the reaction is very anisotropic and only takes place at the rim of the oxygen islands. This implies that at that particular temperature the mean field approximation is not valid. Such experiments require long time stability of the STM and surprisingly few good investigations have actually been performed. This is also an area of development, since there is a strong demand for being able to run the STM not only at elevated temperatures but also at elevated pressures from the catalysis community. Any STM can run under ambient conditions, but the challenge is to get it running in atmospheres relevant to catalysis and study reactions at the surface. There have been attempts to obtain STM images of real catalysts, but so far it has not been very successful. It is very difficult to orient yourself on such non-ideal surfaces and find the active metal particles. Furthermore there is also the problem of the isolating the support material.

## 10.4 Electron Microscopy

Electron Microscopy is widely used giving us a visual impression of materials or biological samples in the regime where the light microscopes does not work any longer. Considering the universal curve it is obvious that these 100 keV to 400 keV electrons will penetrate their way into the sample and the method is as such not a surface sensitive method, although it can be if combined with for example an Auger analyser. There are many ways to detect the electrons used in EM as shown in Figure 10.16 taken from [4] and each of the methods

add complementary information on the sample investigated.

### **Figure 10.16**

The transmitted (TEM) or reflected (SEM) electrons may in the scanning mode be used for depicting the sample morphology. By measuring emitted x-rays (EDS), emitted electrons (Auger), or by measuring energy losses it is possible to make elemental identifications. The electrons may undergo diffraction, if there are favourably oriented crystalline particles so also crystallographic information may be obtained. An example of a transmission electron micrograph, stimulating our imagination of a catalyst, is shown in

Figure 10.17 where small Rh particles are supported on a silica sphere [66].

### Figure 10.17

Another example is the highly undesired growth of carbon on Ni-catalyst as shown in Figure 10.18. Here it is seen how the carbon filaments grow out



from the Ni-particles basically ruining the catalyst, taken from [67].

### Figure 10.18

EM microscopes usually come in the conventional high vacuum regime ( $10^{-6}$  mbar to  $10^{-7}$  mbar) or in the UHV version ( $10^{-10}$  mbar). But recent development have made it possible to study samples under reasonable pressures (mbar regime) so catalysts can be studied under somewhat more realistic conditions following for example the dynamics as a function of gas composition. Care must naturally be taken here since an 300 keV beam is not exactly innocent concerning introducing chemical reactions, that would not otherwise have been possible.

# Chapter 11

## Ion Scattering Methods

There are a wide number of other important methods in surface science and it is beyond the scope of these notes to treat them all. Nevertheless the ion scattering methods deserve to be mentioned briefly since they are used widely and will be encountered quite often in the literature.

Previously we have seen how heavy ions like Ar could be used to remove atoms from the surface and how that combined with an analytical method like AES could be utilised to get information from deeper lying layers. In the following section we shall see how primarily light ions such as  $\text{H}^+$  or  $\text{He}^+$  can be used to actually identify various elements at the surface (Ion Scattering Spectroscopy), and also how they in the high energy version can be used to make a non-destructive depth profile. Both methods come in more advanced version where also surface geometry can be investigated and serve as tool for structural investigations like LEED.

### 11.1 Low Energy Ion Scattering Spectroscopy

The principle of Low Energy Ion Scattering (LEIS) or just Ion Scattering Spectroscopy (ISS) is very simple and can be performed in many UHV chambers in its basic version. All that is required is an ion gun and a bipolar analyser so that the energy of positive ions instead of electrons can be measured in an angle resolved manner. Naturally the set-up can be more advanced by having a well focused ion source so that lateral resolution can be obtained or with a movable analyser so that the ions can be detected in various scattering geometries. In the following we will only consider the simple version where

the angle between the analyser and the ion gun is fixed. The geometry is depicted in Figure 1.

**Figure 11.1** Schematic drawing of the ISS setup.

**Figure 11.2** Calculated  $\text{He}^+$  ion trajectories as a function of impact param-

eter. The energy of the He beam was 1 keV and the target atom is Yb.

ISS usually refers to primary energies of 1 keV to 2 keV energy of the ions. Preferentially He is used although heavier ions like Ne are also encountered. Very low ion doses are used in order not to create too much damage on the surface by sputtering processes. This is also one of the reasons for using lighter He ions. In this low energy regime the ions interact almost perfectly through binary collisions with the surface atoms. The method is very surface sensitive since it has a large scattering cross section  $\sim \text{\AA}^2$  and thereby a large shadow cone see Figure 2 ensuring that most ions are not passing through the first layer of the sample. Furthermore most of the ions hitting the surface will be neutralised ( $> 99\%$ ) so very few of the particles survive the interaction as ions.

This makes the method particularly surface sensitive since ions which penetrates into the surface or undergoes multiple scattering processes will be neutralised and not detected in the electrostatic analyser if they were to be scattered back. Since it is a simple binary collision there will be conservation of momentum and energy:

$$M_i v_0 = M_i v_1 + M_s v_s \quad (11.1)$$

and

$$\frac{1}{2} M_i v_0^2 = \frac{1}{2} M_i v_1^2 + \frac{1}{2} M_s v_s^2 \quad (11.2)$$

where  $M_i$  is the mass of the incoming ion,  $M_s$  is the mass of the surface atom,  $v_0$  is the velocity of the incoming ion,  $v_1$  is the velocity of the scattered ion, and  $v_s$  is the velocity of the surface atom after the interaction.

After appropriate manipulation of the above equations the following ratio between the velocities of the incoming and outgoing ion can be found:

$$\frac{v_1}{v_0} = \frac{\pm \sqrt{M_s^2 M_i^2 \sin^2(\theta)} + M_i \cos(\theta)}{M_s + M_i} \quad (11.3)$$

If the  $M_i < M_s$  the plus sign applies and the ratio between the energy of the incoming and outgoing ion is:

$$\frac{E_1}{E_0} = \left[ \frac{\sqrt{M_s^2 - M_i^2 \sin^2(\theta)} + M_i \cos(\theta)}{M_s + M_i} \right]^2 \quad (11.4)$$

The equation shows that the energy of the ion after the scattering event is only dependent on the initial energy of the ion, the angle  $\theta$  and the mass of the surface atom. Since only the latter is unknown the mass of the surface atom can be determined. A typical ISS spectrum is shown in Figure 3.

**Figure 11.3** Schematic drawing of the STM setup.

The big advantage of ISS is that it is basically restricted to probing the surface layer. Thus if say a 50-50 alloy is studied it is quite easily seen if one component segregates to the surface instead of the other one. The same results are in principle obtainable from an AES or XPS study, but here the deeper lying layers will always contribute as well which complicates the

analysis. The mass resolutions are typically not very good (depends naturally on geometry and resolution power of the analyser) and it is usually not possible to distinguish two neighbour elements such as nickel and copper unless special equipment and isotopically cleaned samples are used. In some specific cases the resolution between different elements can be improved considerably by for instance using  $\text{Ne}^+$  ions instead of  $\text{He}^+$  ions, but great care should here be exercised that the surface is not damaged by sputtering during the measurements.

In dedicated instruments it may be possible to make angle resolved measurements changing the angle of the analyser. By comparing such data to calculations of the absolute scattering cross section of the various atoms present on the surface and by making model calculations it is possible to extract information on the surface structure just as could be done by modelling LEED IV-curves. Such analysis is just as LEED restricted to well-behaved flat surfaces. Recently a dedicated instrument has been developed by [72] utilising the advantages of the geometry of a CMA. By having the ion gun along the center of the analyser, which is normal to the surface, and collecting scattered ions in a ring of the cylinder, a huge gain in signal can be obtained. This means that it first of all is very fast to perform an analysis and secondly only very small doses of ions are necessary limiting the potential danger of destruction of the surface.

## 11.2 High Energy Ion Scattering Spectroscopy

This method will only be treated briefly here since it is not a general method as it requires access to high energy accelerators. An extensive review of these methods can be found in [7]. In a typical Rutherford Backscattering Spectroscopy (RBS) experiment ions are used which have energies in the range of 0.5 MeV to 5 MeV.  $\text{H}^+$ ,  $\text{D}^+$  and  $\text{He}^{++}$  ions at these energies have a very small cross section for scattering and will therefore have a penetration depth of several  $\mu\text{m}$  into the material. By measuring the energy of the ions scattered back -  $\theta = 170^\circ$  - into a high energy ion detector it can in the same manner as for ISS be deduced which atoms the ion has encountered in the solid. The high energy ion detector is typically a gold coated silicon wafer where the ions during de-acceleration forms electron-hole pairs in the silicon in a number proportional to the energy of the incoming ion. Furthermore, as the ions will lose energy during penetration of the solid and since this energy

loss can be estimated quite accurate is it possible to estimate the distance the ions have penetrated in the sample. An example of an RBS is shown in Figure 4 where 3 MeV  $\text{He}^+$  ions are back scattered ( $\theta = 170^\circ$ ) from a 4000 Å thick aluminium film with gold overlayers on both sides. Notice that the position of the front of the peaks reveals the element and the width the thickness of the various elements. Gold shows two peaks since ions scattered from the gold film on the back side will lose energy penetrating the aluminium film twice. Thus RBS analysis can be a powerful tool in many cases where it is necessary to analyse sandwich structures or diffusion profiles.

**Figure 11.4** Schematic drawing of the STM setup.

## 11.3 Secondary Ion Mass Spectroscopy

Secondary Ion Mass Spectroscopy (SIMS) is a method very similar to ISS in the sense that also here low energy ions are used and the conventional UHV equipment will be sufficient. But instead of performing energy analysis of the back scattered ions a mass analysis of particles sputtered away from the surface is performed as illustrated in Figure 5. This allows for a detection of which elements, fractions of molecules, or clusters have been present on the surface. The method is very sensitive and can in some cases measure down to ppm levels of impurities in a sample. This makes the method particularly applicable in the microelectronic industry for characterizing for instance the silicon wafers for impurities and dopant.

**Figure 11.5** Schematic drawing of the SIMS setup.

Quantitative analysis is in general difficult in surface science, but it is a



particular problem in SIMS due to the fact that the method relies only on the ions coming off the surface. Ideally all species should be detected if a correct composition should be extracted. As we saw for the ISS experiments the chance of surviving as an ion was very little when interacting with the surface. Furthermore this probability will be very dependent on the element in question and the behaviour of the surface. In an approximate picture a simple relation can be obtained [73] where the probability for obtaining positive ions is given by

$$P^+ \propto e^{-\frac{\Phi - A}{\epsilon_0}} \quad (11.5)$$

where  $\Phi$  is the work function of the surface,  $A$  is the affinity level of the atom leaving the surface and  $\epsilon_0$  is a variable dependent, among other things, on the hopping matrix element of the electron from the atom to the surface and the velocity normal to the surface of the atom leaving. Similarly the probability for negative ions is given by

$$P^- \propto e^{-\frac{I - \Phi}{\epsilon_0}} \quad (11.6)$$

where  $I$  is the ionisation potential of the atom leaving the surface. It is now obvious why the probability for obtaining signal in SIMS will vary orders of magnitude for the different elements and why it is not possible to say anything about the surface composition from a spectrum without taking the sensitivities of the different elements into consideration. A SIMS spectrum of Si is shown in Figure 6 together with an AES analysis of the same surface. The SIMS analysis reveals many components which are not observed in the AES spectrum at all. That the probability also depends on the work function  $\Phi$  makes things even worse since that will tend to vary strongly with the

surface composition during a sputter profile.

**Figure 11.6** Schematic drawing of the STM setup.

The quantitative analysis can naturally be considerably improved by using well known standards and the method is particularly useful for measuring

trace amounts of elements where methods like XPS and AES have to give in due to their detection limit (roughly 1 atomic percent). SIMS can also be used for measuring bigger fragments sputter off the surface. For instance SIMS has in some special cases been used in catalysis to monitor whether certain intermediates may be present at the surface or not. Even bigger fragments can be analysed, but then a conventional quadrupole mass spectrometer may not be sufficient any longer. Instead a Time of Flight (TOF) technique is used. This approach is particular useful when analysing the fragments coming of polymer surfaces.

There are many interesting aspects to these ion based methods, but the reader is referred to Briggs and Seah for a thorough treatment [31] of this subject.

# Bibliography

- [1] A. Zangwill, “Physics at Surfaces”, Cambridge University Press, Cambridge (1988) ISBN 0-521-34752-1.
- [2] G. Somorjai, “Introduction to Surface Chemistry and Catalysis”, Wiley and Sons, New York (1994) ISBN 0-471-03192-5.
- [3] J. B. Hudson “Surface Science”, Wiley and Sons, New York (1998), ISBN 0-472-25239-5.
- [4] J. W. Niemantsverdriet, “Spectroscopy in Catalysis”, VCH, Weinheim (1995), ISBN 3-527-28726-4.
- [5] G. Ertl and J. Kupperts, “Low energy electrons and Surface Chemistry” VCH Weinheim (1985), ISBN 3-527-26056-0.
- [6] D. Briggs and M. P. Seah, “Practical Surface Analysis”, Wiley (1990) ISBN 0 471 92081 9.
- [7] L. Feldman and J. W. Mayer, “Fundamentals of Surface and Thin Film Analysis”, North-Holland (1986) ISBN 0 444 00989 2.
- [8] D. P. Woodruff and T. A. Delchar, “Modern techniques of surface science”, Cambridge University Press (1986) ISBN 0 521 35719 5.
- [9] A. Roth, “Vacuum Technology”, North Holland (1990), ISBN 0 444 86027 4.
- [10] R. P. Feynman, R. B. Leighton, and M. Sands, “The Feynman Lectures” Vol II. Addison-Wesley Publishing Company (1975).

- [11] K. Siegbahn, C. N. Nordling, K. Hamrin, J. Hedman, G. Johansson, T. Bergmark, S. E. Karlson, I. Lindgren, and B. Lindberg. "ESCA, Atomic, Molecular, and Solid State Structure Studied by Means of Electron Spectroscopy", Almqvist and Wiksells, Uppsala, Sweeden, (1967).
- [12] Krause and Ferreria, (1975).
- [13] I. Chorkendorff, J. Onsgaard, J. Schmidt-May, and R. Nyholm, Surf. Sci. 160 (1985) 587.
- [14] F. Gerken, PhD Thesis, HASYLAB, Hamburg, Germany, (1982).
- [15] D. A. Shirley, Topics in Applied Physics, 27, (19xx).
- [16] G. K. Wertheim and L. R. Walker, J. Phys. F: Metal Phys, 6 (1976) 2297.
- [17] S. Doniach and M. Sunjic, J. Phys. C: Solid St. Phys, 3 (1970) 285.
- [18] C. D. Wagner, W. M. Riggs, L. E. Davis, J. F. Moulder, and G. E. Muilenberg, "Handbook of X-ray Photoelectron Spectroscopy", Perkin-Elmer Corporation.
- [19] P. K. Ghosh, "Introduction to Photoelectron and Auger Spectroscopy", Wiley-Interscience Publishers, New York, (1983).
- [20] J. H. Scofield, J. Electron Spectrosc. 8 (1976) 129.
- [21] I. Chorkendorff, I. Alstrup, and S. Ullmann., Surf. Sci. 227 (1990) 291.
- [22] E. W. Plummer and W. Eberhart, Adv. Chem. Phys. 49 (1982) 533.
- [23] J. N. Andersen I. Chorkendorff, J. Onsgaard, J. Ghiejsen, R. L. Johnson, and F. Grey, Phys. Rev. B 37 (1988) 4809.
- [24] P. Heimann, J. Hermanson, J. Miosga, and H. Neddermeyer Phys. Rev. B 20 (1979) 3059.
- [25] S. D. Kevan, Phys. Rev. Lett. 50 (1983) 526.
- [26] C. N. Berglund and W. E. Spicer, Phys. Rev. 136 A (1964) 1030 *ibid.* 1044.

- [27] T. Gustafson and E. W. Plummer, in Photoemission and Electronic Properties of Surfaces; Ed B. Feuerbacher, B. Fitton, and R. F. Willis, Wiley, Chichester, p53 (1978).
- [28] G. Wentzel, Z. Phys. 43 (1927) 524.
- [29] L. E. Davis, N. C. Macdonald, P. W. Palmberg, G. E. Riach. and R. E. Weber, "Handbook of Auger Spectroscopy", Perkin-Elmer Corporation.
- [30] I. Chorkendorff, J. N. Russel Jr., and J. T. Yates Jr., J. Chem. Phys 86 (1987) 4692.
- [31] D. Briggs and M. P. Seah, "Practical Surface Analysis" Volume II, Wiley (1990) ISBN.
- [32] P. Sigmund, "Sputtering by Ion Bombardment; Theoretical Concepts" in Sputtering by Particle Bombardment I, Editor R. Behrisch. Springer-Verlag New York, (1982). Chapter 2.
- [33] P. Sigmund, Phys. Rev. 184 (1969) 383.
- [34] R. Behrisch. Sputtering by Particle Bombardment I and II, Springer-Verlag New York, (1982). Chapter 2.
- [35] A. Zalar, Thin Solid Films 124, (1985) 223.
- [36] S. Hoffmann, Chapter 4 in D. Briggs and M. P. Seah, "Practical Surface Analysis" Volumen I, Wiley (1990) ISBN 0 471 92081 9.
- [37] N. C. Alstrup, PhD Thesis, DTU (1993).
- [38] H. Ibach and D. L. Mills, "Electron Energy Loss Spectroscopy and Surface Vibrations" Academic Press, New York (1982).
- [39] T. Bruckmann, S. Lehrwald, G. Kisters, and H. Ibach, (1990).
- [40] P. A. Taylor, P. Rasmussen, C. V. Ovesen, P. Stoltze, and I. Chorkendorff, Surf. Sci. 261 (1992) 191.
- [41] A. M. Bradshaw, Surf. Sci. 11/12 (1982) 712.
- [42] M. R. Barnes and R. F. Willies, Phys. Rev. Lett. 41 (1978) 1729.

- [43] S. Bailey, G. Forment, J. W. Snoeck, and K. C. Waugh, *Catal. Lett.* 30 (1995) 99.
- [44] C. Kittel, *Elementary Solid State Physics: A Short Course*, Wiley, New York, 1962.
- [45] N. W. Ashcroft and N. D. Mermin, *Solid State Physics*, Holt-Saunders, Philadelphia, 1976.
- [46] C. J. Davidson and L. H. Germer, *Phys. Rev.* 30 (1927) 705.
- [47] J. B. Pendry, *Low Energy Electron Diffraction*, Academic Press, New York 1974.
- [48] M. A. van Hove and S. Y. Tong, *Surface Crystallography by LEED*, Springer, Berlin 1979.
- [49] K. Heinz and K. Muller, in *Structural Studies of Surfaces*, Springer Tracts in Modern Physics, vol 91. Springer Berlin 1982.
- [50] P. A. Taylor, P.B. Rasmussen, C. V. Ovesen, P. Stoltze, and I. Chorkendorff, *Surf. Sci.* 261 (1992) 191.
- [51] L. I. Schiff, "Quantum Mechanics" McGraw-Hill Tokyo (1968).
- [52] E. Merzbacher, "Quantum Mechanics" Wiley New York (1970).
- [53] G. Binnig, H. Rohrer, C. Gerber, and E. Weibel, *Appl. Phys. Lett.* 40 (1982) 178.
- [54] G. Binnig, H. Rohrer, C. Gerber, and E. Weibel, *Phys. Rev. Lett.* 49 (1982) 57.
- [55] G. Binnig, H. Rohrer, C. Gerber, and E. Weibel, *Phys. Rev. Lett.* 50 (1983) 120.
- [56] *Scanning Tunneling Microscopy I, II, III*, Springer Series in Surface Science Ed: R. Wiesendanger and H. J. Guntherodt, (1993) Berlin, ISBN 3-540-56317-2.
- [57] J. Tersoff and D. R. Hamann, *Phys. Rev. Lett.* 50 (1983) 1998.
- [58] J. Bardeen, *Phys. Rev. Lett.* 6, (1961) 57.

- [59] N. Lang, Chapter 2 in Scanning Tunneling Microscopy III, Springer Series in Surface Science, Ed: R. Wiesendanger and H. J. Guntherodt, (1993) Berlin, ISBN 3-540-56317-2.
- [60] M. L. Colaianni and I. Chorkendorff, Phys. Rev. B 50 (1994) 8798.
- [61] F. Besenbacher, Rep. Prog. Phys. 59 (1996) 1737.
- [62] F. Besenbacher, Chapter 10 in “Technical Physics of Solid Surfaces and Heterogeneous Catalysis”, Ed. D. King and D. P. Woodruff.
- [63] L. Pleth Nielsen, PhD Thesis from University of Århus, Denmark (1996).
- [64] F. Besenbacher, I. Chorkendorff, B. S. Clausen, B. Hammer, A. M. Molenbroek, and J. K. Nørskov, Science 279 (1998) 1913.
- [65] M. Ø. Pedersen, I. A. Bonicke, E. Lægsgaard, I. Stensgaard, A. Ruban, J. K. Nørskov, and F. Besenbacher, Surf. Sci. 387 (1997) 86.
- [66] A. K. Datye and N.J. Long, Ultramicroscopy 25 (1988) 203.
- [67] J. R. Rostrup-Nielsen, *Catalytic Steam Reforming* Catalysis- Science and Technology. Edited by J. R. Anderson and M. Boudart, Springer-Verlag, Berlin 1984, ISBN 3-540-12665-1.
- [68] S. M. Gates, J. N. Russel Jr., and J. T. Yates Jr., Surf. Sci. 159 (1985) 233.
- [69] H. R. Siddiqui, X. Guo, I. Chorkendorff, and J. T. Yates Jr., Surf. Sci. 191 (1987) L813.
- [70] P. B. Rasmussen and I. Chorkendorff, Surf. Sci. 248 (1991) 35.
- [71] J. N. Russel Jr., I. Chorkendorff, and J. T. Yates Jr., Surf. Sci. 183 (1987) 316.
- [72] ???
- [73] N. D. Lang and J. K. Nørskov, Physica Scripta 6 (19983) 15.